Numerical investigation into the effects of multiple bubbles in microchannel flow boiling

by

Louis Lombaard

Submitted in partial fulfilment of the requirements for the degree
Master of Mechanical Engineering

in the

Department of Mechanical and Aeronautical Engineering
Faculty of Engineering, Built Environment and Information Technology

UNIVERSITY OF PRETORIA
Supervisor: Dr Mohammad Moghimi Ardekani
Co-supervisors: Prof Josua Meyer and Dr Prashant Valluri

2021

Abstract

Numerical investigation into the effects of multiple bubbles in microchannel flow boiling

by

Louis Lombaard

Supervisor: *Dr Mohammad Moghimi Ardekani*

Co-supervisors: *Prof Josua Meyer and Dr Prashant Valluri*

Department: *Department of Mechanical and Aeronautical Engineering*

University: *University of Pretoria*

Degree: *Master of Mechanical Engineering*

Keywords: *Microchannel, flow boiling, multiple bubbles, computational fluid dynamics, Ansys Fluent*

Recent developments in microelectronics have produced higher heat fluxes that are beyond the capabilities of current heat exchangers. An increase in computing power coupled with decreasing processor size requires high thermal management on a smaller contact area. Microchannel heat sinks utilising flow boiling have been shown to produce heat fluxes orders of magnitude higher than those of their macroscale counterparts. Several factors influence the high heat transfer capabilities of the systems such as taking advantage of both the sensible and latent heat of the working fluid and the evaporation of the thin liquid film present between the channel walls and the vapour bubbles. Many researchers have investigated a wide range of microchannel geometries, orientations and different working fluids and applied heat fluxes. The correlations developed between confined boiling, heat flux and pressure drop are for macroscale flow and are ill-suited to microscale analysis. Heat transfer correlations are generally derived from experimental results conducted over a range of parameters and from evaluation of the influence of these varying parameters on the system. Because the scales of these phenomena are extremely small, visualisation and measurement during experimentation are difficult and inaccurate. Numerical modelling through computational fluid dynamics allows researchers to simulate and investigate these small-scale phenomena.

This study focused on numerically modelling the interaction between multiple bubbles during flow boiling of refrigerant R245fa. The two-dimensional numerical domain had a length of 36 mm, consisting of three sections, and a height of 0.5 mm. The first section was adiabatic to allow the patched bubbles to develop in shape before phase change was present. The middle section had an applied heat flux of 5 kW/m^2 and was the main focus. The last section was also adiabatic and was used to retain the leading bubbles. An interface-tracking mesh refinement method was used in all the cases. This method refined the liquid-vapour interface and a set distance around the interface, reducing the computational cost of the simulations.

The results from Magnini, Pulvirenti & Thome (2013a) were recreated with less than 4% of the required mesh elements. A set of three-dimensional simulations was attempted using the same method, but the simulations have not yet been completed. The bubbles were patched into the

domain, instead of simulating bubble departure, to have better control over the positions of the bubbles.

In all the cases, the heat flux improved from the first to the second bubble by at least 25%. A further 20% improvement was observed from the second to the third bubble at the end of the heated section. An increase in phase change was observed as the distance between bubbles were decreased, suggesting better heat transfer. This study illustrated the advantages of flow boiling over single-phase cooling, and the results corresponded to the findings of Magnini et al. (2013a) and Magnini & Thome (2016).

Acknowledgements

I want to thank and acknowledge the following people:

- my supervisor, Dr Mohammad Moghimi Ardekani, for his guidance and support, both technically and morally;
- my co-supervisors, Prof Josua Meyer, for providing me with a bursary for my postgraduate studies and assisting me in returning to South Africa during the Covid-19 pandemic, and Dr Prashant Valluri, for his support, guidance and warm welcome to the University of Edinburgh;
- my family and friends, for their love, support and motivation during my studies.

Above all, my thanks go to God, for His amazing grace, the opportunity that I have received and for keeping me safe abroad and during this challenging time.

Contents

List of figures

List of tables

Nomenclature

Symbols

A	Area [m^2]
c_p	Specific heat capacity [J/kg.K]
D	Diameter [m]
e	Error
F	Force
G	Mass flux [$kg/m^2.s$]
g	Gravitational acceleration [m/s^2]
h	Heat transfer coefficient [$W/m^2.K$]
Δh_e	Inlet subcooling enthalpy
h_L	Latent heat capacity [J/kg]
k	Conductivity [W/m.K]
L	Length [m]
L_{Bi}	Initial bubble length [m]
L_{int}	Initial spacing [m]
M	Molecular mass
m	Mass [kg]
$\dot{m}$	Mass transfer rate [$kg/m^3.s$]
P	Pressure [Pa]
p	Perimeter [m]
$\dot{q}$	Heat flux [W/m^2]
$\dot{q}_c$	Critical heat flux [W/m^2]
R_g	Gas constant [J/kg.mol]
S_E	Energy generation source term
S_g	Vapour mass source term [$kg/m^3.s$]
S_L	Liquid mass source term [$kg/m^3.s$]
T	Temperature [K]
t	Time [s]
U	Velocity [m/s]
V	Volume [m^3]
V_{int}	Initial volume [m^3]
x_c	Critical quality
x_i	Initial position from heated entrance [m]
x_H	Non-dimensional position in the heated region

Greek letters

α	Volume fraction
γ	Mass transfer coefficient
δ_t	Film thickness [m]
Δ	Change in property
κ	Interface curvature
μ	Dynamic viscosity [kg/m.s]
π	Pi
ρ	Density [kg/m^3]
σ	Surface tension [N/m]
$\emptyset$	Scalar property
τ	Non-dimensional time
ψ	Level-set function

ω	Mass transfer coefficient
Subscripts	
a	Acceleration
c	Entrance contraction
$crit$	Critical
e	Expansion
eq	Equivalent
f	Fluid
$f, 1-ph$	Single-phase frictional pressure drop
f, tp	Two-phase frictional pressure drop
g	Gravitational
H	Heated
h	Hydraulic
i	Interfacial
L	Liquid
nw	Near-wall
P	Primary phase
S	Secondary phase
sat	Saturated
tp	Two-phase
tr	Threshold
$unsat$	Unsaturated
v	Vapour
w	Wall
Superscripts	
$\rightarrow$	Vector
$-$	Single-fluid approach
Abbreviations	
CFD	Computational fluid dynamics
CFL	Courant-Friedrichs Lewy number
CHF	Critical heat flux
CSF	Continuum surface force
GCI	Grid convergence index
HTC	Heat transfer coefficient
LS	Level-set
MCHS	Microchannel heat sink
PISO	Pressure-Implicit with Splitting of Operators
PRESTO!	PREssure Staggered Option
UDF	User-defined function
VOF	Volume of fluid
Dimensionless numbers	
Bo	Bond number
Ca	Capillary number
Co	Confinement number
Eö	Eötvös
Nu	Nusselt number
Pr	Prandtl number
Re	Reynolds number
We	Webber number

1. Introduction

1.1 Background

The Industrial Revolution was the start of drastic and rapid progress in various fields, unknown in human history. This progress has led to bigger buildings, faster cars and smaller, more powerful electronics, driven by the many ways of producing and consuming large amounts of energy.

Effective control of the heat energy produced by electronic components is crucial to their optimal performance and longer lifespans. While processors are shrinking, they are also becoming more powerful, resulting in a larger thermal output over a smaller area to which a heat sink can be attached. Standard air-cooling systems cannot handle these high heat fluxes nor prevent the processors from overheating. Although liquid cooling systems are common in industrial and commercial computers, the heat fluxes are still beyond the capabilities of these systems.

A recent method for improving the capabilities of liquid cooling systems is to reduce the size of the channels in compact heat exchangers. Reducing the diameter increases the heat transfer coefficient (HTC), as shown in Figure 1-1. These small channels are called mini- and microchannels. When moving down to the microscale, the governing properties of the flow change. The intermolecular forces such as surface tension have a larger influence than gravity and viscosity on the microscale flow. Microchannel heat sinks (MCHSs) provide larger heat fluxes than standard heat exchangers but require more pumping power due to a larger pressure drop (Figure 1-2).

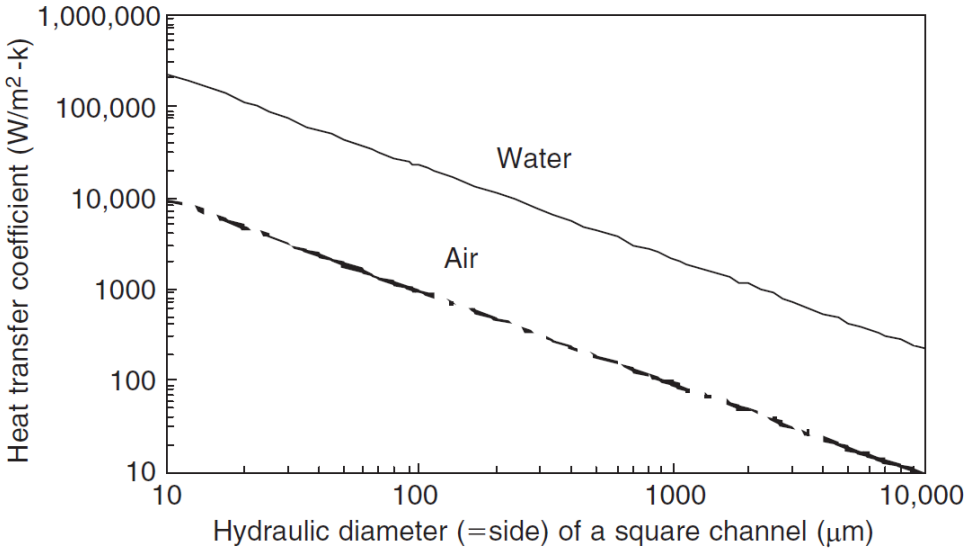

Figure 1-1: Variation of heat transfer coefficient with channel size for fully developed laminar flow of air and water (Kandlikar, Garimella, Li, Colin & King, 2005).

Single-phase microchannel heat sinks can provide sufficient thermal management for most applications. However, some industries can produce heat fluxes beyond the limits of single-phase systems; for example, microelectronics and concentrated solar power. Single-phase liquid systems only utilise the sensible heat of the refrigerant. As the temperature of the fluid rises, the efficiency of the system reduces. Employing the latent heat with the sensible heat of the fluid increases the amount of heat that can be absorbed. The refrigerant is heated to saturation temperature for this process and remains there while phase change occurs as more energy is absorbed. This process is called flow boiling and produces significantly larger heat fluxes than for single-phase flow.

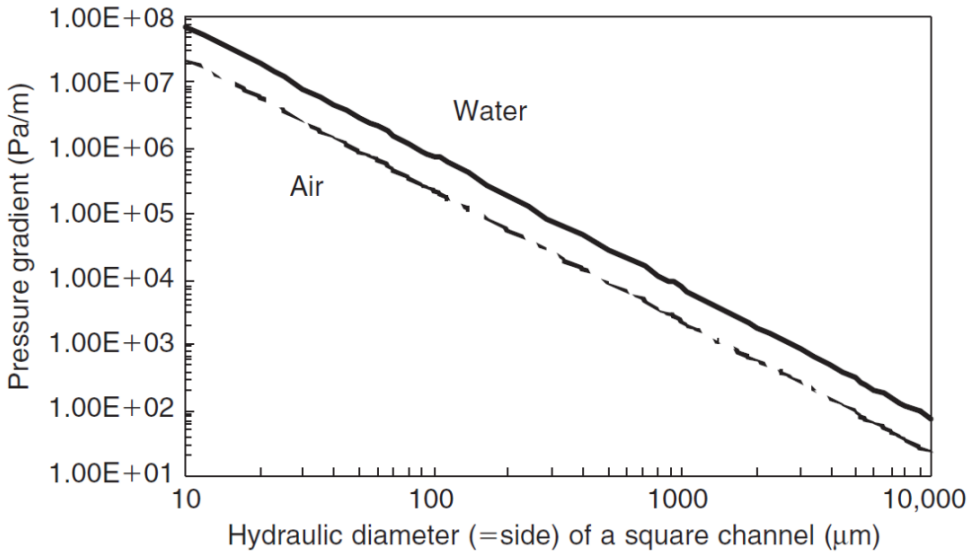

Figure 1-2: Variation of pressure gradient with channel size for fully developed laminar flow of air and water (Kandlikar et al., 2005).

1.2 Motivation

Much research and experimentation have been conducted to understand how the heat transfer and pressure drop in microchannels are influenced by factors such as geometry and aspect ratio. The smaller the scale of the channel under investigation, the harder it becomes to analyse the physical phenomena present. Current experimental equipment is expensive and cannot accurately predict the exact state of the inside of microchannels due to the minute scales involved. These drawbacks have led to researchers using numerical investigations through computational fluid dynamics (CFD) software.

CFD software allows researchers to visualise and measure various microscale properties that are not possible through experimentation due to factors including light diffraction and the transparency of the working fluid. Numerical modelling also offers researchers better control over the system, allowing them to investigate a single parameter while the rest of the conditions remain constant. Once a numerical model is validated against previous results, multiple effects can be investigated without manufacturing a new physical model. These results can be used together with experimental results to improve heat transfer correlations in order to design more efficient compact heat exchangers.

1.3 Problem statement

Employing a microchannel heat sink is a promising solution to thermal management in many industries, such as the microelectronic industry. The various thermophysical and geometrical requirements present in the industry have driven researchers to better understand the physics involved in optimising the systems. The small scales make quantifying relations through experimental investigations difficult.

Because of the complexity of the flow-boiling process and the many influences, several of the phenomena involved are not well understood; for example, bubble departure and coalescence. Studies investigating these phenomena are scarce, and three-dimensional simulations are difficult due to the high computational costs of conventional methods.

The interaction between multiple bubbles and the effect of gravity in microchannels are not entirely understood and limited to only a few studies. In this study, multiple bubbles were simulated to investigate the effects on heat transfer and the influence of gravity.

1.4 Objectives

A good understanding of the governing phenomena and the many thermophysical models in Ansys Fluent 19.4 is required to create an accurate numerical model of slug flow boiling in a microchannel. The microchannel in question had a rectangular cross-section and a high aspect ratio with multiple bubbles present.

The objectives of this study were as follows:

- to validate the adaptive meshing and mass transfer models against previously published research;
- to conduct various two-dimensional simulations in order to investigate the effects of multiple bubbles in a microchannel separated by a liquid slug of varying lengths;
- to recreate a case in a three-dimensional domain in order to investigate the effects of gravitational orientation.

To summarise, the study aimed to evaluate how the interaction between bubbles was influenced by the distance between them and the gravitational orientation, giving insight into how different heat transfer characteristics were produced.

1.5 Layout

The layout of this study is as follows:

- a literature review conducted to gain insight into previous research on microchannel flow boiling and the models used;
- a discussion of the selected models and methods and validation against previous research;
- multiple two-dimensional simulations with two or three bubbles and a review of the three-dimensional case;
- a review of the results and a conclusion with recommendations for further research.

2. Literature study

2.1 Introduction

The development of smaller high-performance electronics has created a need for smaller heat exchangers. This need has led to the investigation of microchannel heat sinks (MCHSs). Microfluidics is present in devices with sizes in millimetres to micrometres and volumes ranging from nano- to millilitres (Ottino & Wiggins, 2004). Two-phase flow in particular has gained interest due to the possibility of higher heat transfer and overcoming numerous challenges associated with single-phase flow. Due to the small geometric and time scales of microchannels, advanced experimental equipment is required to obtain data accurately. For this reason, numerical analysis with computational fluid dynamics (CFD) has been the preferred choice. Numerical simulations have their challenges with regard to mathematical models and the computational power available.

This chapter reviews flow boiling in microchannels. The following aspects are considered: defining a microchannel, how flow boiling increases heat transfer and the various flow fields produced, what numerical methods are available and how they have been implemented, as well as applications for microchannel heat sinks.

2.2 Microchannels

Defining a microchannel is difficult due to the many combinations of shapes and sizes used in various applications. Categorising a channel based on size alone is insufficient because it does not account for the fluid properties that also influence the flow; for example, viscosity or surface tension. The countless combinations of shapes, sizes and fluid properties have led to various definitions and classifications.

Kandlikar (2002) categorised the channels by hydraulic diameter alone into three groups. The categories are conventional or macrochannels for a diameter of 3 mm or larger, minichannels for diameters between 200 µm and 3 mm and microchannels for diameters between 10 and 200 µm. Li & Wang (2003) conducted an experimental two-phase flow study to investigate the effects of channel size. They used surface tension and phase densities to define a critical (D_{crit}) and a threshold diameter (D_{tr}). The diameters were calculated with the following equations:

$$D_{crit} = 0.224 \sqrt{\frac{\sigma}{g(\rho_L - \rho_v)}} \tag{2.1}$$

$$D_{tr} = 1.75 \sqrt{\frac{\sigma}{g(\rho_L - \rho_v)}} \tag{2.2}$$

where σ is the surface tension [N/m], g is the acceleration due to the gravity [m/s^2], ρ_L is the liquid density [kg/m^3] and ρ_v is the vapour density [kg/m^3].

They reported that when $D < D_{crit,}$ the surface tension forces dominated the flow behaviour, while gravity was the dominant force for $D > D_{tr}$ and both forces had a relatively equal effect when $D_{crit} < D < D_{tr}$. Sample data for the critical and threshold diameters are reported in Table 2-1 for water, glycol, R22 and R134a in the temperature range of 283 to 450 K.

Table 2-1: Predicted critical and threshold diameters for water, glycol, R22 and R134a (adapted from Li & Wang (2003)).

Liquid	Temperature [K]	Surface tension [N/m]	D_{crit} [µm]	D_{tr} [µm]
Water	300	0.0717	600	4680
	450	0.0429	490	3827
Glycol	300	0.0478	464	3624
	373	0.0413	442	3452
R22	283	0.0104	206	1609
	333	0.0034	136	1062
R134a	283	0.0103	207	1617
	333	0.0038	140	1093

Ong & Thome (2011) proposed new criteria based on their experimental results. They found that the transition threshold from macro- to microscale depended on the channel confinement, mass velocity, phase densities, surface tension, saturation temperature, viscosity and flow pattern. Their threshold was based on the dimensionless confinement number (Co). The Co is a relation between the hydrodynamic properties of the fluid and the channel diameter:

$$Co = \frac{1}{D}\sqrt{\frac{\sigma}{g(\rho_L - \rho_v)}} \tag{2.3}$$

They concluded that macroscale behaviour was observed for $Co < 0.34$ and microscale behaviour for $Co > 1$. When the Co was between these points, the flow pattern was used to judge the scale.

The confinement number is one of many dimensionless numbers used in dimensionless analysis. Dimensionless analysis reduces the number of parameters in a system and helps researchers to develop correlations. These terms allow researchers to change variables such as velocity and density without additional experiments or numerical simulations.

The dimensionless terms applicable to heat transfer in the microscale are the confinement number (Co), Reynolds number (Re), Nusselt number (Nu), Prandtl number (Pr), capillary number (Ca), Weber number (We), Bond number (Bo) and the Eötvös number ($E\ddot{o}$).

The Reynolds number, Re, is the most widely used and is the ratio of the inertial to viscous forces acting on the fluid:

$$Re = \frac{\rho U D_h}{\mu} \tag{2.4}$$

where ρ is the fluid density [kg/m^3], U is the velocity [m/s], D_h is the hydraulic diameter [m] and μ is the dynamic viscosity of the fluid [Pa s]. The Reynolds number is generally used to judge whether laminar or turbulent conditions are present. For flow inside tubes or channels, the transition from laminar to turbulent occurs at 2 300 (Çengel & Ghajar, 2015). Talimi, Muzychka & Kocabiyik (2012) reported that for two-phase flow, the transition from laminar to turbulent flow occurs at a Reynolds number of about 1 000.

The next number is the Nusselt number, Nu, representing the ratio of convective and conduction heat transfer at the boundary between the solid and the fluid. The Nu is important to evaluate the heat transfer characteristics of a system. The Nu is calculated as follows:

$$Nu = \frac{hD}{k} \tag{2.5}$$

where h is the convective heat transfer coefficient [W/m^2], and k is the conductivity of the fluid [W/m].

Sadeghi, Bahrami & Djilali (2010) investigated the Nu relations of microchannels with various cross-sectional geometries. They used the square root of the cross-sectional area as the characteristic length, rather than the more commonly used hydraulic diameter. Their Nu is related to equation 2.5 by:

$$Nu_{\sqrt{A}} = \frac{p}{4\sqrt{A}} Nu \tag{2.6}$$

where p is the perimeter [m] and A is the cross-sectional area [m^2].

The Prandtl number, Pr, is the ratio of the momentum diffusion to thermal diffusion. It is calculated with:

$$\mathrm{Pr} = \frac{\mu c_p}{k} \tag{2.7}$$

where c_p is the specific heat capacity [J/kg.K]. The Pr can be used in combination with the Re for Nu correlations of various cases and geometries. According to Çengel & Ghajar (2015), the average Nu of flow over a flat plate or cylinder can be calculated with:

$$Nu = C\ Re^m Pr^n \tag{2.8}$$

where C, m and n are geometry-specific constants.

The capillary number, Ca, indicates the relative effect of viscous forces on interfacial tension forces:

$$Ca = \frac{\mu U}{\sigma} \tag{2.9}$$

As the interfacial forces overcome the viscous forces, a liquid layer forms. The Ca can be used to calculate the thickness of the liquid. For very low Ca ($Ca < 10^{-3}$), the film thickness can be correlated to only Ca (Bretherton, 1961; Carlson, 2007).

The Weber number, We, is the ratio between inertial and surface forces:

$$We = Re * Ca = \frac{\rho U^2 D_h}{\sigma} \tag{2.10}$$

The importance of surface tension effects in the microscale is evaluated based on Re, Ca and We. For low Re, the Ca is of interest and We at high Re (Talimi et al., 2012).

The Bond number, Bo, represents the importance of the interfacial forces concerning gravity (Bordbar, Taassob, Zarnaghsh & Kamali, 2018):

$$Bo = \frac{(\rho_L - \rho_v) g D_h^2}{\sigma} \tag{2.11}$$

The Bo is valuable for studies where gravity or gravitational orientation is present. The Bo is the reciprocal of the squared Co:

$$Bo = \frac{1}{Co^2} \tag{2.12}$$

Therefore, the Bo can be used to define the microscale, similar to the criteria of Ong & Thome (2011).

The last number is the Eötvös number, $E\ddot{o}$, which is the ratio of surface tension effects and gravity. The $E\ddot{o}$ is calculated with:

$$E\ddot{o} = \frac{(2\pi)^2 \sigma}{(\rho_L - \rho_v) D_h^2 g} \tag{2.13}$$

The surface tension becomes dominant in the flow once $E\ddot{o} > 1$.

These dimensionless numbers are useful to develop correlations and allow more freedom when scaling models.

2.3 Boiling

With the advance in computing technology in order to create smaller, faster and more powerful parts arises the need for more effective cooling methods (Sakanova, Keian & Zhao, 2015). Microchannel heat sinks (MCHSs) have been investigated since the 1980s (Tuckerman & Pease, 1981) and have proved to be an effective method for heat removal (Asthana, Zinovik, Weinmueller & Poulikakos, 2011). Single-phase flow through microchannel heat sinks requires high pressure, and when fully developed, the flow is laminar, resulting in only conduction heat transfer in the transverse direction (Che, Wong & Nguyen, 2012). Two general methods are used to make the flow more turbulent; the first involves geometry. Geometries consisting of wavy or corrugated channels generate vortices, which improves mixing and results in higher heat transfer (Naphon, 2007; Sui, Teo, Lee, Chew & Shu, 2010)

The second method is focused on alternating the fluid properties or flow conditions. Alternating properties are achieved by using additives, including gas bubbles, immiscible droplets or solid particles. The addition of solid particles refers to nanofluids. Gas bubbles can be present in boiling and non-boiling conditions. Studies have shown that flow boiling can significantly increase heat transfer when compared with single-phase flow. Figure 2-1 illustrates the experimental results of a study comparing single-phase and slug flow in a square microchannel (Betz & Attinger, 2010).

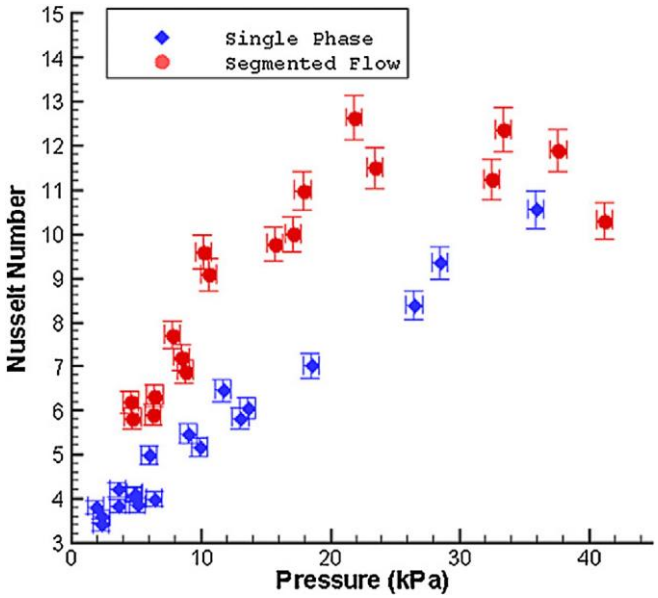

Figure 2-1: Nusselt number versus pressure drop of single-phase and slug flow in a square microchannel (Betz & Attinger, 2010).

Flow boiling produces higher heat transfer by disturbing the flow and utilising the latent heat of evaporation. This allows the working fluid to absorb more heat. Kandlikar et al. (2005) reported that two-phase flow in a square microchannel could produce an HTC 10 times greater than in single-phase flow.

Boiling heat transfer can be classified as pool boiling and flow boiling. During pool boiling, there is no bulk fluid motion, while flow boiling occurs in a fluid passing a heated surface resulting in combined convection and pool boiling. Therefore, a good understanding of pool boiling is important to understand flow boiling (Çengel & Ghajar, 2015).

Boiling occurs when a liquid in contact with a heated surface absorbs enough energy to undergo phase change from liquid to vapour. When enough vapour has formed, the buoyancy force overcomes the surface tension, and the bubble detaches from the surface. Once the bubble has departed, cooler liquid flows into the space created in its absence.

Boiling consists of three regimes: nucleate, transition and film boiling. Figure 2-2 shows the pool-boiling curve for water at 1 atm and indicates the three regimes' temperature and heat flux relations. Nucleate boiling is the first regime and is divided into two different flow patterns: isolated bubbles and continuous columns. The isolated bubbles form along the surface and detach individually; as they rise, heat is transferred to the cooler liquid, and the bubbles collapse. As the surface temperature rises and the bubble frequency is high enough, continuous columns of bubbles form, which agitate the fluid. This agitation improves convection and increases the heat transfer (Çengel & Ghajar, 2015).

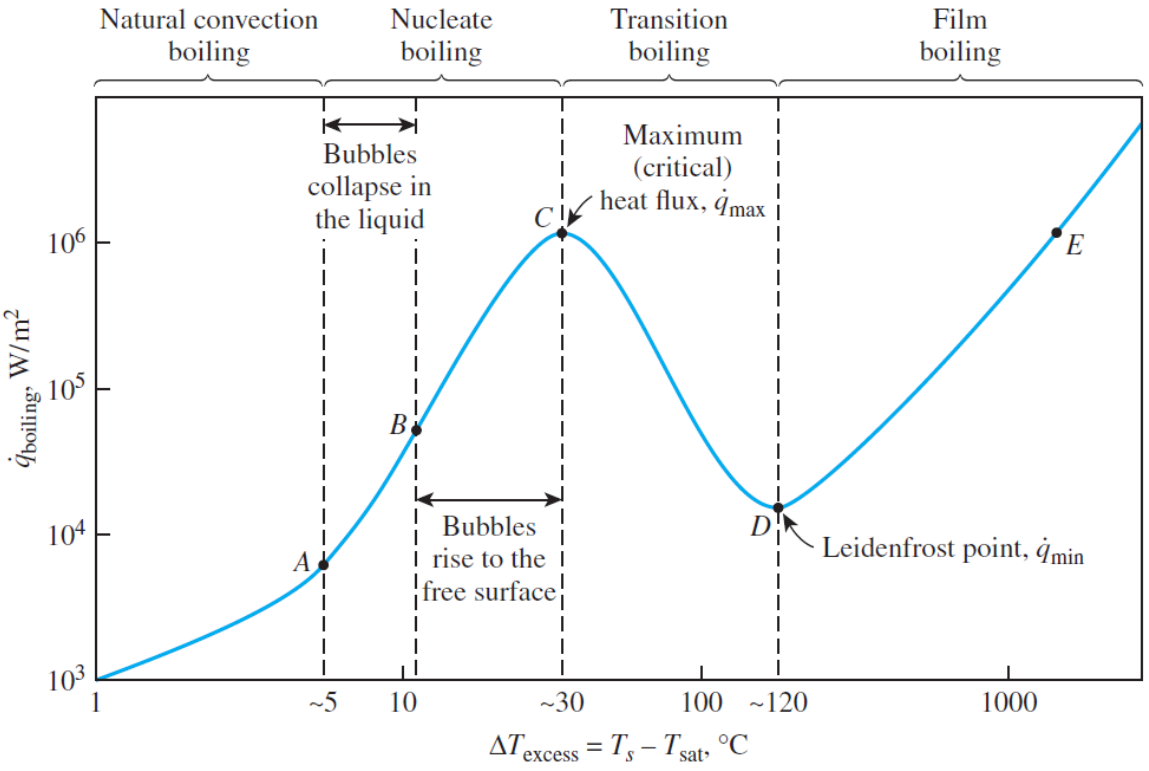

Figure 2-2: Pool-boiling curve for water at 1 atm (Çengel & Ghajar, 2015).

The best regime for boiling heat transfer is the nucleate boiling regime, because it provides a higher heat flux than transition boiling does and avoids the high temperatures required for film boiling. During transition boiling, large vapour bubbles cover the heated surface, reducing the amount of liquid

in contact with the surface. The vapour film has reduced heat transfer capabilities, preventing the heat from being transferred from the surface to the fluid. This reduction in heat transfer leads the surface temperature to rise and the film to increase in size.

Once the vapour film covers the entire surface, film boiling has been achieved. Film boiling changes the heat transfer from convection to conduction through the vapour. Film boiling requires a higher surface temperature than nucleate boiling does to achieve the same heat flux, but this temperature is generally higher than the melting temperature of the surface and can lead to burnout.

Now flow boiling can be discussed. Flow boiling has two categories, namely internal and external flow. Flow boiling also produces a significantly higher HTC than that of pool boiling because of the additional convection. For external flow, the fluid is open to the atmosphere allowing the vapour to escape and simplifying external flow when compared with internal flow (Çengel & Ghajar, 2015).

Internal flow boiling is generally referred to as two-phase flow and was employed in this study. Two-phase flow has been shown to significantly improve the HTC (Chinnov, Ronshin & Kabov, 2015). The convection present in two-phase flow changes the relation between temperature difference and heat transfer from that of pool boiling. This relation is illustrated in Figure 2-3.

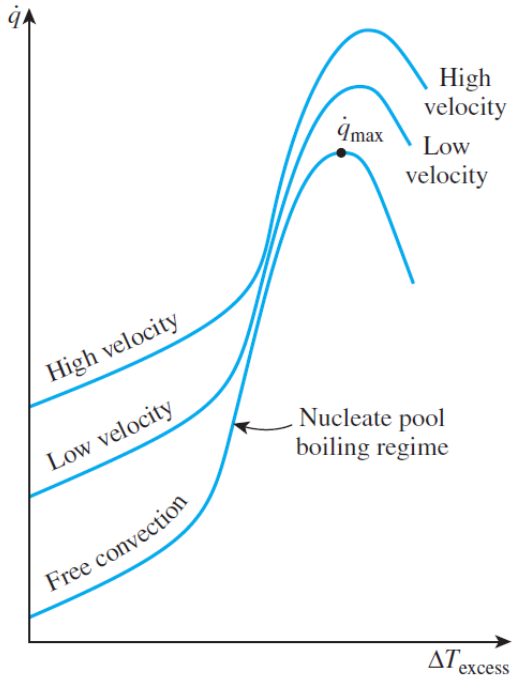

Figure 2-3: Flow-boiling curve (Çengel & Ghajar, 2015).

The flow-boiling curve clearly shows the dependence of heat transfer on fluid velocity; this also illustrates the importance of the Reynolds number (Re). For single-phase flow, the HTC can be calculated from the known heat flux at the surface and the temperatures of the wall and local fluid with the following equation (Wang, Sefiane & Harmand, 2012):

$$h = \frac{\dot{q}}{T_W - T_L} \tag{2.14}$$

where the HTC is represented by h [W/m^2.K], the heat flux by $\dot{q}$ [W/m^2] and T_W and T_L the wall and local fluid temperature [K] respectively.

To obtain the local fluid temperature, it is assumed that there is a no-slip condition at the walls and a small layer of thickness δ_t where the temperature has a linear distribution. The heat transfer due to conduction and convection is then equated to attain the following equation (Kandlikar et al., 2005):

$$\delta_t = \frac{k}{h} \tag{2.15}$$

where δ_t is the liquid layer thickness [m], k is the thermal conductivity of the liquid [W/m], and h is the single-phase HTC, calculated before boiling occurs [W/m^2].

Substituting the new HTC into equation 2.5 gives the following equation for the local single-phase Nu:

$$Nu = \frac{\dot{q} D_h}{k(T_W - T_L)} \tag{2.16}$$

This equation allows for easier calculation of the Nu because when a known heat flux and wall temperature are applied, the HTC can be calculated. This HTC can then be used when the heat flux is unknown. To calculate the HTC for two-phase flow, the saturation temperature is used instead of the local fluid temperature (Ferrari, Magnini & Thome, 2018):

$$h_{tp} = \frac{\dot{q}}{T_W - T_{sat}} \tag{2.17}$$

where h_{tp} is the two-phase HTC.

Calculating the Nu of two-phase flow is more complicated since heat is conducted through the liquid film into the vapour bubbles. The calculation requires the heat and mass transfer rates between the phases to be balanced. In previous studies conducted by Gupta, Fletcher & Haynes (2010) and Agostini, Bontemps & Thonon (2006), the HTC was calculated using the bulk fluid temperature rather than the local fluid temperature. This is a valid approach as the bulk temperature should be close to the saturation temperature of the fluid during phase change.

The Nu equation is transformed to:

$$Nu = \frac{\dot{q} D_h}{k(T_W - T_{sat})} \tag{2.18}$$

An important aspect of microchannel heat exchangers and a reason for their use in cooling applications are the maximum heat flux that can be acquired. This heat flux is commonly referred to as the critical heat flux (CHF) and is dependent on both the fluid and channel properties. The various combinations of these properties make it difficult to produce an accurate model of the CHF. Wojtan, Revellin, Thome & Italia (2006) produced the following correlations for the CHF and the vapour quality at CHF:

$$\dot{q}_c = 0.437 \left(\frac{\rho_v}{\rho_L}\right)^{0.073} We^{-0.24} \left(\frac{L_H}{D_h}\right)^{-0.72} Gh_L \tag{2.19}$$

$$x_c = \frac{4\dot{q}_c L_h}{G(h_L + \Delta h_e) D_h} \tag{2.20}$$

where $\dot{q}_c$ is CHF [W], L_h is the heated length [m], G is the mass flow rate [kg/s], x_c is the critical quality and $\Delta h_e$is the inlet subcooling enthalpy. This correlation only applies to circular microchannels with uniform heat flux and predicts the CHF with an error of 7.6%.

The inherent nature of flow boiling to produce vapour bubbles with a lower density disturbs the laminar flow profile. This disturbance creates a variety of different flow patterns, each uniquely influencing the heat transfer.

2.4 Flow regimes

Due to a lack of a free surface, the vapour present in internal flow boiling is forced to flow with the liquid through the channel. The vapour has its own distinct thermophysical properties and the interaction between vapour and liquid phases results in various flow patterns. Two-phase flow occurs either when there are gas bubbles or immiscible droplets present in the primary fluid. Zhao, Chen & Yuan (2006) conducted a study of liquid-liquid two-phase flow, while the current study only focused on liquid-vapour two-phase flow.

Many studies have been conducted on the different flow patterns that occur as the quality of the working fluid changes. Examples of experimental studies are those of Kreutzer, Kapteijn, Moulijn & Heiszwolf (2005) and Barber, Sefiane, Brutin & Tadrist (2009). Many numerical studies have focused on simulating the behaviour of the different regimes (Guo, Fletcher & Haynes, 2016; Bordbar et al., 2018).

The characteristics of each regime are unique, leading to various flow rates, heat transfer and pressure drops (Bogojevic, Sefiane, Walton, Lin & Cummins, 2009). The four main flow patterns are illustrated in Figure 2-4: (a) bubbly flow, (b) slug, Taylor or capillary flow, (c) churn flow, (d) and (e) annular flow. There are also transitional regions with combined properties between the mentioned regimes.

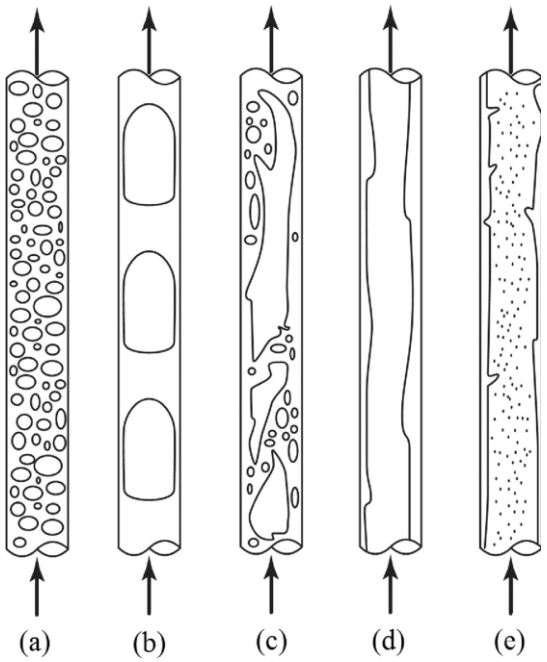

Figure 2-4: Flow patterns in capillary channels (Bordbar et al., 2018).

As subcooled liquid enters a heated microchannel, bubbles start to form on the heated surfaces and detach once large enough. This creates bubbly flow, which is characterised by distinct non-spherical bubbles with diameters smaller than the hydraulic diameter of the channel, occurring at moderate velocities (Mikaelian, Haut & Scheid, 2015). As the bubbles grow, they become confined in the radial direction and can only expand in the axial direction. This is the slug flow regime and is recognised by the alternating segments of the two phases. The vapour phase occupies most of the

channel's cross-section. This type of flow is present when the velocity is higher than that of bubbly flow but does not overcome the surface tension force of the liquid phase (Serizawa, Feng & Kawara, 2002).

The bubble size in slug flow can lead to two scenarios; either the vapour phase contacts the wall or a liquid film between the wall and the bubble forms (Srinivasan & Khandekar, 2017). The film thickness is increased by the viscous force and decreased by the surface tension force (Han & Shikazono, 2009). The behaviour of the film depends on the channel geometry. A relatively uniform film is present in circular channels, while fluid build-up occurs in the corners of rectangular channels.

The two-phase interface results in recirculation within the primary and secondary phases of slug flow (Figure 2-5). As the fluid near the axis moves forward, it is blocked by the front interface and is displaced radially. The fluid then moves backwards along the wall until it reaches the rear interface, where it is redirected to converge towards the axis. This recirculation enhances heat transfer between the wall and the liquid (Che, Wong & Nguyen, 2013). The most significant influence on the internal flow topology of liquid slugs is the viscosity ratio (Ma, Sherwood, Huck & Balabani, 2014). The viscosity ratio (λ) is the ratio of the vapour phase's viscosity to the liquid phase's viscosity.

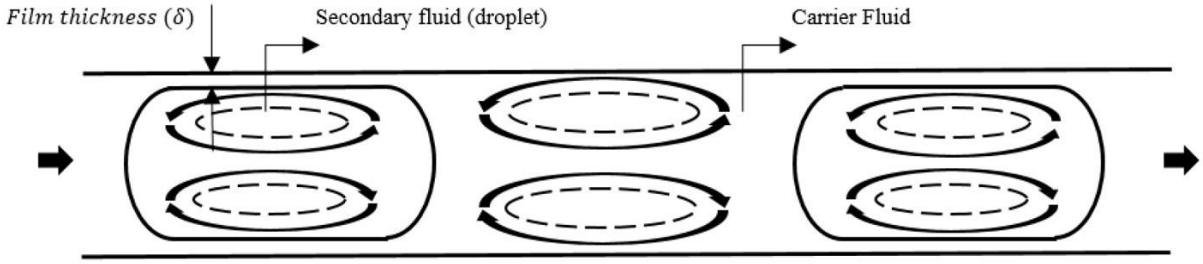

Figure 2-5: Recirculation in two-phase slug flow (Abdollahi, Sharma & Vatani, 2017).

As the bubbles grow further, churn flow develops. Churn flow is characterised by instabilities in the flow. These instabilities cause the bubbles to break apart and reform. Churn flow is similar to annular flow with additional liquid slugs between the vapour bubbles (Kew & Cornwell, 1997).

The annular flow regime has been reached when the vapour quality is high enough and the bubbles have merged, the vapour then starts to flow down the centre of the channel in a continuous stream. The liquid is only present around the perimeter of the channel. This liquid film can dry out and cause burnout (Guo et al., 2016).

The liquid film present in slug and annular flow plays a crucial role in the heat transfer capabilities of the microchannel. Each flow regime has its own CHF, which can vary along the length of the channel. Szczukiewicz, Borhani & Thome (2013) conducted an experimental investigation into the relation between heat flux and fluid quality. The results, shown in Figure 2-6, have a similar trend to those of the pool-boiling curve in Figure 2-2. This indicates a relation between pool boiling and flow boiling in microchannels. Kew & Cornwell (1997) found that nucleate pool-boiling correlations were more accurate at predicting the heat transfer than flow-boiling correlations for channels with a Co greater than 0.5.

The complexity of two-phase flow results in large fluctuations of the heat transfer over the heated surfaces, which can benefit the heat exchanger, although this unstable nature of flow boiling leads to a pressure drop, which requires increased pumping power.

The viscosity of the fluid causes a no-slip boundary condition at the walls and results in a pressure drop when pumping the fluid through a small channel. The velocity of the fluid at the wall is zero due

to the no-slip condition, causing the velocity at the centre of the channel to increase due to the conservation of mass. The increased velocity creates a varying velocity field due to shear stresses in the fluid. Ribatski, Wojtan & Thome (2006) analysed previous studies and reported that increasing the mass flux increased the pressure drop. In contrast, an increase in saturation temperature or channel diameter decreased the pressure drop.

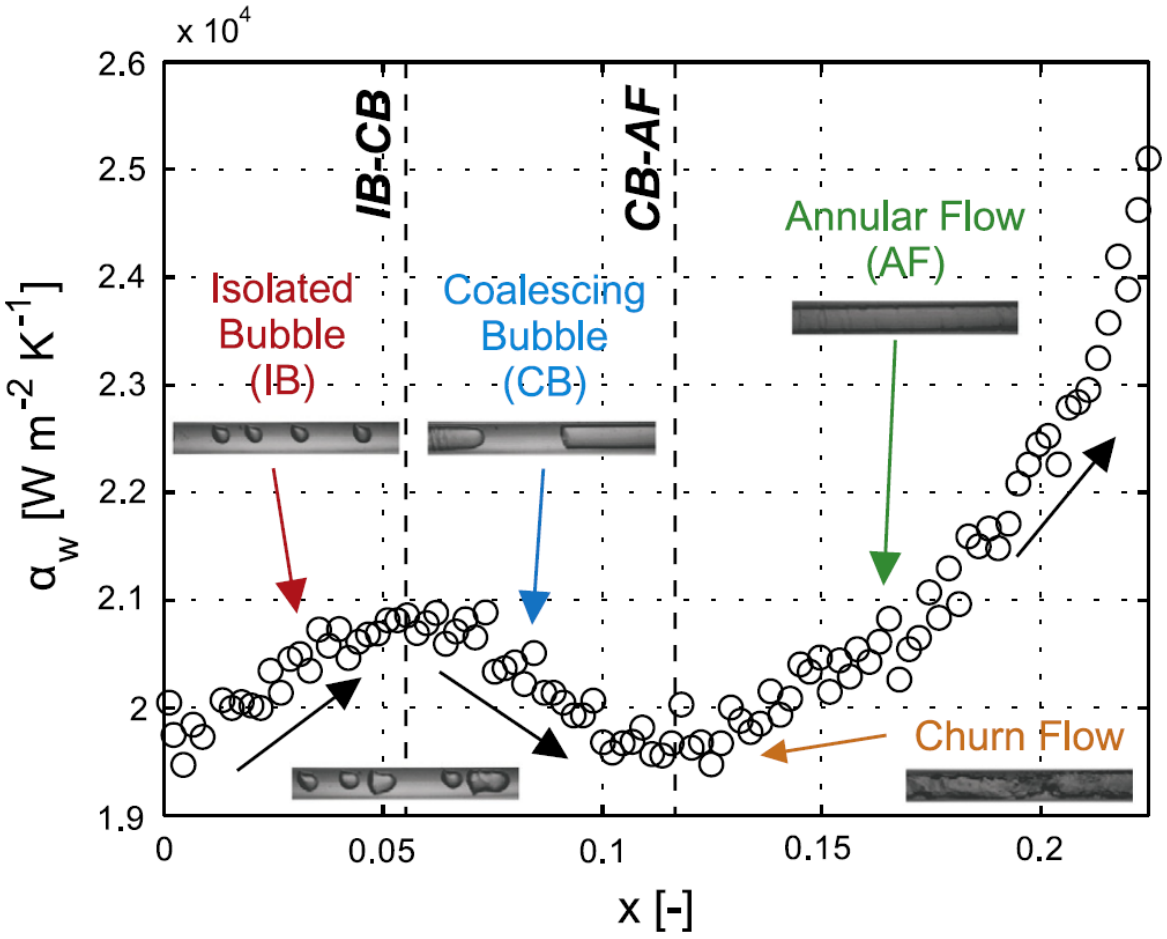

Figure 2-6: Heat flux versus fluid quality for flow boiling of R236fa (Szczukiewicz et al., 2013) with flow visualisation by Revellin (2005).

The presence of an additional phase with a considerably different density and velocity complicates the calculation of pressure drop in two-phase flow. Two different pressure drop prediction models were reported in the literature. The first model was proposed by Lockhart & Martinelli (1949) and considered each phase separately. It was assumed that the stream of a given phase travelled at its mean velocity. The second model assumed that the multiphase fluid behaved as a pseudo-single phase. The pseudo-properties were based on the fractions of the phases and their respective properties (Ribatski et al., 2006).

Kandlikar et al. (2005) suggested that the pressure drop in microchannels was due to the following six factors: contraction at the entrance (c), single-phase friction pressure drop ($f, 1-ph$), two-phase friction pressure drop (f, tp), acceleration due to evaporation (a), gravity (g) and expansion at the outlet (e). These components are summed to obtain the total pressure change:

$$\Delta P = \Delta P_c + \Delta P_{f,1-ph} + \Delta P_{f,tp} + \Delta P_a + \Delta P_g + \Delta P_e \qquad (2.21)$$

The sudden changes in the volume of the vapour bubbles and their movement can lead to large fluctuations in pressure, temperature and HTC, and even mechanical vibrations. Szczukiewicz, Magnini & Thome (2014) reported vapour backflow and flow maldistribution due to the fluctuations. They also found that applying a flow restriction at the inlet could stabilise the flow.

These fluctuations increase significantly in parallel microchannels. Bogojevic et al. (2009) observed that the fluctuations could lead to an asymmetrical flow distribution across parallel microchannels. They also reported that the instabilities were related to the heat flux to mass flux ratio and the inlet condition. Mohammed, Gunnasegaran & Shuaib (2011) used wavy microchannels to induce instability to the flow and reported an increased HTC. However, as the HTC was increased, the pressure drop also increased.

The instabilities in flow boiling should be investigated and evaluated when designing an MCHS. Although the heat transfer can benefit from the fluctuations, mechanical vibrations can cause damage to the system.

2.5 Numerical methods

Technological progress in the field of data capturing has enabled researchers to record the effect of small-scale phenomena on heat and mass transfer more accurately. High-resolution infrared cameras now allow for easier visualisation of temperature distributions within microchannels. However, the current technology is still not able to accurately predict the exact state within a microchannel. The equipment is influenced by the size of channels, the reflective indexes of the channel material and the minuscule time variations. Szczukiewicz et al. (2014) reported that the characteristic times of certain phenomena were smaller than the response times of most thermocouples; one example is bubble nucleation.

Computational fluid dynamics (CFD) allows researchers to investigate the physical phenomena in two-phase flow without expensive equipment. Modelling the molecular level might not be possible, but the errors can be reduced to obtain a solution representing the physical world. New theoretical models can be developed by combining numerical and experimental results (Szczukiewicz et al., 2014). These numerical models can provide valuable insights. Because of the complexity of the models and algorithms available in commercial CFD codes, it is necessary to assess each case to ensure that the most applicable models are implemented.

To solve a CFD simulation, the domain of interest is divided into smaller elements or nodes. The size of the elements has a large impact on the solution of the simulation. This is because the properties, such as velocity and temperature, are uniform within an element, and therefore, small-scale changes in these properties cannot be accurately represented. This can lead to a propagation of error throughout the simulation.

It is important to note that two main types of mesh are used, namely structured and unstructured. The most basic mesh is a structured mesh. This mesh is comparable with a Cartesian grid, and a node's position can easily be identified, similar to a point on a Cartesian grid. It is also generally limited to simple geometries. A structured mesh requires smaller elements to capture all the domain details properly, increasing the resources required with complex geometries. Therefore, complex geometries generally use unstructured meshes. An unstructured mesh has more freedom regarding shape, size and distribution, but the difference in neighbouring elements increases the solution time and can lead to numerical errors (Ferziger & Perić, 2002).

During a simulation, the governing equations are solved within each element at every iteration. This leads to a relation between the solution time, or computational cost, and the number of elements in

the solution domain. To improve the solution time, the number of elements needs to be kept at a minimum. Smaller or finer areas of the domain will require a finer resolution to be accurate, such as the thin liquid film at the microchannel wall (Bordbar et al., 2018). Ensuring that fine mesh resolutions exist in the regions that contain small-scale phenomena becomes difficult when transient simulations are being conducted, because these regions can move around the domain.

The minute scales of the phenomena existing in microchannel flow boiling require very fine mesh elements to be captured accurately. This leads to high computational costs; therefore, most studies are limited to two-dimensional domains. Time is also limited, resulting in most simulations investigating less than a second of flow time. Most of the numerical studies conducted only focus on a single bubble, with very few simulating multiple bubbles. One study investigating two bubbles in the slug flow regime was conducted by Magnini et al. (2013a). They used elongated bubbles that were initially three diameters (3D) in length and separated by a liquid slug of length 6D. They observed that the hydrodynamically disturbed regions extended behind the bubbles but were shorter than the liquid slug. In comparison, the thermally disturbed region was longer than the liquid slug. This improved the time-averaged heat transfer coefficient of the second bubble.

Magnini & Thome (2016) studied various parameters that influence heat transfer such as heat flux, bubble frequency and inlet mass flux. They found that increasing the frequency increased heat transfer, while increasing the mass flux reduced the mass transfer. Table 2-2 lists previous studies on slug flow.

Table 2-2: List of slug flow studies.

Author	Channel Size	Channel Shape	Element Size & Type	Number of Mesh Elements	2-D/3-D
Gupta, Fletcher & Haynes (2009)	0.5 x 5 mm	Axisymmetric	D/100 Inflation layers at the walls Structured	53 000	2-D
Magnini et al. (2013a)	0.5 x 10-36 mm	Axisymmetric	D/300 Uniform Structured	0.9 - 3.24 x10^6	2-D
Magnini, Pulvirenti & Thome (2013b)	1 x 8 mm	Axisymmetric	D/300 Uniform Structured	360 000	2-D
Magnini & Thome (2016)	0.5 x 22.5 mm	Axisymmetric	D/300 Uniform Structured	2 000 000	2-D
Ferrari et al. (2018)	0.5 x10 mm	Axisymmetric	D/300 Uniform Structured	900 000	2-D
	0.1 x 0.1 x 3-5 mm	Square	D_{eq}/125 Inflation layers at the walls Structured	4.7 - 7.9 x10^6 (for a quarter of the domain)	3-D
Liu, Ling, Peng, Li & Duan (2020)	0.3 x 0.3 x 12 mm & 0.3 x 0.3 x 2.1 mm	Square T-section	D/15 Uniform Structured	392 000	3-D

Other studies that have investigated single bubble slug flow include work done by Khodaparast, Magnini, Borhani & Thome (2015) and by Kumari, Kumar & Gupta (2019). Khodaparast et al. (2015) studied the dynamics of isolated bubbles. They investigated the effect of capillary and Reynolds numbers on various parameters such as bubble shape, size and velocity. They found that the curvature of the bubble nose increased as the capillary number increased and that inertial effects were no longer negligible in air-water flows when $Ca > 0.01$.

Kumari et al. (2019) investigated the effects of bubble volume and Reynolds number on bubble shape and heat transfer. They observed that the Nu is at a maximum for a bubble that is close to a perfect sphere and for larger pill-shaped bubbles Nu is independent of the Reynolds number.

The accuracy of two-phase simulations depends on the modelling of the two-phase interface. The most commonly used methods for interface capturing are the volume of fluid (VOF) and level-set (LS). The LS method implements a smooth distance function, ψ, with the interface located at $\psi = 0$. The function is positive in one phase and negative in the other. This method is known to suffer from poor mass conservation (Bonometti & Magnaudet, 2007). The VOF method uses the volume fraction, α, to determine the interface. The values of the volume fraction range from 0 to 1. Where 0 indicates that the cell is only filled by one phase and 1 by the other phase. The interface is located at cells with a value between 0 and 1. VOF methods are conservative but struggle to capture the interface accurately without a very fine mesh.

Interface-capturing methods are commonly used with the single-fluid approach. One set of mass, momentum and energy equations is solved for the entire computational domain as a single phase. These equations are expressed as:

$$\frac{\partial}{\partial t}(\rho) + \nabla \cdot (\rho \vec{u}) = 0 \tag{2.22}$$

$$\frac{\partial}{\partial t}(\rho \vec{u}) + \nabla \cdot (\rho \vec{u} \vec{u}) = -\nabla P + \nabla \cdot [\mu(\nabla \vec{u} + \nabla \vec{u}^T)] + \vec{F} \tag{2.23}$$

$$\frac{\partial}{\partial t}(\rho E) + \nabla \cdot (\rho \vec{u} h) = \nabla \cdot (k \nabla T) \tag{2.24}$$

where $\vec{u}$ is velocity, P is pressure, E is the internal energy, h is enthalpy, k is the thermal conductivity and $\vec{F}$ is the surface tension force. The most popular method used for resolving the effects of surface tension is the continuum surface force (CSF) model. This model is widely implemented in commercial computational fluid dynamics software packages and was proposed by Brackbill, Kothe & Zemach (1992). This type of model interprets the surface tension as a continuous effect rather than assuming a boundary value at the interface. The CSF model can be expressed as:

$$\vec{F} = \sigma \kappa \delta_s \vec{n} \tag{2.25}$$

where σ is the surface tension, κ is the interface curvature, δ_s is the Dirac delta function specifying the interface and $\vec{n}$ is the interface normal vector. The interface normal vector, $\vec{n}$, is defined as the gradient of the volume fraction:

$$\vec{n} = \nabla \alpha, \tag{2.26}$$

and the interface curvature, κ, is the divergence of the unit normal:

$$\kappa = \nabla \cdot \frac{\vec{n}}{|\vec{n}|} \tag{2.27}$$

The weighted average over the two phases is used for fluid properties such as density, viscosity and thermal conductivity. The property values are calculated for each computational cell by using the volume fraction, where $\alpha = 1$ in the primary phase:

$$\rho = \alpha\rho_P + (1-\alpha)\rho_S \tag{2.28}$$

$$\mu = \alpha\mu_P + (1-\alpha)\mu_S \tag{2.29}$$

$$k = \alpha k_P + (1-\alpha)k_S \tag{2.30}$$

The subscripts P and S denote the primary and secondary phases respectively. For cases with phase change, the liquid phase is the primary phase and the vapour phase the secondary. An alternative method is to use the volume fraction, α, which relates to a colour function, C, by the following equation:

$$\alpha = \frac{1}{V}\iiint_v C dv \tag{2.31}$$

where V is the volume. For the case of flow boiling, it is important to account for mass transfer due to phase change. The mass transfer rate, $\dot{m}$, is given by

$$\dot{m} = \rho_S(\vec{u}_S - \vec{u}_i)\cdot\vec{n} = \rho_P(\vec{u}_P - \vec{u}_i)\cdot\vec{n} \tag{2.32}$$

The subscript i indicates the interface value. The mass transfer rate is positive for evaporation and negative for condensation. The following jump conditions are applied to the velocity, momentum transfer rate and energy transfer rate across the interface and are defined respectively as:

$$(\vec{u}_S - \vec{u}_P)\cdot\vec{n} = \dot{m}\left(\frac{1}{\rho_S} - \frac{1}{\rho_P}\right), \tag{2.33}$$

$$\dot{m}(\vec{u}_S - \vec{u}_P) = (\tau_S - \tau_P)\cdot\vec{n} - (p_S - p_P)\boldsymbol{I}\cdot\vec{n} + \sigma\kappa\vec{n} \tag{2.34}$$

and

$$q_i'' = \dot{m}h_{fg} \tag{2.35}$$

where $\boldsymbol{I}$ is an idemfactor. The energy jump equation only accounts for latent heat transfer. When phase change is present, equations 2.33 to 2.35 are generally used at the interface and the conservation equations in equations 2.22 to 2.24 are applied to the interior of each phase.

One of the most widely used models for interfacial phase change is the Rankine-Hugonoit jump condition or the energy jump condition. For this model, the mass transfer rate is based on net energy transfer across the interface; this includes conductive heat transfer to or from the interface:

$$q_i'' = \vec{n}\cdot(k_P\nabla T_P - k_S\nabla T_S) = \dot{m}h_L \tag{2.36}$$

The volumetric mass source term, S, is defined as:

$$S_S = -S_P = \dot{m}|\nabla\alpha_S| \tag{2.37}$$

where $|\nabla\alpha_S|$ for a specific cell is calculated from

$$|\nabla\alpha_S| = \frac{1}{V}\int|\nabla\alpha_S|\,dV = \frac{A_{int}}{V} \tag{2.38}$$

where A_{int} is the interfacial area within the cell and V is the cell volume. Equation 2.37 was simplified by Nichita and Thome (2010) as:

$$S_S = -S_P = \frac{(k_S\alpha_S + k_P\alpha_P)\,(\nabla T \cdot \nabla \alpha_P)}{h_L} \tag{2.39}$$

Equation 2.39 is less accurate because of assumptions regarding the relation between thermal conductivity and bubble growth. When boiling, the liquid phase is saturated and the vapour phase unsaturated because it can be superheated. While condensing, the vapour is saturated and the liquid unsaturated since it can be subcooled. To account for this, Sun, Xu & Wang (2012) proposed the following equation based on the assumption of zero-heat conduction in the saturated phase:

$$S_{sat} = -S_{unsat} = \frac{2k_{unsat}(\nabla \alpha \cdot \nabla T)}{h_L} \tag{2.40}$$

where the saturated phase is indicated by the subscript sat and the unsaturated phase by the subscript $unsat$. Another model for mass transfer is the Schrage model proposed by Schrage (1953), which is based on the kinetic theory of gases. The model is developed on the assumption that both the liquid phase and the vapour phase are saturated, as well as allowing a temperature and pressure jump across the interface, $T_{sat}(p_P) = T_{P,sat} \neq T_{sat}(p_S) = T_{S,sat}$.

The number of molecules undergoing phase change and crossing the interface is defined by a fraction γ, and the reflected molecules are defined as $1 - \gamma$. The fractions involving condensation and evaporation are defined as:

$$\gamma_c = \frac{number\ of\ molecules\ absorbed\ by\ liquid\ phase}{number\ of\ molecules\ impinging\ on\ liquid\ phase} \tag{2.41}$$

and

$$\gamma_e = \frac{number\ of\ molecules\ transferred\ to\ vapour\ phase}{number\ of\ molecules\ emitted\ from\ liquid\ phase} \tag{2.42}$$

where the subscript *c* indicates condensation and *e* evaporation. Perfect condensation occurs when $\gamma_c = 1$ and perfect evaporation when $\gamma_e = 1$. The mass flux for this model is determined by

$$\dot{m} = \frac{2}{2 - \gamma_c}\sqrt{\frac{M}{2\pi R}}\left[\frac{\gamma_c p_S}{\sqrt{T_{S,sat}}} - \frac{\gamma_e p_P}{\sqrt{T_{P,sat}}}\right] \tag{2.43}$$

where R is the universal gas constant [8.314 J/mol K], M the molecular weight and the pressures and saturation temperatures of the phases at the interface. When the condensation and evaporation fractions are considered equal, they can be represented by a single accommodation coefficient γ, equation 2.26 can then be simplified to

$$\dot{m} = \frac{2\gamma}{2 - \gamma}\sqrt{\frac{M}{2\pi R}}\left[\frac{p_S}{\sqrt{T_{S,sat}}} - \frac{p_P}{\sqrt{T_{P,sat}}}\right] \tag{2.44}$$

The greatest challenge of this model is the unknown value of γ. Attempts have been made to ascertain its value, with varying results for different scenarios. The relationship was further simplified by Tanasawa (1991) under the assumption that the local mass flux is linearly dependent on the temperature jump between the interface and the vapour phase when this temperature jump is small:

$$\dot{m} = \frac{2\gamma}{2 - \gamma}\sqrt{\frac{M}{2\pi R}}\left[\frac{\rho_S h_L (T - T_{sat})}{T_{sat}^{3/2}}\right] \tag{2.45}$$

T_{sat} is calculated at the local pressure. The volumetric mass source term for the Schrage model is also calculated using equation 2.37. The gradient of the volume fraction in equation 2.37 ensures that evaporation only occurs at the interface. However, the small cell sizes required in microscale flow concentrate the mass transfer to a very small area. This can lead to negative volume fractions because more liquid attempts to evaporate than that which exists in the cells. For this reason, the Tanasawa (1991) model in its original form is unsuitable for microscale flow (Kharangate & Mudawar, 2017). To solve this, a smear source term model was proposed by Hardt & Wondra (2008). This model conserves mass transfer across the interface, while limiting the source terms to the pure phase regions.

For a microchannel heat sink, slug flow is the most commonly investigated flow-boiling regime, and one of the most-used models was developed by Thome (2004). This model attempts to simulate heat transfer during slug flow while the bubbles move past the area of interest. For this model, the microchannel is divided into three regimes, each with its own HTC. First, a liquid slug flows over the area of interest, then an evaporating elongated bubble, and finally, a vapour slug. It is assumed that numerous bubbles will start to nucleate on the microchannel wall. The bubbles only detach and join the bulk flow after their radii have grown and reached the other walls. Then they continue to grow in the axial direction. The flow is then in the slug regime with alternating vapour and liquid slugs.

Magnini et al. (2013b) studied the hydrodynamics and heat transfer of slug flow in an axisymmetric domain. They reported that the largest increase of the HTC occurred at the minimum thickness of the liquid film, which is generally at the rear of the bubble. The increase also disturbed the thermal boundary layer in the wake. This was expanded upon by Ferrari et al. (2018), who investigated slug flow in a square channel. They found that the higher slug velocity and the lower film thickness compared well with circular channels due to the fluid moving into the corners of the channel.

As mentioned earlier, finer details in the flow field require a finer mesh resulting in a higher computational cost. To reduce computational costs without losing accuracy, mesh adaption can be applied. Refinement should be applied to areas such as the liquid film near the channel wall or where gradients change over a small area, such as the liquid-vapour interface. Gupta et al. (2010) recommended that elements with an aspect ratio of 1 should be used in the interface region. This is to ensure accurate and mesh-independent interface capturing. If the aspect ratio is too large, it can cause errors when calculating the surface tension force. These errors lead to spurious currents near the channel wall, which do not exist in a physical system. These spurious currents are illustrated in Figure 2-7.

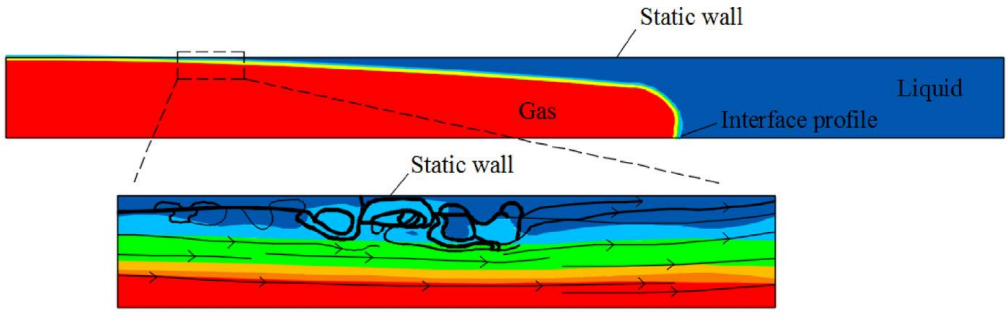

Figure 2-7: Spurious currents in slug flow simulation (Bordbar et al., 2018).

Dynamic mesh adaptions have been employed with interface tracking. This approach remeshes at a set interval of time steps to accurately capture the interface without wasting computational resources in the single-phase regions. The adaption method is based on the error that is expected to

occur over the cell size and the gradient of the specific area. The expected two-dimensional error is calculated with the following equation:

$$|e_{i1}| = (A_{cell})^{\frac{r_g}{2}} |\nabla f| \quad (2.46)$$

where e is the associated error, A_{cell} is the area of the cell, r_g is the gradient volume weight, and ∇f is the Euclidean norm of the gradient of the adaption metric. The isovalue option uses the adaption metric, while the curvature option of the gradient adaption approach uses the second derivative of the chosen metric.

Adaptive meshing is used to reduce the expected error. From equation 2.46, it can be seen that the cell area and the gradient are used to determine the error. The best way of improving the error is by reducing the cell area because the gradient influences the solution. Ansys Fluent has a default adaption procedure, which can be based on several parameters. For two-phase flow simulations, the gradient of the volume fraction is the commonly used parameter. Using the gradient of the volume fraction allows refinement of the cell located in the interface. This method was implemented in studies by Fondelli, Andreini & Facchini (2015) and Mehdizadeh, Sherif & Lear (2011).

Mehdizadeh et al. (2011) recreated a previous study on slug flow with a 96% reduction of cells by implementing adaptive mesh refinement. Their study was based on a uniform two-dimensional axisymmetric mesh with a base cell size of 50 µm. The cells around the interface were refined eight times, achieving a size of 6.25 µm. The adaption metric was the gradient of the volume fraction, and refinement was applied every five time steps to cells with a value above 0.1. A similar method was used on a macroscale model, allowing for larger cells, by Fondelli et al. (2015). A dam-break problem was three-dimensionally replicated, proving that mesh adaption could be used in two-dimensional and three-dimensional studies.

Zhou & Ai (2013) studied mesh adaption for moving immersed boundaries. The cases they studied included a swimming fish and vortex shedding. By reducing the number of nodes of the swimming fish model from 749 724 to 60 410, they reported that the adaptive mesh had a solution time of one-tenth that of the uniform mesh. Bayareh, Nasr Esfahany, Afshar & Bastegani (2020) further confirmed that implementing an adaptive mesh reduced the computational time.

An alternative method of mesh adaption is a moving mesh. Jafari & Okutucu-Özyurt (2016) used this method and produced accurate results. As the bubble grew, the cells at the interface were stretched and deformed. Once the cells were significantly deformed the mesh was regenerated to ensure accuracy. Each of the various methods of mesh adaption should be adjusted to suit the investigation better. The improved effectiveness of an adaptive mesh over a static mesh has proved its value.

2.6 Applications

As technology advanced and production methods improved, it led to the development of smaller, more powerful electronic components, resulting in circuits with a higher heat output and a smaller contact surface for heat sinks. Sufficient thermal management is required to ensure optimal performance and to prevent the reduction of the component lifespan (Bach, 2014), thus driving the development of various cooling methods to improve heat removal.

The primary characteristic used to evaluate the performance of a heat sink is its thermal resistance and is calculated as follows (Husain & Kwang-Yong, 2008):

$$R_{th} = \frac{T_{s,o} - T_{f,i}}{\dot{q} A_S} \tag{2.47}$$

where R_{th} is the thermal resistance [W/m], $T_{s,o}$ is the substrate temperature near the outlet (highest temperature) [K], $T_{f,i}$ is the fluid temperature near the inlet (lowest temperature) [K] and A_s is the exposed area of the substrate [m^2]. Studies on microchannel heat sinks were conducted by researchers such as Tuckerman & Pease (1981) and Husain & Kwang-Yong (2008).

Tuckerman & Pease (1981) developed a silicon substrate water-cooled MCHS with dimensions of 50 µm x 300 µm. They observed a small thermal resistance and a tested heat flux of 790 W/cm^2. Furthermore, they concluded that non-uniform heat fluxes, such as present on integrated chip surfaces, would cause a slight increase in the thermal resistance.

Husain & Kwang-Yong (2008) investigated the optimal shape of a rectangular microchannel. They investigated the influence of aspect ratio on the thermal resistance of their numerical model. They observed a decrease in thermal resistance as the aspect ratio increased. This trend continued until the velocity dominated the convective heat transfer. A reduction of the convective heat transfer area led to an increase in thermal resistance.

The working fluid in an MCHS is crucial to the effectiveness of the system. Kandlikar et al. (2005) proposed the following set of desirable characteristics for the ideal working fluid:

- a saturation pressure slightly higher than atmospheric conditions;
- high latent heat capacity;
- good thermophysical properties, such as high conductivity and low viscosity;
- high dielectric constant, if used in contact with computer chips;
- chemically stable;
- not reacting with commonly used materials in the system;
- safe for human and material exposure when accidental leaks occur.

Applications of microchannel heat exchangers include micromixing in chemical reactors, cryogenic systems and even waste heat recovery for smaller-scale systems (Ohadi, Choo, Dessiatoun & Cetegen, 2013). The operating temperature of the circuit should be taken into account, along with the surrounding temperature. Heliostats and solar dishes used in concentrated solar power plants are examples of high-temperature applications.

2.7 Conclusion

Two-phase flow microchannel heat sinks show great potential in satisfying the need for a small and effective heat exchanger. Although there is much interest in microchannel flow boiling, the size of the channels makes experimental research difficult. Obtaining accurate measurements for temperature, pressure and heat flux is problematic, and visualisation is challenging. Experimental studies are generally restricted to circular channels due to manufacturing limitations.

CFD simulations allow for easier investigation on a microscale. This gives researchers the capability to change aspects of the investigation without the need to recreate the channel physically. Numerical models can produce more accurate measurements, and profiles can easily be generated. However, selecting the appropriate schemes and methods along with a proper mesh domain is crucial to obtain accurate results.

This study aims to add to the understanding of how multiple bubbles interact in microchannels. The main focus is to investigate the effect of the distance between the bubbles on the behaviour of the bubbles and the influence on heat transfer. Along with the influence of gravity.

3. Numerical modelling of microchannel flow boiling

3.1 Introduction

There are many models and methods which can be used in numerical investigations, each with its advantages and disadvantages. Therefore, it is essential to have a good understanding of the physics in order to select the appropriate model. This chapter starts with describing the governing equations, discretisation methods and solution procedure used during this study, followed by a discussion of the numerical domain, mass transfer model and the applied mesh refinement method. Finally, a validation is presented of the selected models and methods against a previous numerical study to ensure accurate results.

3.2 Governing equations

To conduct a numerical study, the laws that govern the physical world need to be applied to the system that is being investigated. For fluid dynamics, these governing equations are known as the Navier-Stokes equations. They include the conservation of mass, momentum and energy. These equations are necessary for obtaining a usable solution.

The first equation is the conservation of mass or the continuity equation. This equation ensures that the mass in the system is constant, in other words, mass is neither created nor destroyed:

$$\frac{\partial \rho}{\partial t} + \nabla(\rho \vec{u}) = 0 \tag{3.1}$$

where $\vec{u}$ is the velocity vector of the fluid, containing all three-dimensional components.

The first term accounts for the volumetric change in density of a cell and the second term accounts for mass entering and leaving the cell.

Along with the conservation of mass, an equation is required to guarantee that the momentum stored inside a cell is not destroyed or created:

$$\rho\left(\frac{\partial \vec{u}}{\partial \vec{t}} + \vec{u}.\vec{\nabla}\vec{u}\right) = -\vec{\nabla}P + \mu\vec{\nabla}^2\vec{u} + \rho g + \sigma\vec{\kappa}\vec{n}\delta \tag{3.2}$$

The left-hand side of the equation ensures that the momentum within a cell is balanced, similar to the conservation of mass. The terms on the right are other possible influences on the momentum, namely pressure, viscous dissipation, gravitational head and surface tension.

The third equation is the conservation of energy. This equation is concerned with the conduction, advection or removal of heat via phase change:

$$\rho c_p\left(\frac{\partial T}{\partial t} + \vec{u}.\vec{\nabla}T\right) = k\vec{\nabla}^2T + \vec{\nabla}h_L\dot{m} \tag{3.3}$$

The left-hand side of the equation also operates in a similar manner to the conservation of mass to ensure that the heat inside a cell and the heat entering and/or leaving the cell due to the momentum of the fluid are balanced. The first term on the right represents heat transfer via conduction and the second term represents the absorption of heat at a constant temperature during phase change.

The following two equations are less common in CFD studies but just as necessary for this study. The first equation is a standard advection equation to monitor the movement of an arbitrary user-defined scalar, ∅:

$$\frac{\partial \emptyset}{\partial t} + \nabla . \emptyset \vec{u} = \emptyset \nabla . \emptyset \tag{3.4}$$

This equation is used for both the mass transfer and mesh refinement models used in this study.

The other critical equation is the volume fraction advection equation, which ensures that the volume fraction is conserved (it is always between 0 and 1):

$$\frac{1}{\rho}\left[\frac{\partial}{\partial t}(\alpha\rho) + \nabla . (\alpha\rho\vec{u})\right] = \frac{1}{\rho_L}[S_\alpha + \dot{m}_V - \dot{m}_L] \tag{3.5}$$

The left-hand side of the equation is an advection equation, which governs the volume fraction entering or leaving a cell due to the fluid movement. The right-hand side ensures that the volume fraction is conserved during condensation, evaporation or other applied source terms.

The following assumptions are made to simplify the equations, making them easier to solve. Both the liquid and gas are incompressible (constant ρ), viscous ($\gamma \neq 0$) and immiscible, and the interfacial surface tension is constant (constant σ).

The Reynolds number (Re) used in this study is within the laminar range and the turbulence modelling is accordingly set to laminar. The multiphase method used in the study is the volume of fluid (VOF) method. This method treats the two phases as non-interpenetrating fluids with a clearly defined interface. This model assigns each part of the domain a value that is generally either 0 or 1. This represents the volume fraction of the two fluids and is denoted with α. The single-fluid properties of the bulk fluid can then be calculated by using α and the properties of the two phases with the following equation:

$$\overline{\emptyset} = \emptyset_L \alpha + (1 - \alpha)\emptyset_V \tag{3.6}$$

where ϕ can represent ρ, μ, k or c_p and the superscript $\overline{\ }$ shows the use of the single-fluid approach.

Only a single set of conservation equations must be solved with values for the bulk fluid flow during each iteration.

Once the assumptions and single-fluid approach are applied, the equations are transformed into the following forms:

$$\nabla(\vec{u}) = 0 \tag{3.7a}$$

$$\bar{\rho}\left(\frac{\partial \vec{u}}{\partial \vec{t}} + \vec{u}.\vec{\nabla}\vec{u}\right) = -\vec{\nabla}P + \bar{\mu}\vec{\nabla}^2\vec{u} + \bar{\rho}g + \sigma\vec{\kappa}\vec{n}\delta \tag{3.7b}$$

$$\bar{\rho}\bar{c_p}\left(\frac{\partial T}{\partial t} + \vec{u}.\vec{\nabla}T\right) = \bar{k}\vec{\nabla}^2 T + \vec{\nabla}h_L\dot{m} \tag{3.7c}$$

$$\frac{\partial \emptyset}{\partial t} + \nabla . \emptyset \vec{u} = \emptyset \nabla . \emptyset \tag{3.7d}$$

$$\frac{1}{\bar{\rho}}\left[\frac{\partial}{\partial t}(\alpha\bar{\rho}) + \nabla . (\alpha\bar{\rho}\vec{u})\right] = \frac{1}{\bar{\rho}}[S_\alpha + \dot{m}_V - \dot{m}_L] \tag{3.7e}$$

These five equations are crucial to a stable solution and the results being physically sound.

3.3 Discretisation methods and solution procedure

The governing equations of the system are solved for each cell during every iteration. Some of the quantities can be obtained directly from the domain. However, there are many terms containing gradients and because the domain is broken up into cells, these gradients cannot be obtained but need to be approximated.

Ansys Fluent has several discretisation methods and solution strategies available to use. Each with its advantages and disadvantages. For this study, the pressure-based solver was used and the PRESTO! (PREssure Staggered Option) scheme was applied to calculate the pressure. The PRESTO! scheme uses a discrete continuity balance to obtain the pressure at each cell face.

The continuity equation is reformatted with a predictor-corrector method to couple the pressure and velocity after the continuity balance is conducted. The pressure-velocity coupling is done with the PISO (Pressure-Implicit with Splitting of Operators) method. The PISO method makes both neighbour and skewness corrections to ensure that the conservation of mass and momentum equations are balanced.

Second-order schemes are used to calculate the spatial gradients. Second-order upwind schemes are applied to the momentum and energy equations, and a second-order implicit method is used for the volume fraction. The VOF interface is broken up into a cell value between 0 and 1 and a normal unit with each iteration. The interface is then propagated via the advection equation and reconstructed to form a sharp interface. The compressive scheme is used to obtain the volume fraction at the cell faces and to reconstruct the interface. The compressive scheme is a high-resolution second-order scheme. The VOF interface is recreated from the cell values and normal unit related to the cell and its surroundings. The compressive scheme recreates the interface using cell face values, donor cell values and spatial gradients. To account for the pressure gradient and the forces between the phases in the momentum equation, the VOF model applies an implicit body force.

An implicit first-order time-stepping method is applied to advance the time. The time advancement is iterative and solves the mass, momentum, energy, volume fraction and other scalar equations simultaneously until the residuals have converged to a value below 0.0001. The time step is calculated with the limited Courant-Friedrichs Lewy number (CFL) criterion. The following equation is used to calculate the time step (Courant, Friedrichs & Lewy, 1967):

$$CFL = \frac{u\Delta t}{\Delta x} \tag{3.8}$$

For this study, the CFL = 0.25. This time step limitation prevents the information from travelling more than a single mesh element during a time step and ensures that the solution remains stable. An additional limitation of $t_{max} < 1e-6$ s prevents that no more than 1% of liquid evaporates from each cell during a time step.

The solution is initialised with the following steps:

1. The temperature, velocity and pressure profiles are initialised by running a single-phase steady-state case.
2. The simulation is then set to transient and the bubbles are patched into the domain with a refined interface.
3. After the bubbles have been patched, the temperature inside the bubble is set to the saturation temperature and the pressure is set to slightly above the surrounding pressure to account for the influence of surface tension.

4. All equations are turned off and a single iteration is run.
5. The adjust functions are activated one at a time, with an iteration run in between each. This step ensures that all scalar variables are initialised so that when they are required during the solution, a value is available. If no values are present, an Ansys Fluent error occurs and the simulation needs to be restarted.
6. Once all relevant scalar equations are initiated through the adjust functions, the last three scalar equations are initialised by applying the mass and energy source terms and running the calculation for an iteration.
7. Finally, the momentum, volume fraction, energy and scalar equations are reactivated.

The solution is then run transiently and the following steps are followed during each iteration:

1. The first step in each iteration is to run each adjust function in the order in which it is implemented in the UDF.
2. The mass and energy source terms are calculated from the smeared source term.
3. The momentum equations are solved.
4. The mass continuity equation is solved, which is used to update the velocities.
5. The volume fraction equation is solved.
6. The energy equation is solved.
7. The scalar equations for the mass transfer and mesh adaption terms are solved.
8. The system properties are updated.
9. The residuals are checked. If they are above 1e-4, the solution starts again at Step 1. If they are below 1e-4, the solution has converged sufficiently, and it moves on to the next time step.

3.4 Computational domain

The numerical model consisted of two pill-shaped vapour slugs that flowed through the computational domain. Three different domains were used in this study, namely an axisymmetric, two-dimensional planar and three-dimensional domain. The two-dimensional domains (axisymmetric and planar) had three sections: an adiabatic section at the inlet, followed by a heated section in the middle and another adiabatic section at the outlet. Figure 3-1 is an illustration of the two-dimensional domain. The three-dimensional domain differed in that it only had two sections, the adiabatic section at the inlet and the heated section. The heated section had a heat flux of 5 kW/m^2 applied. The adiabatic region at the inlet allowed the shape of the slugs to develop before they entered the heated section.

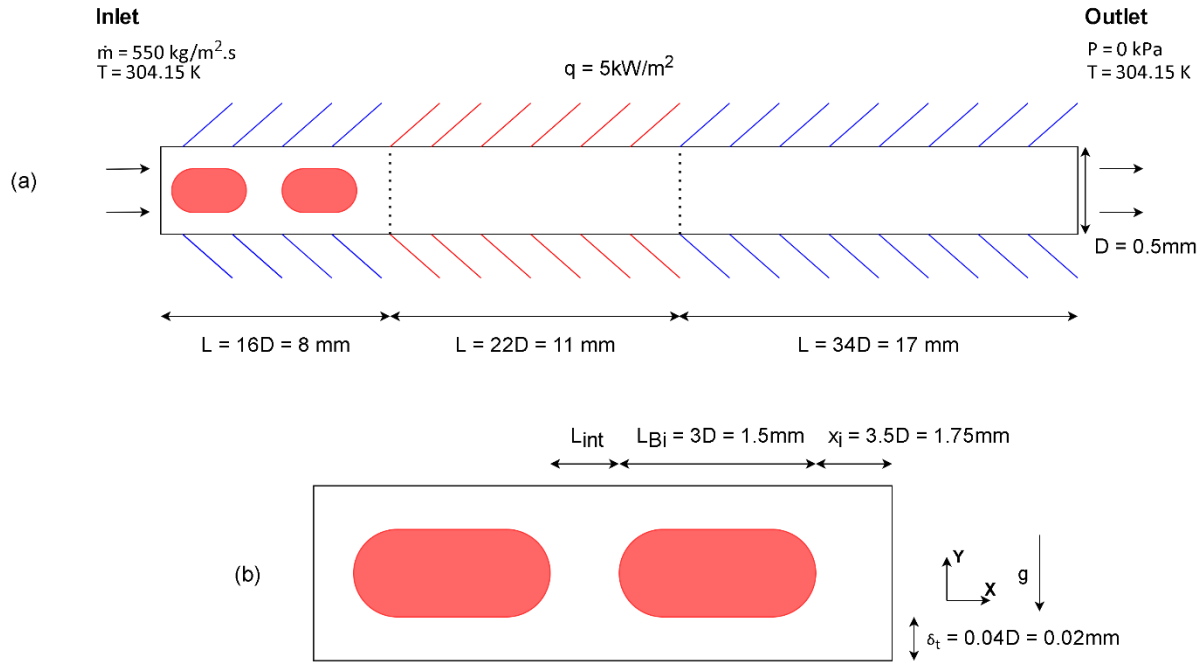

Figure 3-1: Diagram of the two-dimensional domain with (a) illustrating the full domain and boundary conditions and (b) an enlarged view of the inlet adiabatic region (not to scale).

The channel had a diameter or height (D) of 0.5 mm. The adiabatic inlet region had a length of 8 mm, the heated region was 11 mm long and the adiabatic outlet region was 17 mm in length. The vapour slugs were created by patching 1.5 x 0.46 mm cylinders with rounded ends in the channel. The leading slug was located 1.75 mm (x_i) from the heated section. A uniform mass flux of 550 kg/m^{2}s was applied at the inlet and a constant pressure boundary at the outlet. The system was initialised by running a single-phase case to develop the velocity, temperature and pressure fields. Once developed, the bubbles were patched into the domain and the transient simulation was run for 50 ms.

In all the cases simulated for this study, refrigerant R245fa was used as the working fluid. The properties of R245fa, listed in Table 3-1, were kept constant throughout the simulations.

Table 3-1: Properties of R245fa (adapted from Ferrari et al. (2018)).

Property	Dimensions	Liquid	Vapour
Density	kg/m3	1 322	10.5
Viscosity	µPa.s	375.4	10.5
Specific heat	J/kg.K	1352	926
Conductivity	mW/m.K	88.2	14.4
Saturation temperature	K	304.15	
Surface tension	N/m	13.3	
Latent heat capacity	kJ/kg	187.3	

3.5 Mass transfer

The transfer of mass between the liquid and vapour phases was crucial to the success of this study. Mass transfer is responsible for the boiling phenomenon and the high heat transfer characteristics of flow boiling. To numerically recreate mass transfer is extremely difficult due to a lack of understanding of the mechanisms that drive nucleation, coalescence, evaporation and condensation. This meant that only correlations and approximations based on experimental results could be used.

Most studies employed one of three primary mass transfer models (Kharangate & Mudawar, 2017): the Rankine-Hugonoit jump condition, the Schrage model and the Lee model. Generally, the models are adjusted or simplified to better suit the case under investigation.

The Lee model is the default mass transfer model in Ansys Fluent. This model is better suited for macroscale studies and induces phase change throughout the liquid domain. The Schrage model is the better candidate for focusing the phase change at the liquid-vapour interface and was selected as the basis of the applied mass transfer model. Previous studies using a variation of this model, such as the studies by Ferrari et al. (2018), Liu & Palm (2016) and Magnini & Thome (2016), reported instabilities with the advection of the volume fraction or level-set method. These instabilities were due to the mass transfer inside the interface region.

The Schrage model was first proposed by Schrage (1953) and later simplified by Tanasawa (1991). This study used the Tanasawa version of the Schrage model. It was then used to generate the source term-based model by Hardt & Wondra (2008). The kinetic theory of gases forms the basis of the Schrage model, which relates the mass transfer to the difference in partial pressure across the interface and an accommodation coefficient, ω. The accommodation coefficient is the ratio of excited molecules that cross the interface to the total number of excited molecules that strike the interface. The mass flux is calculated with the following equation:

$$\dot{m} = \frac{2\omega}{2 - \omega}\sqrt{\frac{M}{2\pi R_g}}\left[\frac{P_g}{\sqrt{T_{g,sat}}} - \frac{P_L}{\sqrt{T_{L,sat}}}\right] \tag{3.9}$$

where $\dot{m}$ is the mass transfer [kg/m^3.s], M is the molecular mass [kg/mol], R_g is the gas constant and $\omega = 1$.

Tanasawa (1991) assumed that the mass flux across the interface was linearly dependent on the temperature difference across the interface and that the saturation temperatures of the liquid and vapour phases were equal and constant, $T_{g,sat} = T_{L,sat}$. These assumptions simplify equation 3.9 to the following:

$$\dot{m} = \frac{2\omega}{2 - \omega}\sqrt{\frac{M}{2\pi R_g}}\left[\frac{\rho_g h_L (T - T_{sat})}{T_{sat}^{3/2}}\right] \tag{3.10}$$

When the mass transfer is obtained, the mass source term can be calculated as a function of the interfacial area:

$$S_g = -S_L = \dot{m}|\nabla\alpha| \tag{3.11}$$

where the S_g and S_L are the vapour and liquid mass source terms respectively.

The gradient of the volume fraction in equation 3.11, $|\nabla\alpha|$, is the interfacial area, which ensures that evaporation only occurs at the interface. The tiny cell size required for microscale flows focuses the mass transfer onto a very small area. This small scale can lead to an attempt to evaporate more

liquid than is present in the cell, producing negative volume fractions. The negative values can interfere with the volume fraction advection, making the original Tanasawa (1991) model unsuitable for microscale flow boiling (Kharangate & Mudawar, 2017).

Hardt & Wondra (2008) proposed a model to smear the source terms, which would conserve the net mass transfer across the interface and limit the source terms to their respective pure domains. This model was used by Kunkelmann (2011) and is illustrated in Figure 3-2.

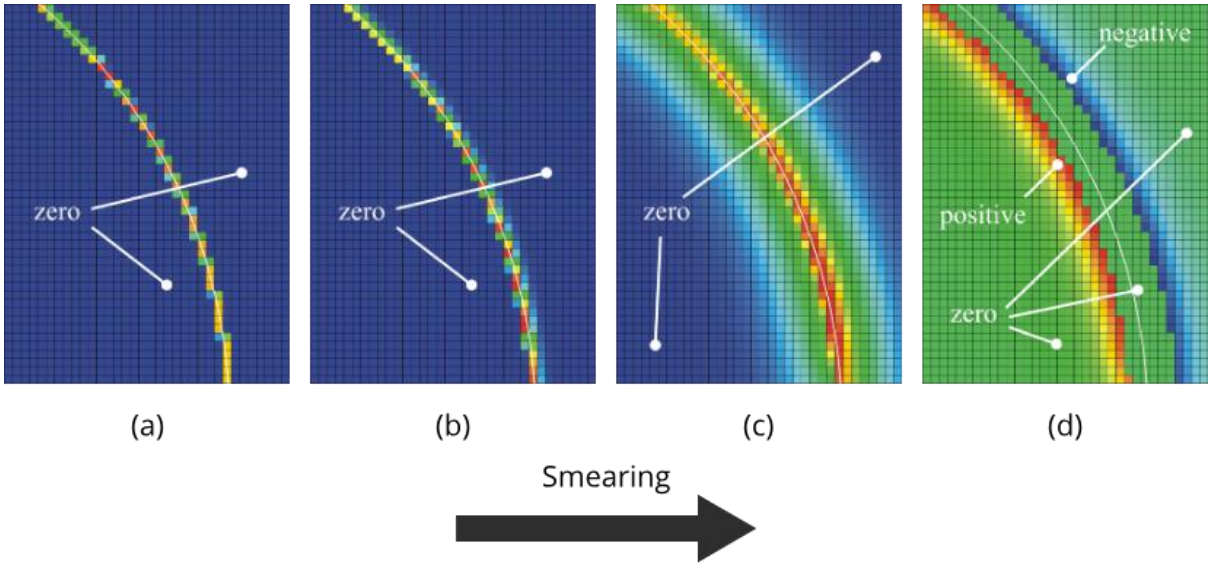

Figure 3-2: Smearing process at the interface, adapted from Kunkelmann (2011).

The following procedure is used to apply the model (Potgieter, 2019):

1. The initial source term is calculated with:

$$\dot{\rho}_0 = N_{to}\dot{m}\alpha|\nabla\alpha| \tag{3.12}$$

where $\dot{m}$ is first obtained from equation 3.10 and N_{to} is a normalisation factor that accounts for the multiplication of α into the equation. This multiplication shifts the source term towards the liquid side of the interface.
N_{to} is calculated as follows:

$$N_{to} = \frac{\int_V |\nabla\alpha| dV}{\int_V \alpha|\nabla\alpha| dV} \tag{3.13}$$

2. The initial source term only exists over two to three cells that comprise the interface. The source term is then smeared, so that a portion of the source term is contained in three to four cells on either side of the interface. The smearing is achieved with the following steady diffusion equation:

$$\dot{\rho}_1 = \dot{\rho}_0 + D\nabla^2\dot{\rho}_1 \tag{3.14}$$

A Neumann boundary condition is set at each boundary. These conditions ensure that there is no discrepancy between the integral of the initial and smeared source terms. The Neumann boundary condition ensures that the scalars have a gradient equal to 0 during the simulations. The zero-gradient forces a zero-flux condition at the boundaries and prevents the scalars from leaving the system.

3. After the source term is smeared, it is bounded on either side and within the interface. If the source term is present inside the interface or in a cell that has not previously been refined, it is set equal to 0. The final source term that is applied in Ansys Fluent is given by:

$$\dot{\rho}\begin{cases} N_v(1-\alpha)\dot{\rho}_1 & if\ \alpha < 0.001 \\ N_L\alpha\dot{\rho}_1 & if\ \alpha > 0.999 \\ 0 & if\ 0.001 \leq\ \alpha\ 0.999 \end{cases} \tag{3.15}$$

where N_v and N_L are the normalisation factors, which ensure that the volume integral of the respective phase source terms is equal to the initial source term.
The normalisation factors are calculated with:

$$N_v = \frac{\int_{V_v}\dot{\rho}_0 dV_v}{\int_V(1-\alpha)\dot{\rho}_1 dV} \tag{3.16}$$

$$N_L = \frac{\int_{V_L}\dot{\rho}_0 dV_L}{\int_V \alpha\dot{\rho}_1 dV} \tag{3.17}$$

where N_v and N_L represent the vapour and liquid phases respectively.

4. When implementing the source terms, mass disappears from the liquid region and reappears in the vapour region. However, the total enthalpy in the regions remains constant, causing heating in the liquid and cooling in the vapour regions. A source term is implemented in the energy equation to deal with the heating, cooling and the enthalpy of formation. The source term is given by:

$$\dot{h} = -\dot{\rho}_0 h_L + N_v(1-\alpha)\dot{\rho}c_{p,v}T - N_L\alpha\dot{\rho}c_{p,L}T \tag{3.18}$$

The mass transfer model is implemented in the UDF (see Appendix A).

To illustrate the importance of the steps and complexity of the mass transfer model above, Potgieter (2019) conducted a couple of benchmark tests. First, he evaluated the Lee model, the default model in Ansys Fluent 19.4. This model causes evaporation in superheated liquid and condensation in subcooled vapour. Figure 3-3 shows a bubble as it enters the heated region, and it clearly illustrates that mass transfer is not limited to the interface. Because mass transfer can occur anywhere in the domain, the model is considered unsuitable for this investigation.

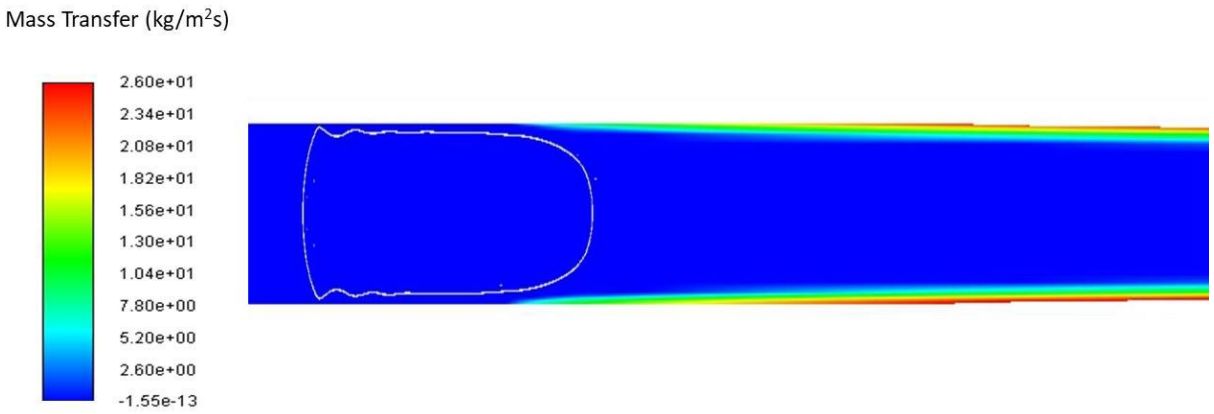

Figure 3-3: Mass transfer using the Lee model with bubble profile outlined in white (Potgieter, 2019).

Secondly, the Tanasawa (1991) model was applied with a UDF rather than the default Ansys Fluent model. The model was applied with no smearing for this test, limiting the mass transfer to the interface. The bubble of this test is illustrated in Figure 3-4.

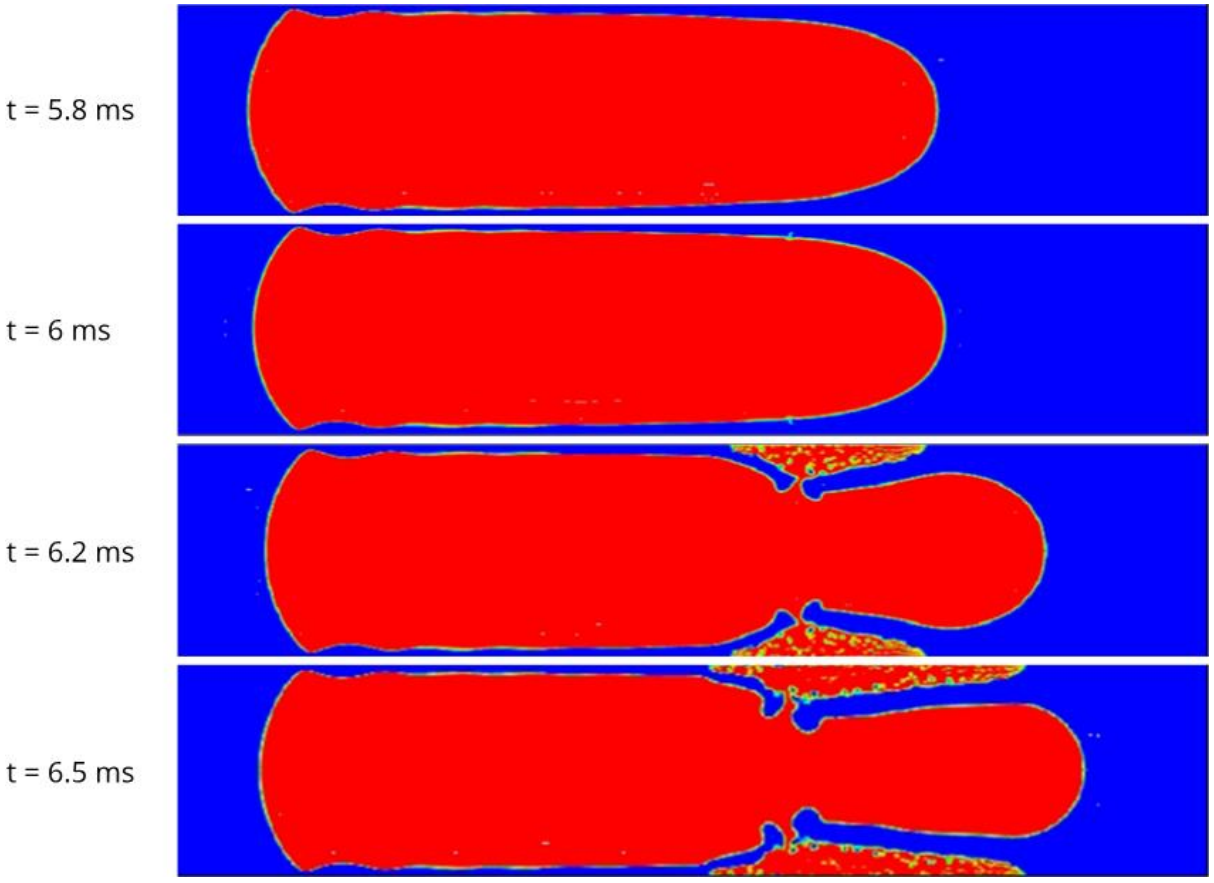

Figure 3-4: Vapour slug profile (red) as it enters the heated region from 5.8 to 6.5 ms without smearing the mass transfer (Potgieter, 2019).

Once part of the interface becomes superheated, the interface breaks down and smears towards the heated region. As time progresses, the surface tension pulls the vapour onto the heated surface, resulting in a large affected area. These results illustrate the necessity of smearing the mass transfer across the interface.

The last test smears the mass transfer, but is not set equal to zero inside the interface. Step 3 above is not applied. The profile of this bubble as it changes over time is shown in Figure 3-5. The slug remains stable for longer when compared with the non-smeared source term. However, the mass transfer present in the interface causes errors. Eventually, the surface tension breaks down again, and the slug deforms.

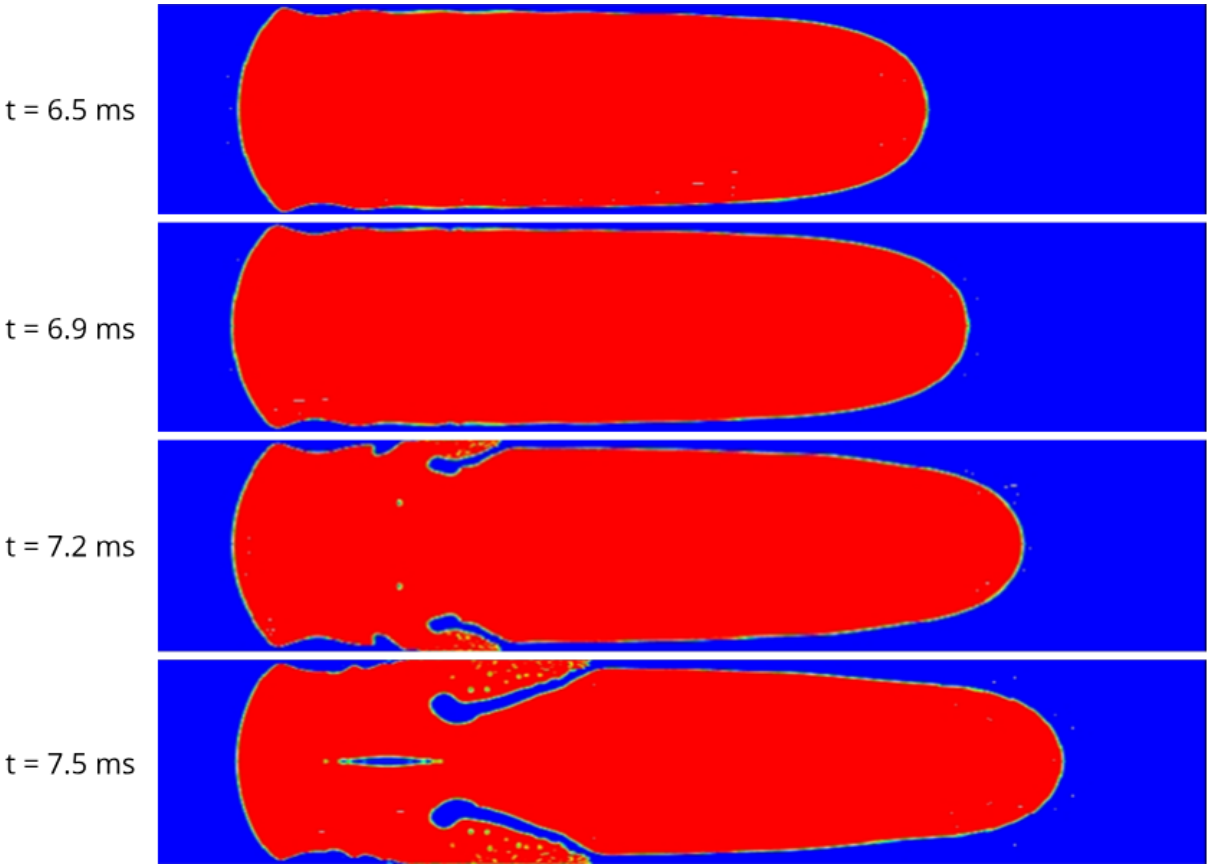

Figure 3-5: Vapour slug profile (red) as it enters the heated region from 6.5 to 7.5 ms without bounding the mass transfer (Potgieter, 2019).

The three tests show the necessity of the chosen mass transfer model, as well as the influence of smearing the initial source term and bounding it to the pure vapour and liquid phases.

3.6 Mesh adaption

The division of the domain under investigation into smaller elements or cells is one of the most significant aspects of CFD simulations. The resolution of the mesh has a direct influence on the accuracy of the solution. The properties of each cell are uniform, which means small changes cannot be captured with large elements or a coarse mesh.

Structured meshes are the simplest. They can be compared with a cartesian grid. Gridlines that originate from the same face never cross each other and they cross gridlines from other faces only once. This allows for easy identification of a cell, similar to cartesian coordinates. This type of mesh is generally used for simpler geometries, as complex domains may require large concentrations of very small low-quality cells. These cells can decrease the accuracy of the solution and waste resources (Ferziger & Perić, 2002).

Complex geometries favour unstructured grids, where the elements can be any shape or size. This type of grid offers more freedom, but large differences between neighbouring cells can lead to

numerical errors and increase the required time for mesh generation and solving the simulation (Ferziger & Perić, 2002).

Due to the influence of the mesh on the solution, an investigation is generally required to ensure that the solution is not dependent on the mesh. One method of ensuring mesh independence is the grid convergence index (GCI) method (ASME, 2009). For this method, a parameter is chosen, e.g. the temperature at the outlet, and evaluated for several different mesh sizes with a constant refinement ratio in all directions. The parameter is then extrapolated to its asymptotic range. When the value tends to 1, it is considered to be independent of the mesh.

Although the size of the mesh elements can be sufficient to obtain an accurate solution, the shape of the elements can still produce numerical errors. Factors that can influence the solution are the aspect ratio, skewness and growth rate of the cells. These aspects are referred to as the mesh quality and can be used to identify the origin of errors.

With each iteration of the computation, the equations are solved for each mesh element, which creates a dependence of computational cost or time on the number of mesh elements. Reducing the number of cells reduces the time required for each iteration; therefore, the number of cells should be kept to a minimum. However, small-scale phenomena and gradients need a finer mesh to be captured accurately; for example, the liquid-vapour interface.

Adaptive mesh refinement can be applied to areas that require a finer resolution. This method changes specific areas of the mesh, either at a set number of iterations or time steps.

The expected error over the cell size and the gradient of the specific area form the basis of the adaption method. The expected two-dimensional error is calculated with the following equation (Potgieter, 2019):

$$|e_{i1}| = (A_{cell})^{\frac{r}{2}} |\nabla f| \tag{3.19}$$

where e is the associated error, A_{cell} is the area of the cell, r is the gradient volume weight, and ∇f is the Euclidean norm of the gradient of the adaption metric.

The goal of adaptive meshing is to reduce the expected error. The area of the cell and the gradient determine the error, as shown in equation 3.19. Changing the gradient will affect the solution, meaning that the best way to reduce the error is by reducing the cell area. Several different parameters can be used for the default adaption procedure in Ansys Fluent, such as temperature and pressure. For two-phase flow simulations, the gradient of the volume fraction is the more common parameter. This parameter refines the cells that are within the liquid-vapour interface. Authors such as Fondelli et al. (2015) used this method for their studies.

A characteristic of numerical investigations into microchannel flow boiling is the presence of spurious currents surrounding the bubble interface. It means that the mass transfer, temperature and velocity gradients cannot be fully captured when only refining the interface. The applied mass transfer is also smeared over three to four cells on either side of the interface. It is crucial that the mass transfer only occurs in the refined region and thus it is necessary to refine this region on either side of the interface. The additional refinement will ensure that the gradients and mass transfer are properly captured and that the liquid film between the vapour slug and the channel wall is fully refined (Vermaak, Potgieter, Dirker, Moghimi, Valluri, Sefiane & Meyer, 2020).

An execution command was used to remesh the domain every five time steps. The remeshing ensured that the cells around the liquid-vapour interface were properly refined to capture the solution

and coarsen cells where the interface was no longer present, preventing high computational costs. A UDF was used to ensure that there were at least four refined cells on either side of the interface at all times, at the same time limiting the spurious currents and mass transfer to the refined region. The number of refined cells around the interface is referred to as δ_M and the level of refinement as δ_L. The number of times required to refine the bulk cells until they have the same size as the cells in the interface is described as the level of refinement. The refinement level and the number of refined cells are illustrated in Figure 3-6.

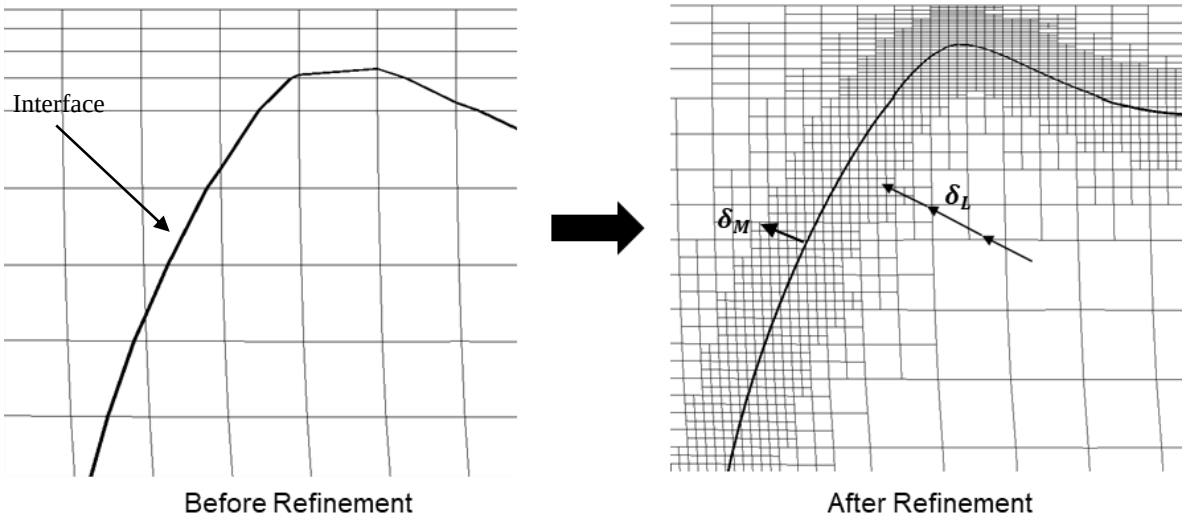

Figure 3-6: Mesh refinement (Potgieter, 2019).

After refinement, the mesh elements had a size of 3µm or D_{min}/160 at the centre of the channel. Several inflation layers were applied at the wall, resulting in the elements having one edge length of D_{min}/160 and one of D_{min}/667 or 0.75µm. The cell sizes were determined by conducting benchmark tests, which are discussed in the following sections.

Potgieter (2019) investigated the main variables of the mesh refinement model, namely the level of refinement (δ_L), the number of cells (δ_M) and the size of the refined cells. To evaluate the refinement level, three cases of different levels of refinement (δ_L = 1, 2 and 3) were compared with a uniform mesh (δ_L = 0). For this test, the number of refined cells was set to δ_M = 4.

The HTC of the heated surface at the end of the simulation and the bubble's position over time were chosen to compare the influence of the factors. There was no significant difference in the HTC as the refinement level was increased. The maximum difference of 5.3% reported was between δ_L = 1 and δ_L = 3. This difference was attributed to the refinement in the inflation layers, which had a smoother transition for δ_L = 3. The bubble's position had a similar trend, with a maximum difference of 2% between the cases.

To investigate the effect of the number of refined cells, four tests were conducted. The first only refined the interface, δ_M = 0, and three tests increased the number of refined cells on either side, δ_M = 2, 4 and 6. The HTC showed little difference between the cases where δ_M = 4 and δ_M = 6, the HTC also became more erratic as the number of cells was reduced. This behaviour was not present for the bubble's position. The cases with refined cells outside the interface had no significant difference. However, the case of δ_M = 0 produced significantly different results. This behaviour was due to the interface leaving the refined region before the mesh was updated every 10 time steps.

Potgieter (2019) concluded that three levels of refinement (δ_L = 3) and four cells on either side of the interface (δ_M = 4) were required to reduce the computational cost while retaining accuracy. These settings produced comparative results with those of the uniform mesh (δ_L = 0) and required 91% less elements.

3.7 Verification and validation

The mesh and discretisation methods used in numerical simulations cause truncation errors, along with the many assumptions and choices of models used. While these errors are unavoidable, they should be limited to ensure that the simulation produces an accurate representation of reality. The results are compared with experimental data or previous numerical studies to verify that the errors are acceptable. After the results are compared and judged to be valid, various cases can be simulated using the same methods and a similar mesh.

Potgieter (2019) used the GCI method to conduct a mesh independence study for four different cell sizes; the sizes were 50, 37.5, 25 and 17 µm. It was reported that the solution was sufficiently independent for a cell size of 25 µm. The larger cell sizes were too coarse to capture the HTC accurately, and there was no significant difference between the smaller sizes. Vermaak et al. (2020) used an identical numerical domain to that of Potgieter (2019) and reported a good comparison between their numerical and experimental results. This study used the same cross-section as Potgieter (2019); therefore, the same mesh settings were used, and no mesh independence study was conducted.

A case was compared with a previous study with a similar domain conducted by Magnini et al. (2013a) to validate this study. The bubbles had an initial spacing of 6D. The average Nu versus position was compared. In this study, time was non-dimensionalised by multiplying the mass flux at the inlet and dividing by the product of the liquid density and the domain diameter/height:

$$\tau = \frac{tG}{\rho_L D} = 0.8320726 * t \tag{3.20}$$

and length was scaled by dividing with the domain diameter/height:

$$L' = \frac{L}{D} \quad or \quad L' = \frac{x}{D} \tag{3.21}$$

The heat transfer coefficient was calculated with the following equation:

$$h = \frac{\dot{q}}{T_{nw} - T_{sat}} \tag{3.22}$$

where $\dot{q}$ is the heat flux [kW/m^2] and the T_{nw} is the near-wall temperature. The Nu was then calculated with:

$$Nu = \frac{hD}{k} \tag{3.23}$$

The Nu was measured along the length of the vapour bubble plus half a liquid slug length in front and behind the bubble, effectively measuring the Nu over the vapour bubble length plus the liquid slug length. The average Nu is plotted against the midpoint of the bubble in Figure 3-7. The Nu produced by the leading bubble is almost identical to the results of Magnini et al. (2013a). Both cases decreased from 14 to 9 (Figure 3-7a). The trailing bubbles showed a larger difference, but the values

were still relatively close together with all the values in the teens (Figure 3-7b). The values for Magnini et al. (2013a) started at 17 and decreased to 13, and those of the current study decreased from 16 to 11. The small differences between the datasets could be due to the method used to calculate the time-averaged values. Magnini et al. (2013a) integrated the HTC over a time interval. In comparison, the current study data were averaged by simply dividing the sum of values for all the data points along this length by the number of data points.

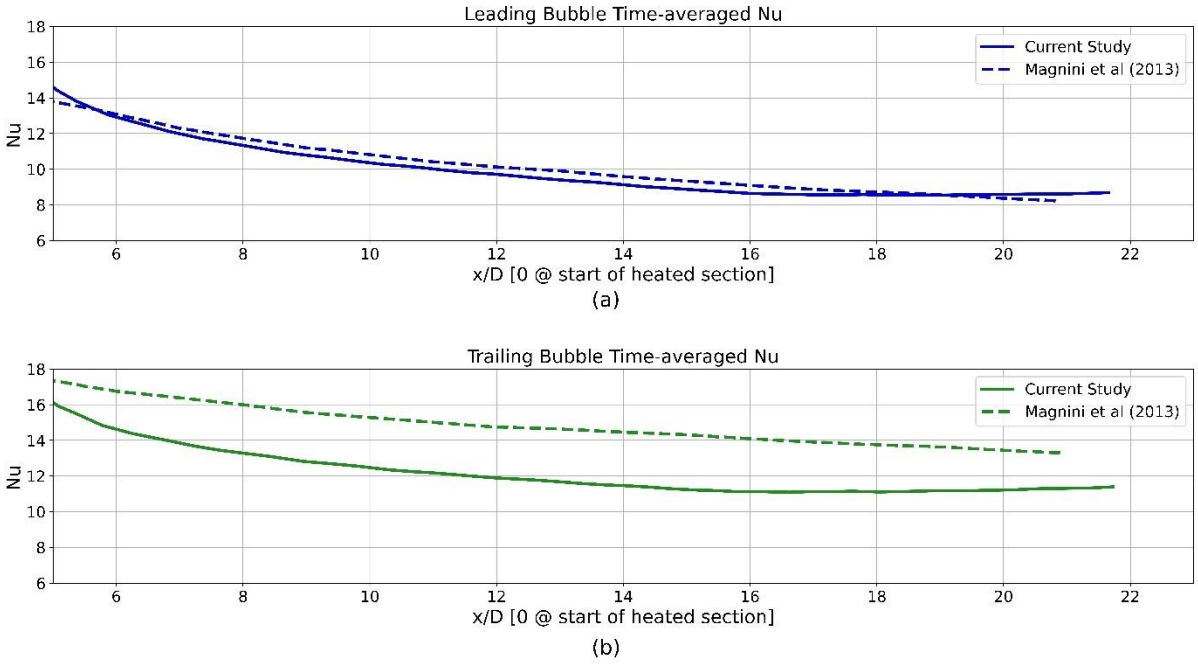

Figure 3-7: Comparing time-averaged Nusselt number (Nu) versus position with Magnini et al. (2013a) for (a) the leading bubble and (b) the trailing bubble.

The results presented here showed a good fit with previously published data and validated the mass transfer model and solver settings. These results were achieved with less than 4% of the mesh elements used by Magnini et al. (2013a).

3.8 Conclusion

This chapter presented the governing equations, discretisation methods and solution process. The mesh refinement model was also discussed. A previous study with a similar domain was reviewed to establish the proper mesh settings. The selected mesh and solver settings could reproduce a previous study accurately, which validated the numerical method used in this study.

4. Results and Discussions

4.1 Introduction

The key characteristic of flow boiling is the phase change of the working fluid as it absorbs heat from the channel walls. Recreating phase change with one of the available mass transfer models is difficult because the movement of the interface and the mass being transferred across this interface can lead to numerical instability.

Due to the difficulty in simulating bubble growth and departure on a heated surface and obtaining a specific initial spacing (L_{int}) between the bubbles, bubble departure was not simulated in this study; the bubbles were rather patched into the domain as pill-shaped vapour slugs (Figure 3-1). This chapter presents the investigation into the effect of the L_{int} on heat transfer and bubble growth. Various cases with different initial spacings were evaluated on both a two-dimensional axisymmetric and two-dimensional planar microchannel. One of the initial spacings was then recreated in a three-dimensional domain in order to investigate the effect of different gravitational orientations. The cross-section of the microchannel had a height of 0.5mm and a width of 5mm.

4.2 Simulation set-up and mesh generation

The domain used for the two-dimensional cases in this study is illustrated in Figure 3-1. The domain for the three-dimensional investigation differed in two ways: first, by the absence of the second adiabatic region and second, only one side was heated. The mesh for the three-dimensional cases is shown in Figure 4-1. The bulk elements of the mesh had an edge length of 25 µm and seven inflation layers around the boundaries. The minimum quality of the mesh was 0.5 and the average 0.89, with a maximum aspect ratio of 4.

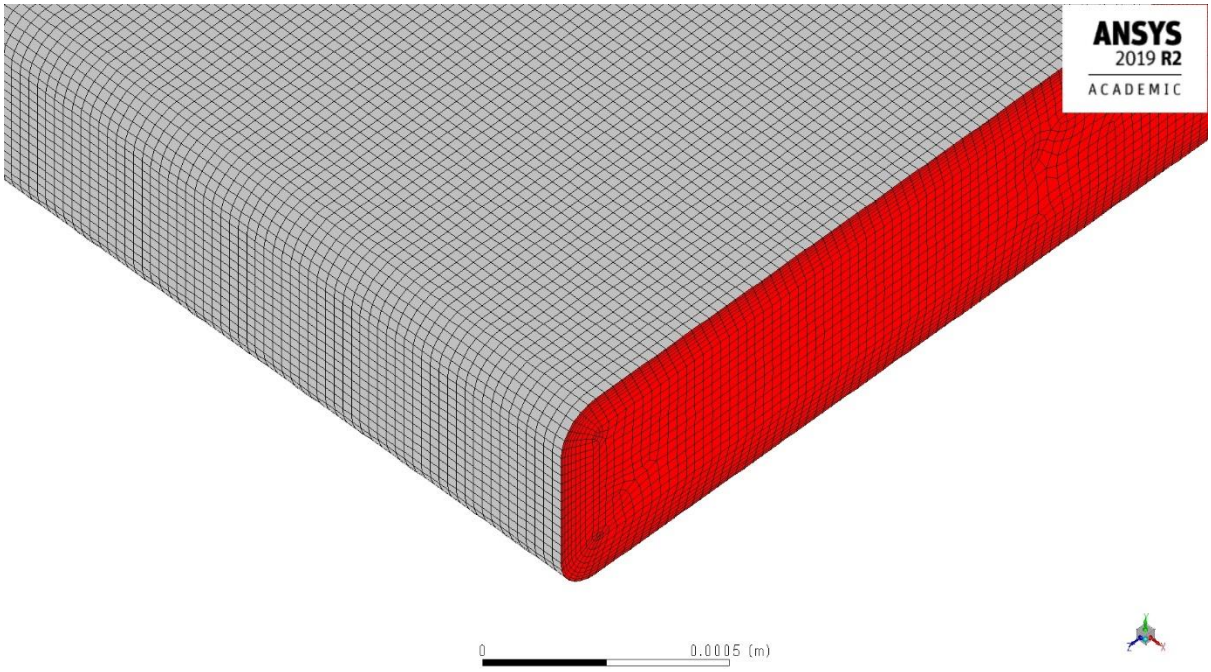

Figure 4-1: Mesh for three-dimensional cases.

The initial profiles for velocity, pressure and temperature were obtained by conducting a steady-state single-phase simulation. The VOF model was then activated, and the bubbles were patched to their initial positions, with the front of the leading bubble at 1.75 mm from the heated section (Figure 3-1). The temperature never exceeded T_{sat} + 4K, leading to the assumptions of constant properties for

both the liquid and vapour phases. The working fluid was R245fa, and the properties are listed in Table 3-1. The specifications of the domain and solver settings are listed in Table 4-1.

Table 4-1: Solver settings and domain specifications.

Numerical simulation settings		
Property		**Specification**
Geometry	2-D	0.5 x 36 mm
	3-D	0.5 x 5 x 19 mm
Mesh	Elements	38 155-125 206 (2-D) $4.49e^{6}$-$32.65e^{6}$ (3-D)
	Maximum size	$2.5e^{-5}$ m
	Minimum size	$7e^{-7}$ m
	Minimum quality	0.5
	Average quality	0.89
	Maximum aspect ratio	4
	Adaption method	UDF
Solver	Type	Pressure-based
	Precision	Double
Multiphase	Model	VOF
	Interface	Sharp
	Evaporation modelling	UDF
	Volume fraction cut-off	1e-6
Turbulence	Model	Laminar
Boundary conditions	Inlet	$\dot{m}$ = 550 kg/m^2.s T = 304.15 K
	Heated surface	q = 5 kW/m^2
	Outlet	Backflow T = 304.15 K P = 0 kPa
Pressure-velocity coupling	Type	PISO
Discretisation	Pressure	PRESTO!
	Time	First-order implicit
	Momentum	Second-order upwind
	Energy	Second-order upwind
	Volume fraction	Compressive/implicit
	User-defined scalars	First-order upwind

Initialisation	Method	Standard
	X-velocity	0.416 m/s
	Y-velocity	0 m/s
	Z-velocity	0 m/s
	Temperature	304.15 K
	Quality	0
Calculation	Flow time	0.05 s (2-D) Not finished (3-D)
	Time step size	$3e^{-7}$-$1e^{-6}$
	Residual convergence	1.00E-4 1.00E-6 (for energy)
	Maximum iterations/time step	40

The same settings and methods listed in Table 4-1 were used in the validation cases.

4.3 Results for two-dimensional cases

Two different scenarios were evaluated during the two-dimensional investigation of this study; the main scenario with two bubbles present and the second with three bubbles present. The two-bubble cases were conducted on both an axisymmetric and a planar domain, while the three bubble cases were only conducted on the planar domain.

The metrics evaluated were as follows: the length of each bubble versus time, the distance between bubbles versus time, the average Nusselt number (Nu) versus position of each bubble and the normalised vapour volume versus time.

4.3.1 Two-bubble cases

The following initial spacings (L_{int}) were investigated in the axisymmetric domain: L_{int} = 1D, 3D, 4D, 5D and 6D. The planar cases had two additional cases for L_{int} = 0.25D and 0.5D.

The initial length of all the bubbles was L_{Bi} = 3D (Figure 3-1). The bubbles started in the adiabatic region to allow the shape to develop before entering the heated section, where phase change became present, which led the bubbles to elongate. For the axisymmetric cases, the leading bubbles reached a final length of between 13 and 14D (Figure 4-2a). All the cases performed similarly, except the case of L_{int} = 1D, which had a sudden jump around τ = 30. This sudden increase was due to the two bubbles merging. The merging of the bubbles is illustrated in Figure 4-2b, and the time frames correspond to the shaded region in Figure 4-2a.

The trailing bubbles followed a similar trend but only achieved a final length of about 12D (Figure 4-3). On closer inspection of Figure 4-3, it would appear that decreasing L_{int} increased the growth rate when the bubbles were in the heated section. This difference in growth rate could be due to the size of the thermal boundary layer. As the leading bubble passed, it disrupted the boundary layer and increased the temperature difference closer to the wall. This increase in temperature difference led to an increase in the heat transfer coefficient.

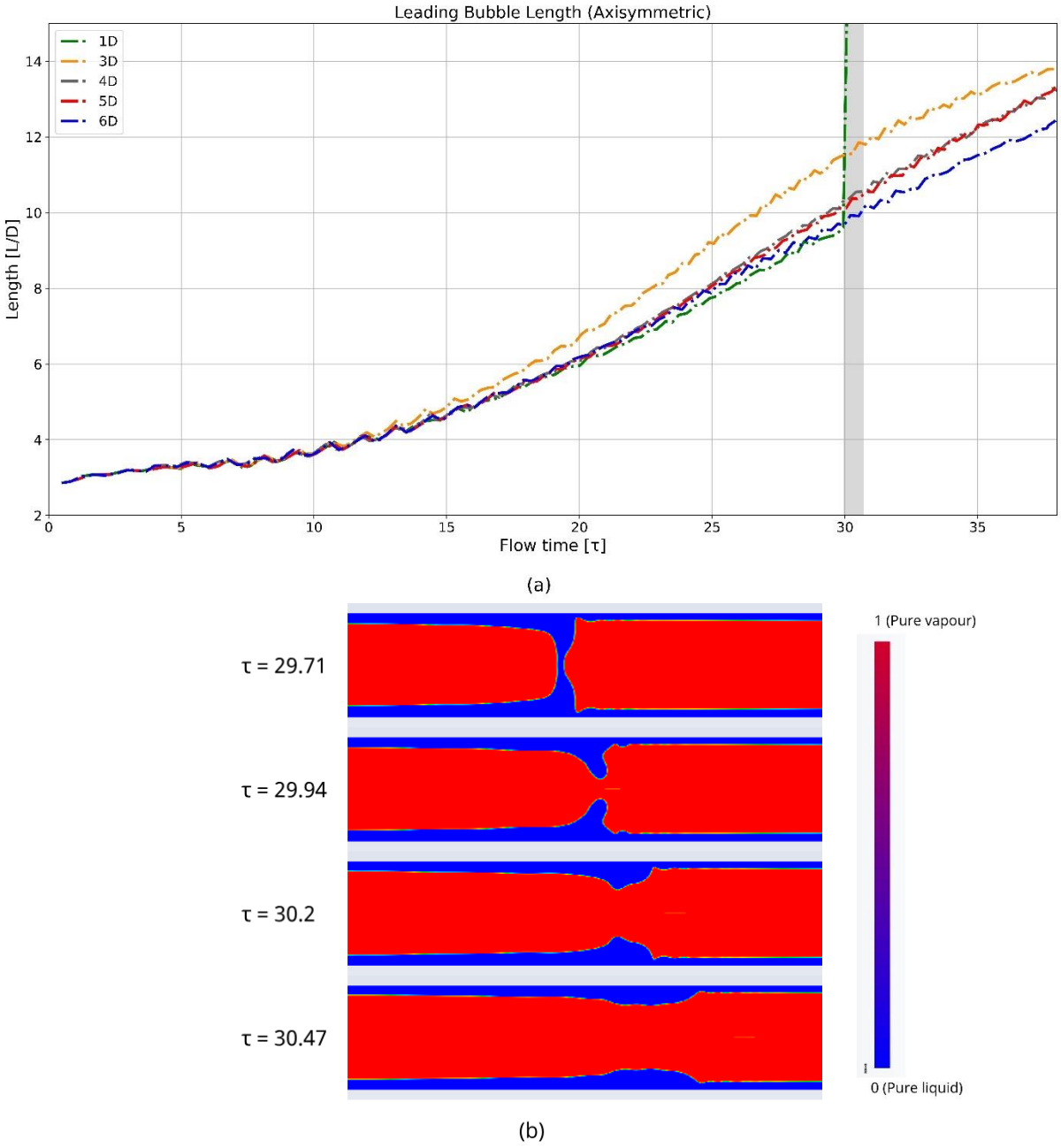

Figure 4-2: (a) Leading bubble length versus time for axisymmetric cases and (b) illustration of the merging bubbles for the case of L_{int} = 1D occurring in the shaded region of (a).

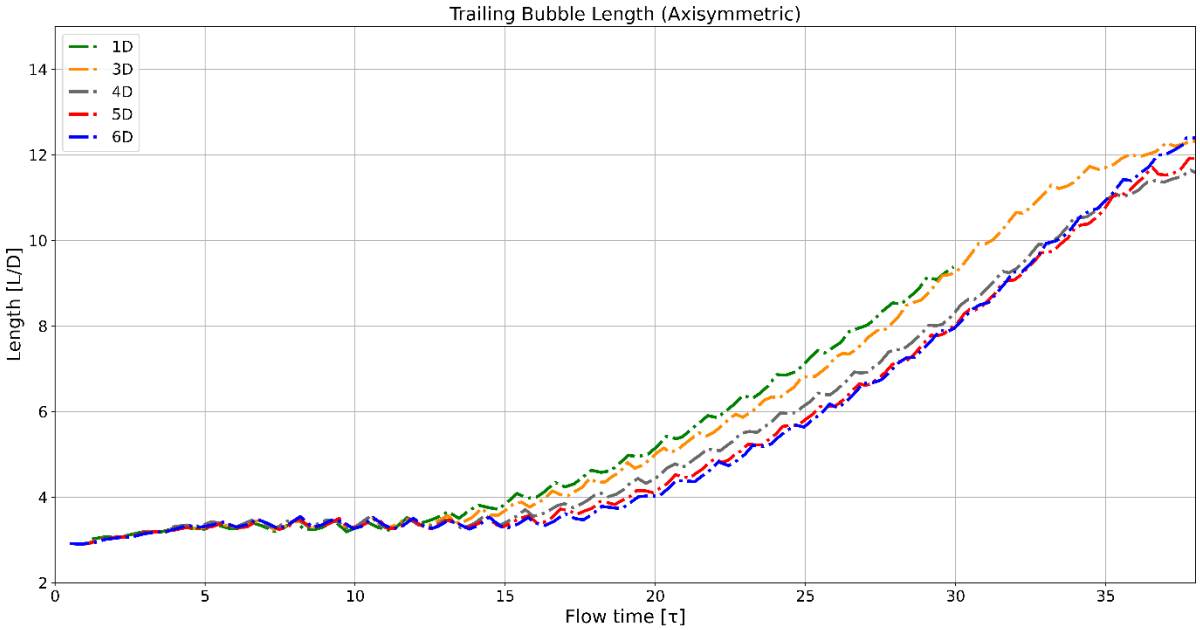

Figure 4-3: Trailing bubble length versus time for axisymmetric cases.

As time progressed, the distance between the bubbles decreased (Figure 4-4a). This decrease was not linear. The initial decrease that was present until $\tau = 5$ resulted from the shape of the bubbles developing. The distance steadily decreased as the bubbles moved along the heated section. The rate of change of the distance increased when both bubbles were near the end of the heated section. The cases for L_{int} = 4-6D had a reduction of 1.5D, and the L_{int} = 3D case had a reduction of 2D. The distance between the bubbles for L_{int} = 1D reached 0 when the bubbles merged.

The fluctuations present in all the graphs where length or distance was evaluated were due to the nature of the bubble tails. The tail of the bubbles constantly changed between concave and convex as it moved through the domain. This fluctuation is shown in Figure 4-4b. These five time frames were taken at the five points marked in Figure 4-4a. The length of the bubbles was measured at the centre of the domain for all the presented cases, which made the measurements especially sensitive to these fluctuations. A Similar behaviour of the bubble tail was observed by Khodaparast et al. (2015) with air bubbles in water. They referred to the change in shape as a flapping motion.

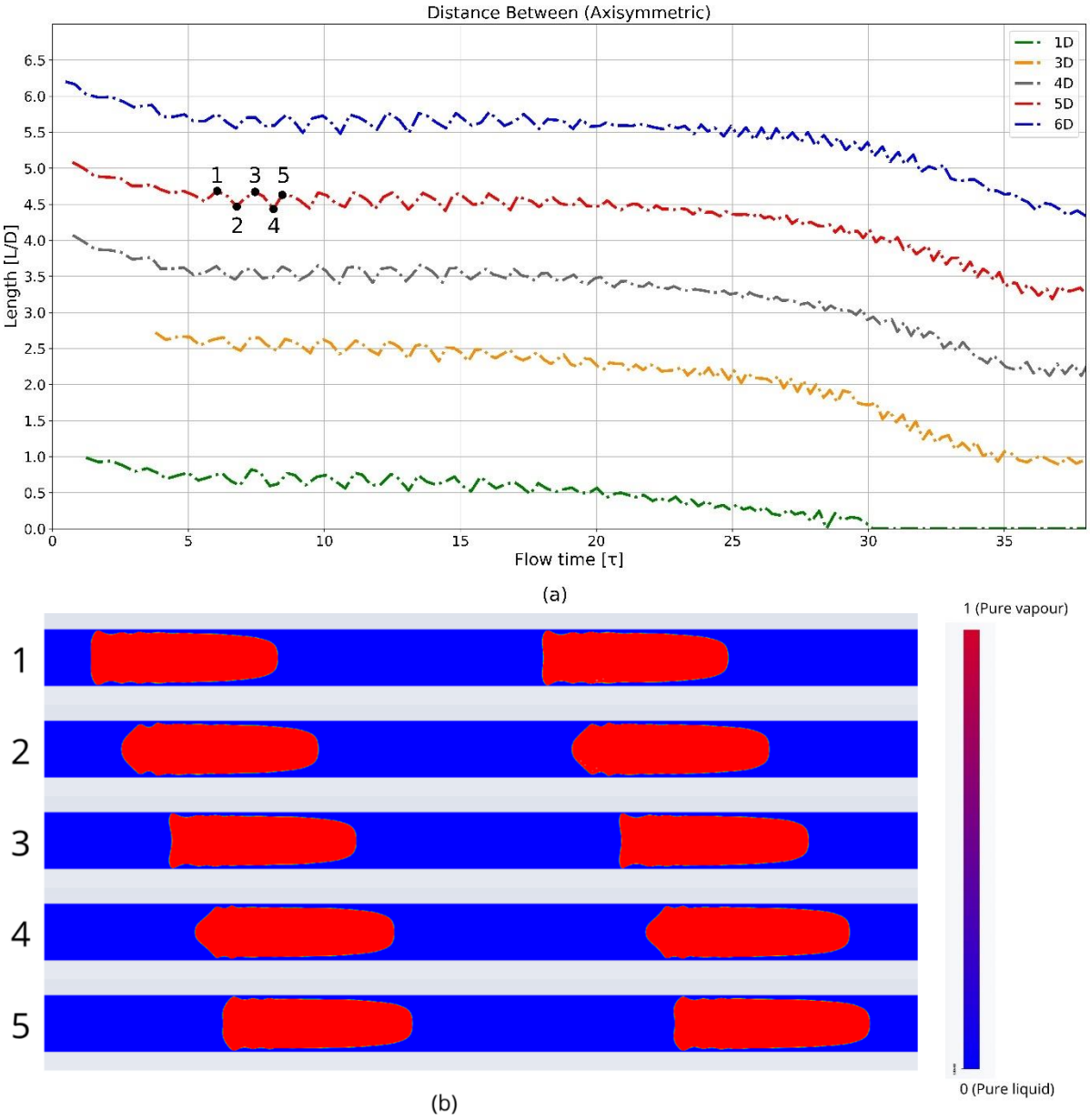

Figure 4-4: (a) Distance between bubbles versus time for axisymmetric cases and (b) illustration of fluctuating bubble tails at corresponding points marked on (a).

The cases conducted in the planar domain can be divided into two groups: the first group for small initial spacings, L_{int} = 0.25-1D, and the second for large initial spacings, L_{int} = 3-6D. There was no significant difference between the behaviour of the leading bubbles (Figure 4-5). The larger spacings reached a slightly longer final length in the range of 6 to 6.5D compared with 5.5 to 6D for the smaller spacings. A more significant difference is present in Figure 4-6, where the trailing bubbles of the smaller spacings achieved a final length of 5.5 to 6.2D. At the same time, the larger spacings only reached a final length of 4.5-5D. The leading bubbles performed identically until τ = 12, after which phase change started to occur in the heated section.

The trailing bubbles behaved differently in the adiabatic region. The larger spacings quickly expanded while developing in shape. Figure 4-7 compares the trailing bubbles for the cases L_{int} = 0.25D and L_{int} = 6D at τ = 7.8. Along with the clear difference in length, a difference in shape is also visible. The trialling bubble of L_{int} = 6D had a sharper nose and was closer in shape to the leading bubble visible

in the L_{int} = 0.25D case. The diameters at the nose of the bubbles also differed, with the longer bubble having a smaller diameter. No phase change occurred during this initial expansion, and Figure 4-7 indicates that the volume did not change. The bubbles seem to elongate due to the flow of the liquid phase, and the amount of elongation is limited by the surface tension. The smaller spacings did not experience this initial expansion as they might be limited by the incompressibility of the shorter liquid slug. The recirculating liquid between the bubbles can also contribute to the limited expansion with the bubbles only growing in the heated section.

The size of the initial spacing had a clear influence on the final length of the trailing bubble. Both Figure 4-3 and Figure 4-6 show a greater increase in bubble length as the initial spacing was reduced. This behaviour in both scenarios supports the argument that smaller spacings benefit from larger temperature differences. Figure 4-8 shows two instances of the thermal boundary at the same position. This figure clearly shows how the leading bubble disturbed the boundary layer. The bubble reduced the thickness of the boundary layer by pushing the liquid forward. The boundary layer was still affected after the bubble had passed due to the presence of the bubble wake. The reduction of the spacing between bubbles reduced the available time of the boundary layer to recover. Therefore, bubbles that were closer took greater advantage of the disrupted thermal boundary layer.

The leading bubbles don't follow a clear trend like the trailing bubbles regarding the final bubble length compared to the initial spacing. In all the cases the leading bubbles enter a steady-state heated section and move through an identical thermal boundary layer. The liquid slug behind the bubble might influence the speed of the bubble and the time spend in the heated section, but not enough to significantly affect the final length of the bubbles.

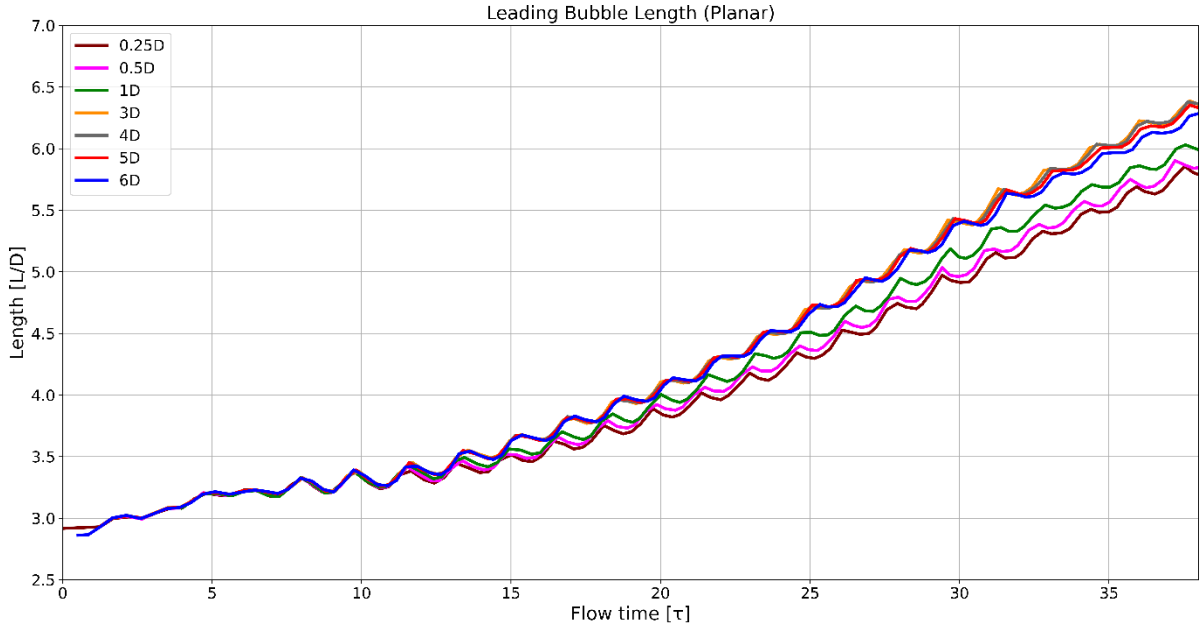

Figure 4-5: Leading bubble length versus time for planar cases.

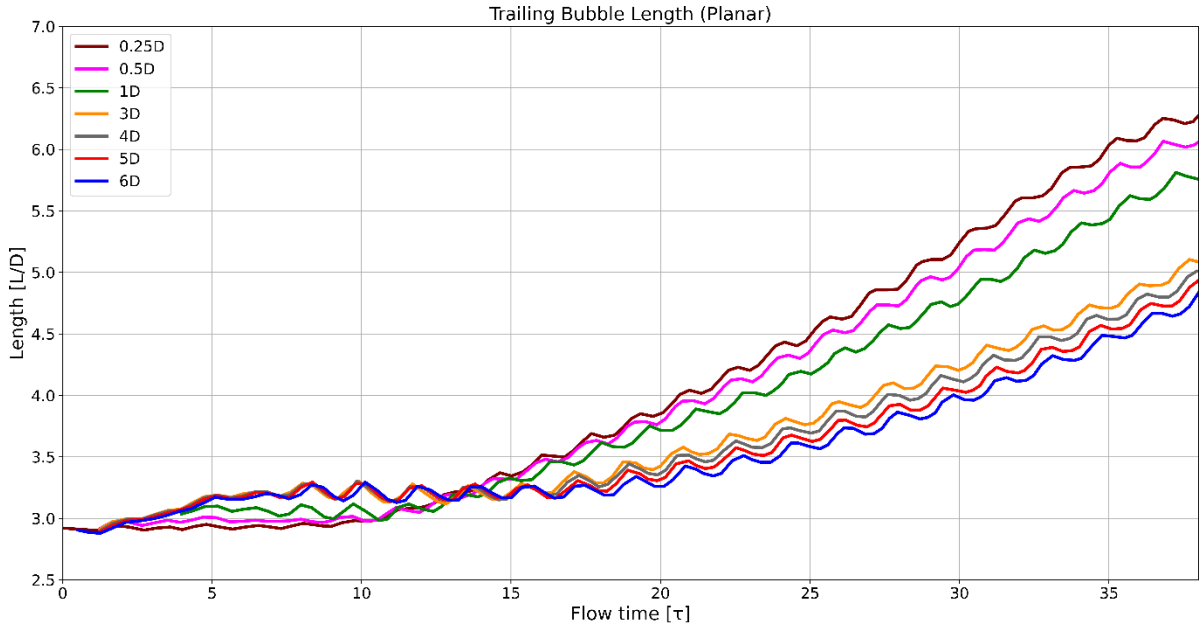

Figure 4-6: Trailing bubble length versus time for planar cases.

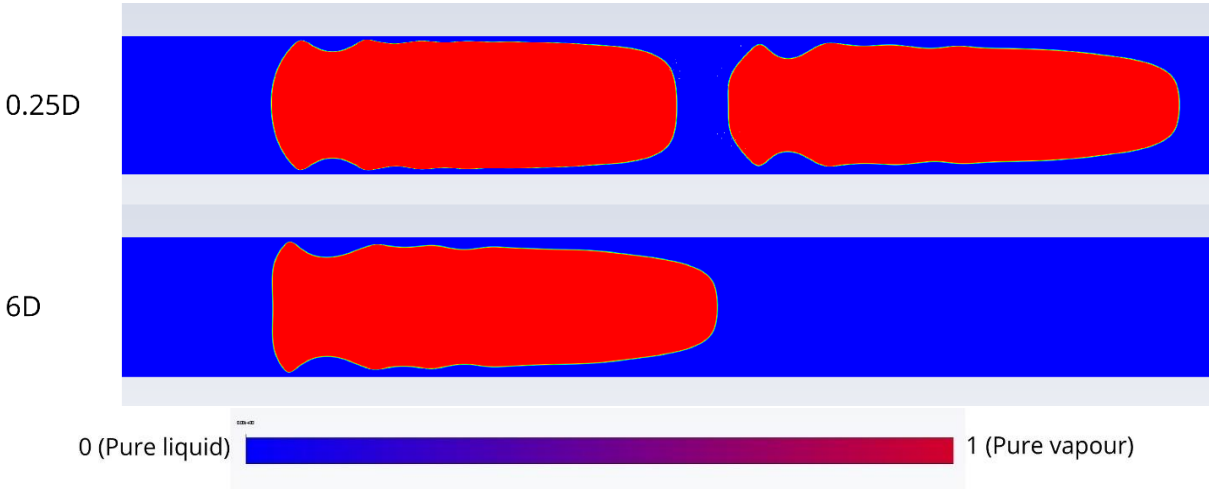

Figure 4-7: Trailing bubbles for L_{int} = 0.25D and L_{int} = 6D at τ = 7.8.

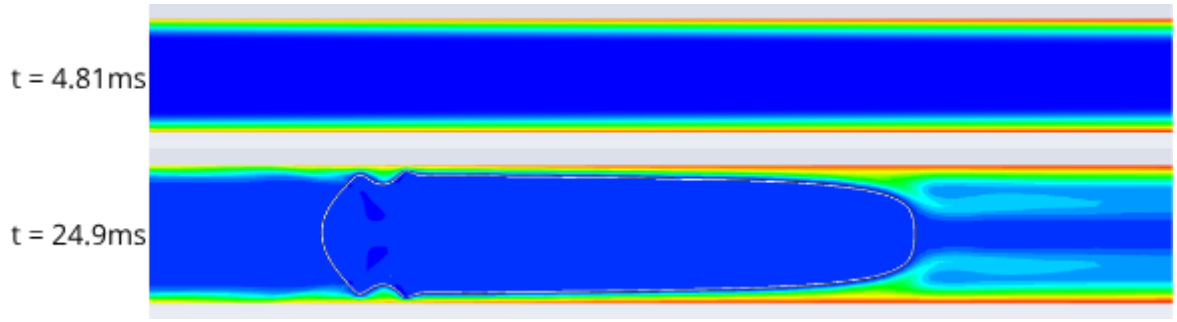

Figure 4-8: Thermal boundary layer for a leading bubble at two different time steps.

The distance between the bubbles did not significantly change over time (Figure 4-9). For the larger spacing, a reduction of less than 0.5D is observed, while an increase of about 0.5D was present in the smaller spacings. This small increase could result from the incompressibility of the liquid slug and the surface tension of the interface. The different gradients at the start corresponded to the bubble shapes developing.

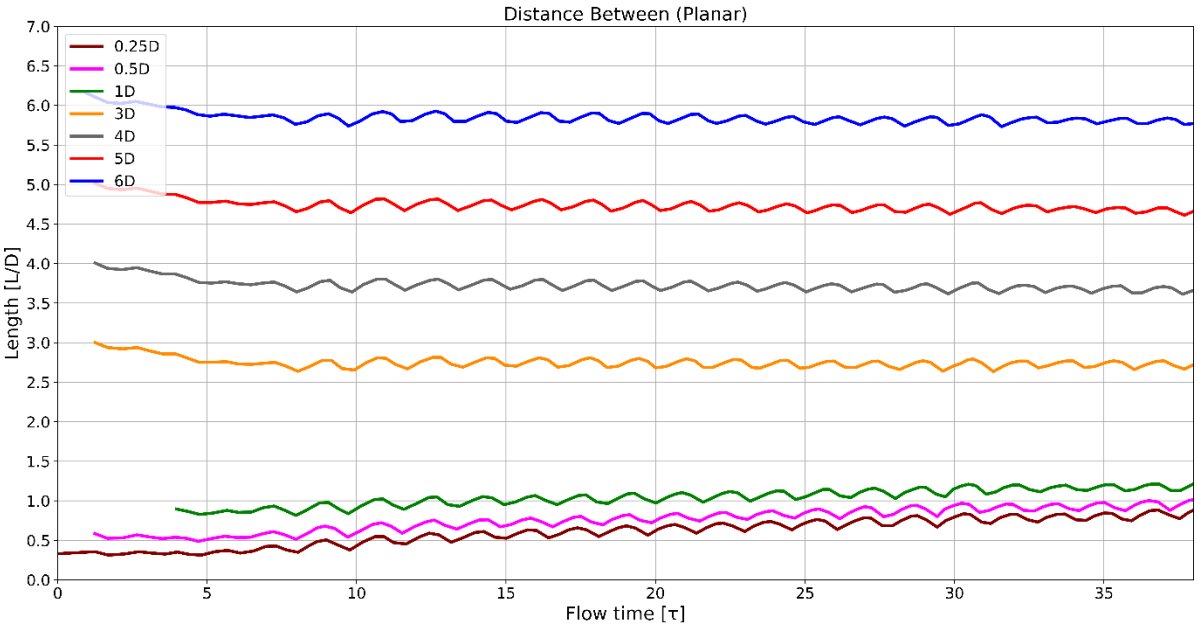

Figure 4-9: Distance between bubbles for planar cases.

The Nu was calculated using equation 3.23 and then averaged along the length of the bubble plus half a liquid slug in front and behind the bubble. Although the leading bubbles developed and grew differently as they moved through the domain (Figure 4-2 and Figure 4-5), their averaged Nu were almost identical. The cases in both the axisymmetric domain (Figure 4-10) and the planar domain (Figure 4-11) roughly followed the line given by the following equation:

$$Nu = 25.5x_H^{-0.4} \tag{4.1}$$

where x_H is the non-dimensionalised length along the heated wall. It is equal to 0 at the entrance of the heated section and calculated as follows:

$$x_H = \frac{x}{D} \tag{4.2}$$

For both cases, the Nu of the leading bubble started high and decreased to below 8. Both the axisymmetric (Figure 4-12) and the planar (Figure 4-13) domains had an overall increase in the Nu of the trailing bubbles. The final value increased to 10 for both domains, which is an increase of 25%. It is difficult to analyse the effect of L_{int} on the Nu when the liquid slug is also considered in calculating the average value, because the Nu is calculated over a longer length for the cases with a longer liquid slug.

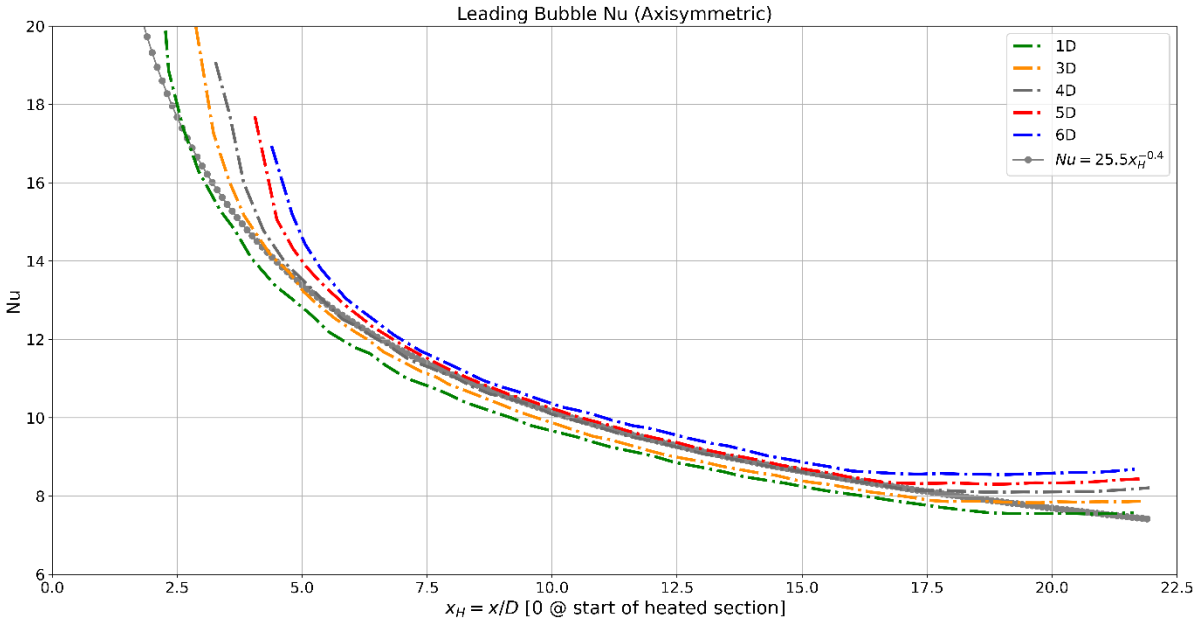

Figure 4-10: Averaged Nusselt number (Nu) of the leading bubble versus the position of the bubble midpoint for axisymmetric cases.

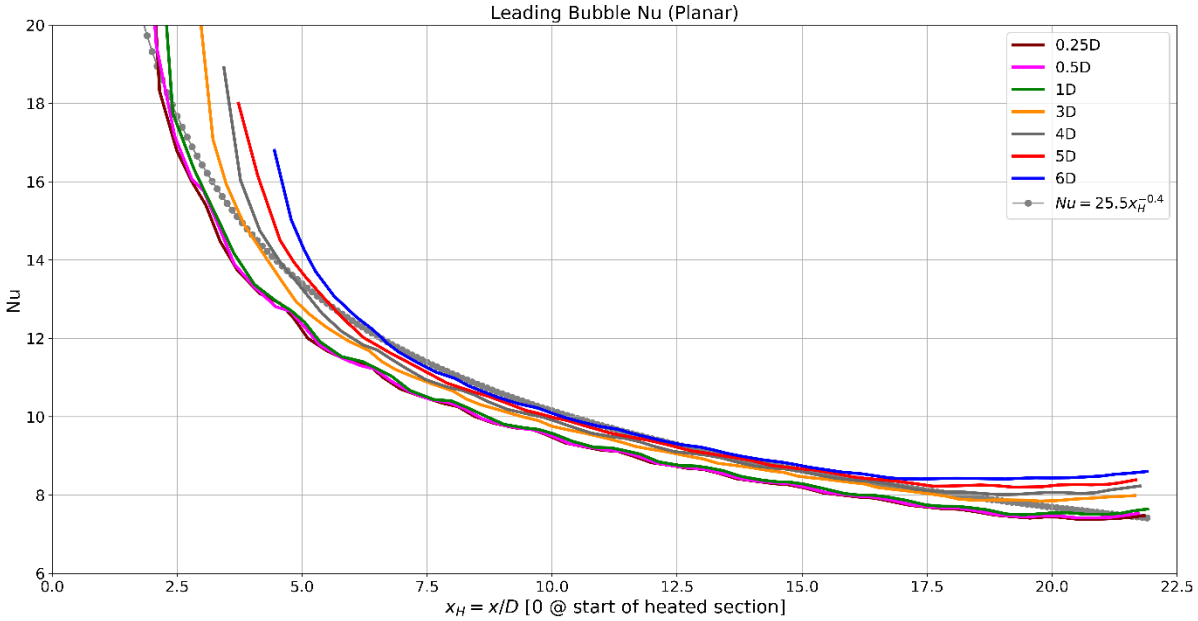

Figure 4-11: Averaged Nusselt number (Nu) of the leading bubble versus the position of the bubble midpoint for planar cases.

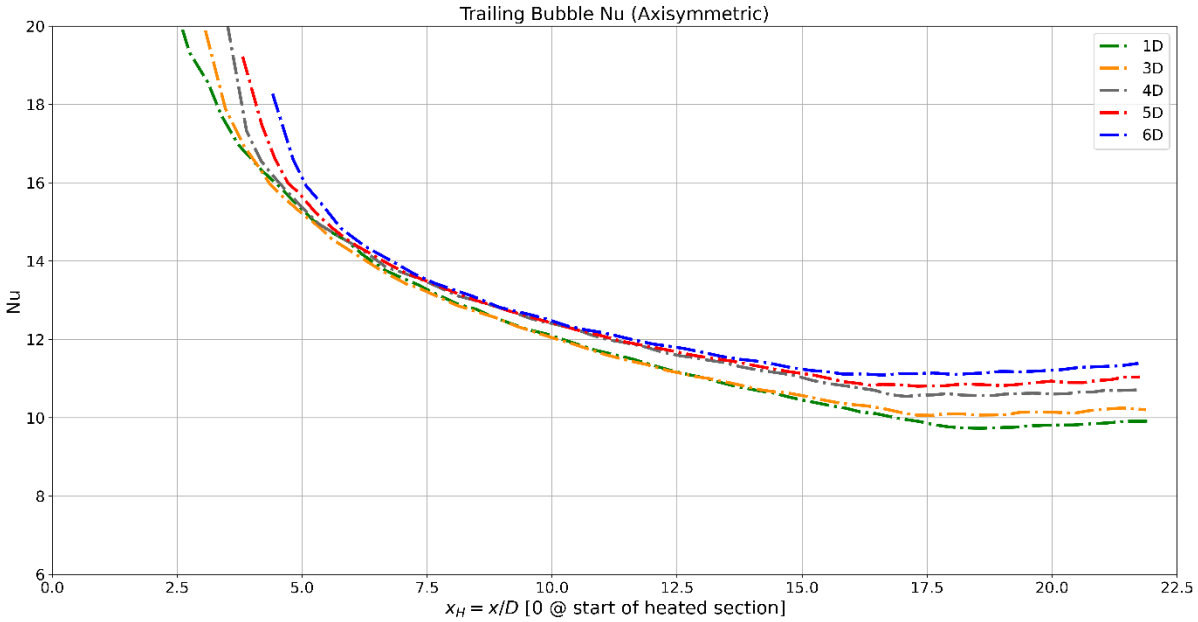

Figure 4-12: Averaged Nusselt number (Nu) of the trailing bubble versus the position of the bubble midpoint for axisymmetric cases.

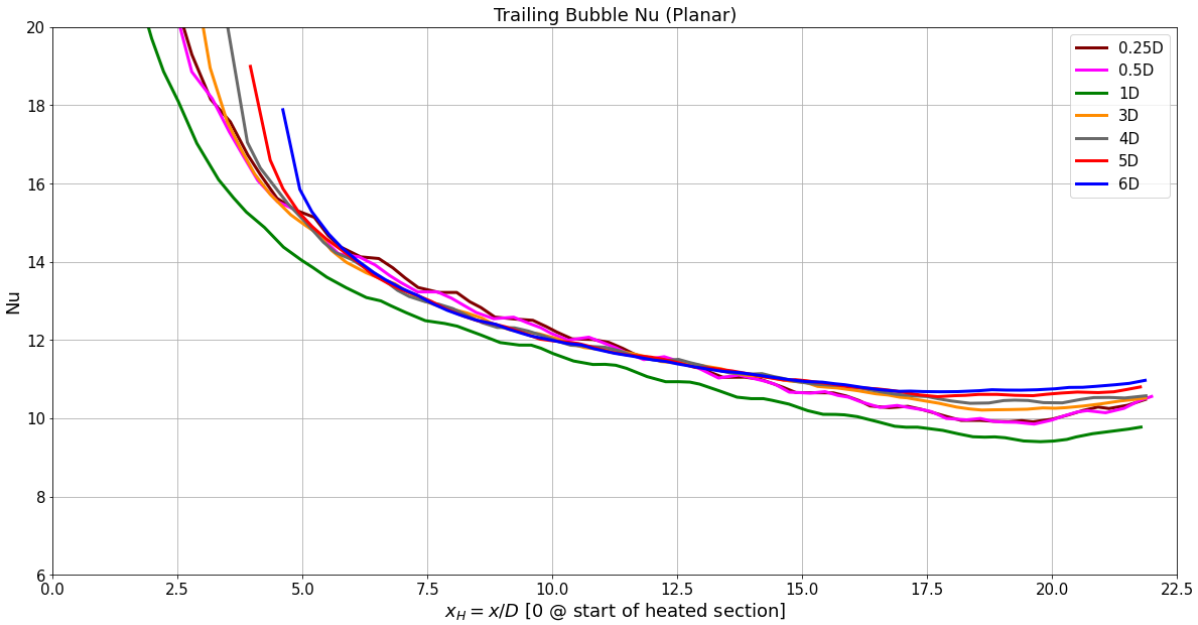

Figure 4-13: Averaged Nusselt number (Nu) of the trailing bubble versus the position of the bubble midpoint for planar cases.

The final metric under investigation was the change in volume of the vapour phase with respect to time. The volume was normalised by dividing it by the initial vapour volume, V_{int}. These graphs (Figure 4-14a and Figure 4-15) followed the same trends as the length versus time graphs (Figure 4-2, Figure 4-3, Figure 4-5 and Figure 4-6); as time progressed, the volume increased. This proved that phase change was present and that the bubbles were not only deforming. Figure 4-14b illustrates the volume change of the bubbles over time for L_{int} = 3D; these time frames correspond to the marked points in Figure 4-14a.

The average gradients were calculated on the interval τ = 20-30, and the values are listed in Table 4-2. During this interval, both bubbles were located inside the heated section, and the gradients could

be described as linear. This corresponds to equation 3.10, which is the linear relation between temperature and mass transfer. There was a small decrease present for the planar cases as L_{int} was increased. This corresponds to Figure 4-15 and proved that decreasing L_{int} improved the heat transfer of the systems, and more phase change occurred. The axisymmetric cases showed the same trend. However, L_{int} = 3D was significantly larger than for the other cases. This behaviour is also indicated in Figure 4-2a, where it shows the fastest growth rate of the leading bubbles. The growth rate of the trailing bubble is similar to the L_{int} = 1D case, shown in Figure 4-3. The cause of this behaviour is not clear and might be the result of the vapour to liquid length ratio in the axisymmetric domain, but further investigation is required to confirm this hypothesis.

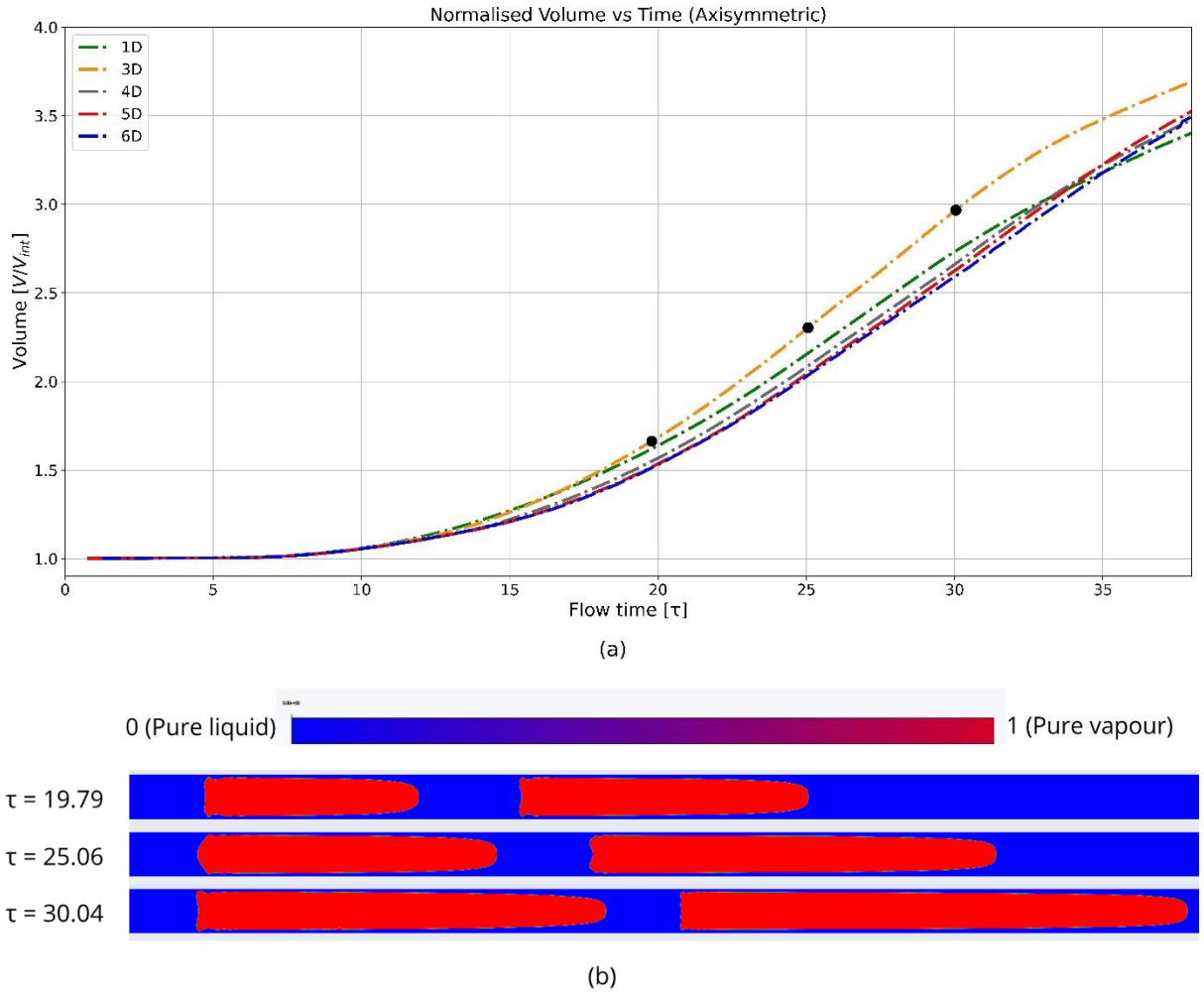

Figure 4-14: (a) Normalised vapour volume versus time for axisymmetric cases and (b) time frames illustrating volume change over time, corresponding to marked points in (a).

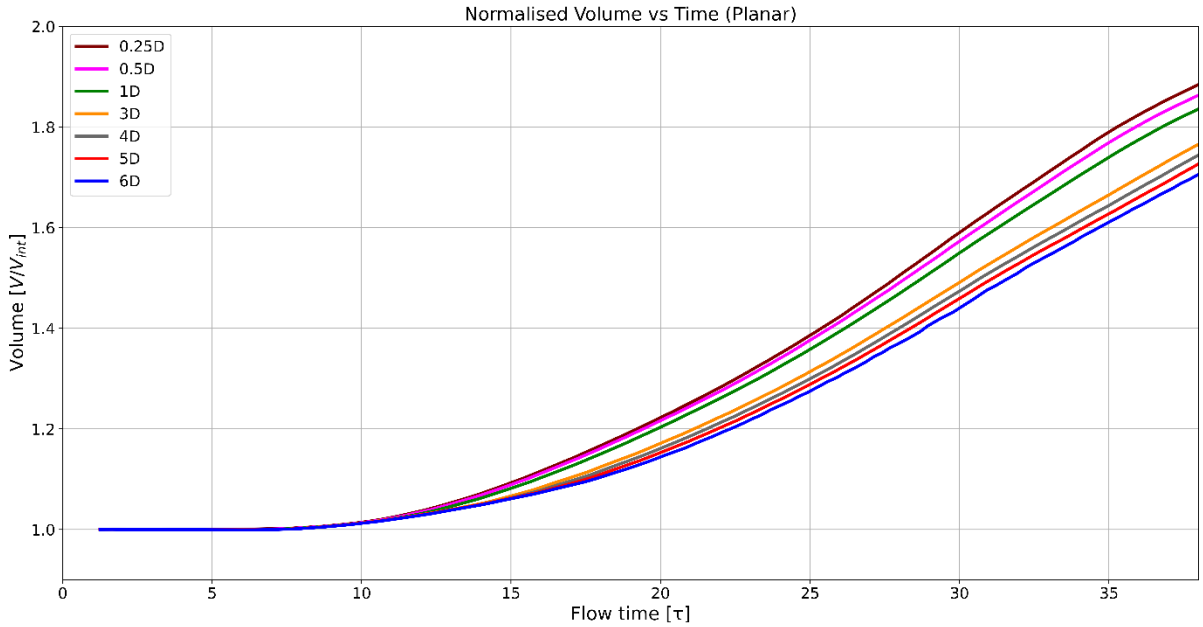

Figure 4-15: Normalised vapour volume versus time for planar cases.

Table 4-2: Average gradient of normalised volume for τ = 20-30 for two-bubble cases.

Initial spacing (L_{int})	Volume gradient for axisymmetric cases	Volume gradient for planar cases
0.25D		0.037
0.5D		0.036
1D	0.110	0.035
3D	0.128	0.032
4D	0.109	0.031
5D	0.109	0.031
6D	0.106	0.030

4.3.2 Three-bubble cases

Only the four smaller spacings were used for the cases with three bubbles present, i.e. L_{int} = 0.25D, 0.5D, 1D and 3D. The development of the leading bubbles was more varied (Figure 4-16) compared with that of the two-bubble cases (Figure 4-5). The case of L_{int} = 3D performed similarly, while the shorter spacings had a reduced final length. This correlates to the time the bubbles spent in the heated section. The cases for L_{int} = 0.25D and 0.5D took 30 ms to pass through the heated section, in comparison, L_{int} = 1D and L_{int} = 3D took 31 ms and 31.5 ms to pass through respectively. This difference in time could result from the incompressibility of the liquid and the presence of the additional bubble.

The middle bubble had a more uniform behaviour across the various initial spacings (Figure 4-17), where all the cases reached a final length of about 5 to 5.5D. This uniform development could result from the middle bubble being confined by the other bubbles, preventing expansion either forwards or backwards.

Of the three bubbles present in the domain, the trailing bubble experienced the greatest variation between the cases (Figure 4-18). There is a significant difference between all the cases, where L_{int} = 0.25D showed the most development with a final length of 6.5D and L_{int} = 3D showed the least development at a final length of 4.25D. This suggests that the trailing bubble benefited from both the

previous bubbles disrupting the thermal boundary layer. The longer the leading bubble, the shorter the trailing bubble and vice versa. As the trailing bubble grew, it pushed the other forward. This had a greater influence on the cases with a shorter L_{int}, resulting in a higher velocity of the leading bubbles and less time to absorb heat and grow. The closer the bubbles were together, the greater the benefit for the trailing bubble as the thermal boundary layer had less time to recover.

The middle and trailing bubbles for L_{int} = 3D mimicked the behaviour seen in the two-bubble scenario while the bubbles were in the entrance region. As the bubble shape developed in the absence of phase change, it expanded slightly and remained constant until phase change occurred. The middle bubbles for L_{int} = 0.25D and L_{int} = 3D are illustrated in Figure 4-19 at τ = 7.9, and the trailing bubbles at τ = 11.9 are shown in Figure 4-20. Both bubbles for L_{int} = 3D had a sharper and slimmer shape compared with the shape of their counterparts, replicating the behaviour of the two-bubble scenario.

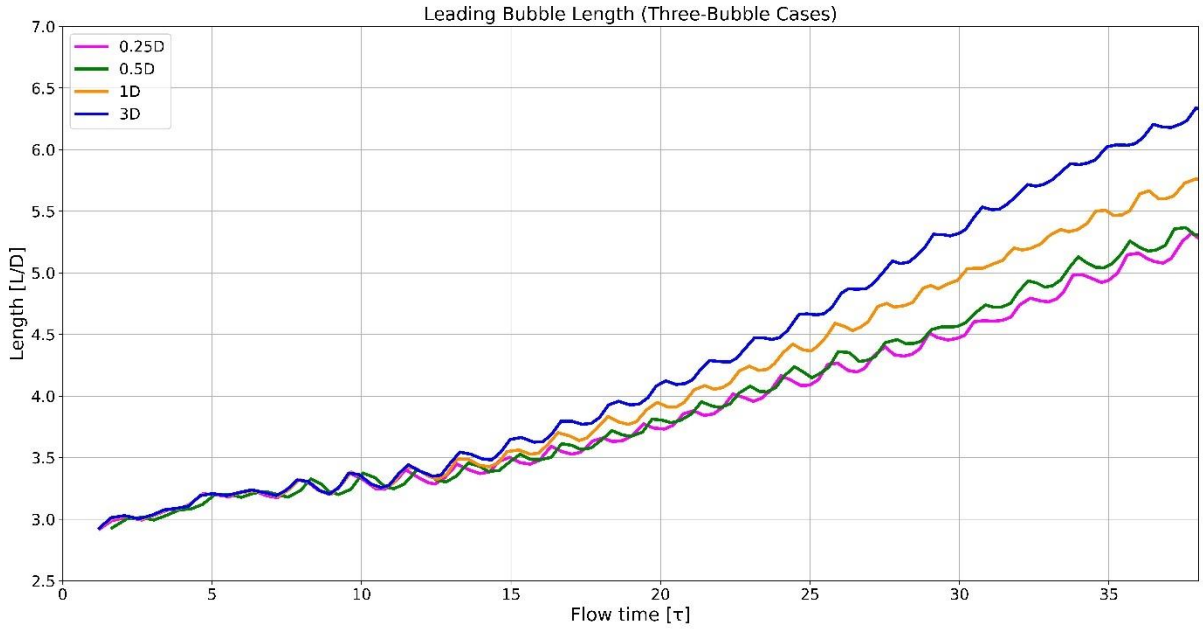

Figure 4-16: Leading bubble length versus time (three-bubble cases).

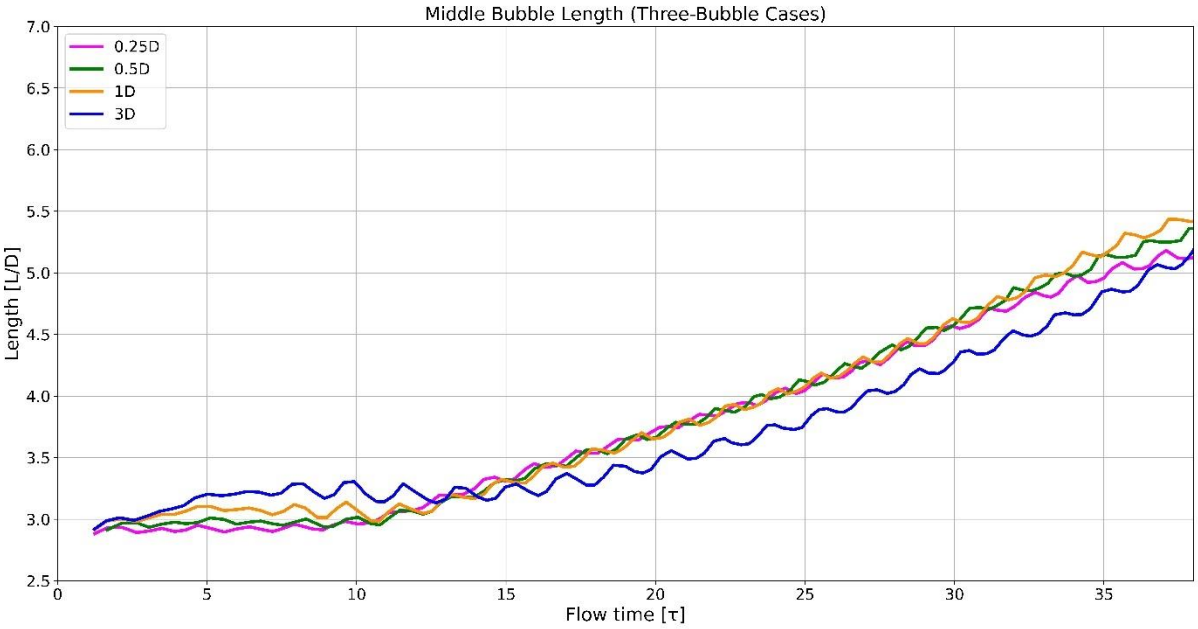

Figure 4-17: Middle bubble length versus time (three-bubble cases).

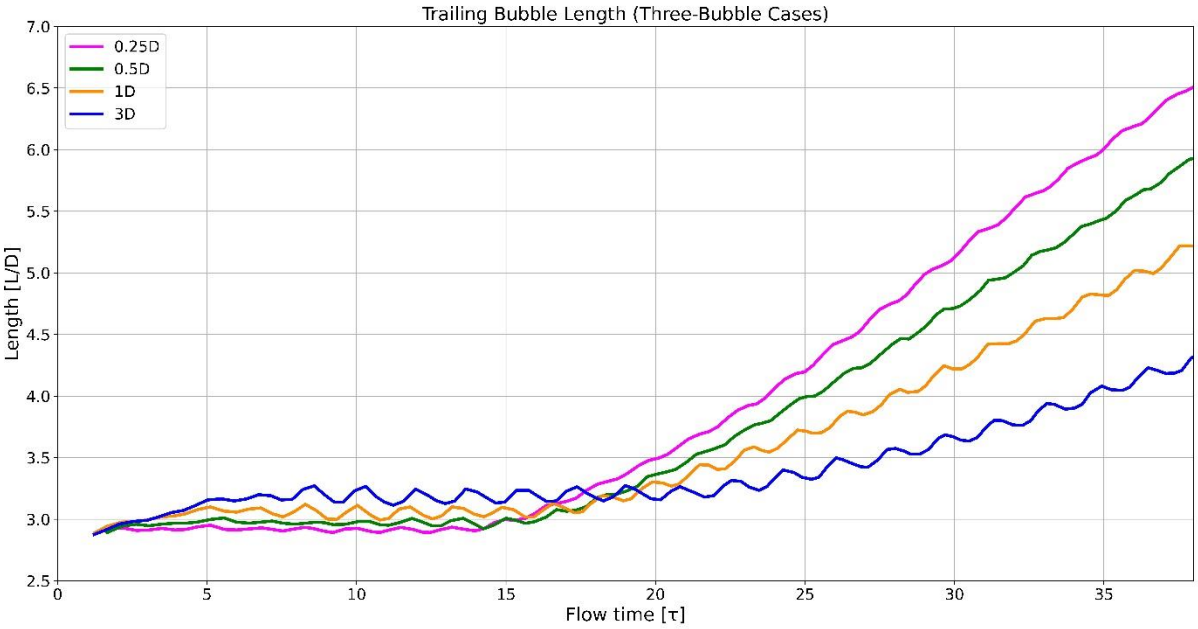

Figure 4-18: Trailing bubble length versus time (three-bubble cases).

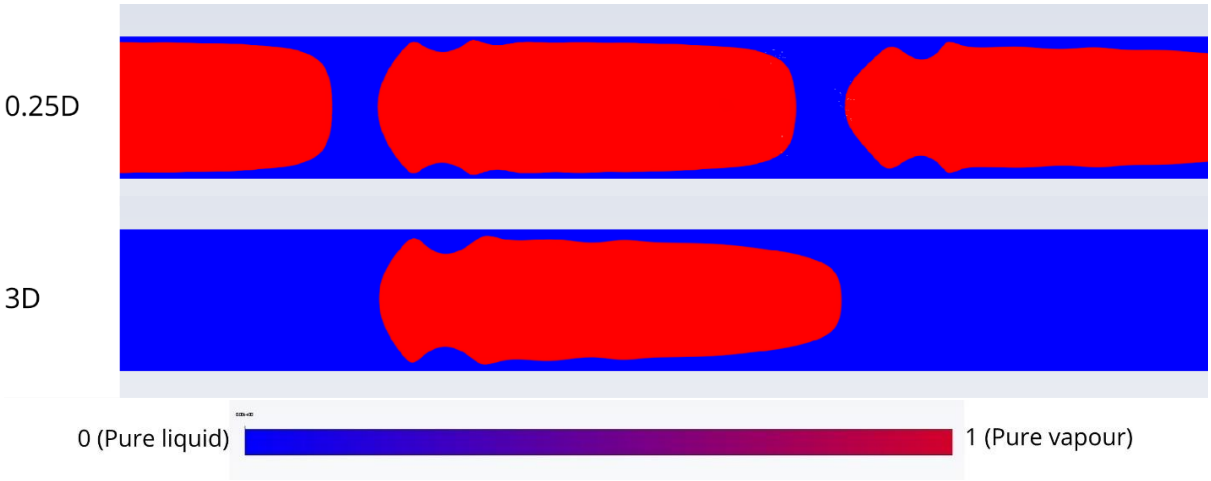

Figure 4-19: Middle bubbles for L_{int} = 0.25D and L_{int} = 3D at τ = 7.9.

Figure 4-20: Trailing bubbles for L_{int} = 0.25D and L_{int} = 3D at τ = 11.9.

The distance between the bubbles showed no significant change between the first and second bubbles (Figure 4-21) and the second and third (Figure 4-22). The case of L_{int} = 3D had a small decrease for both distances as the bubbles developed, while the other cases slightly increased. The behaviour seen here is a replication of the two-bubble cases (Figure 4-9).

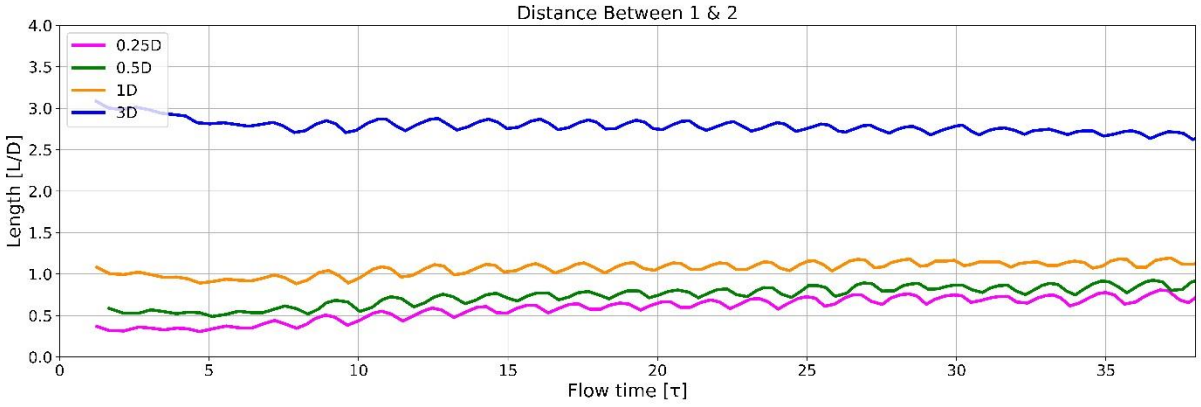

Figure 4-21: Distance between first and second bubble versus time.

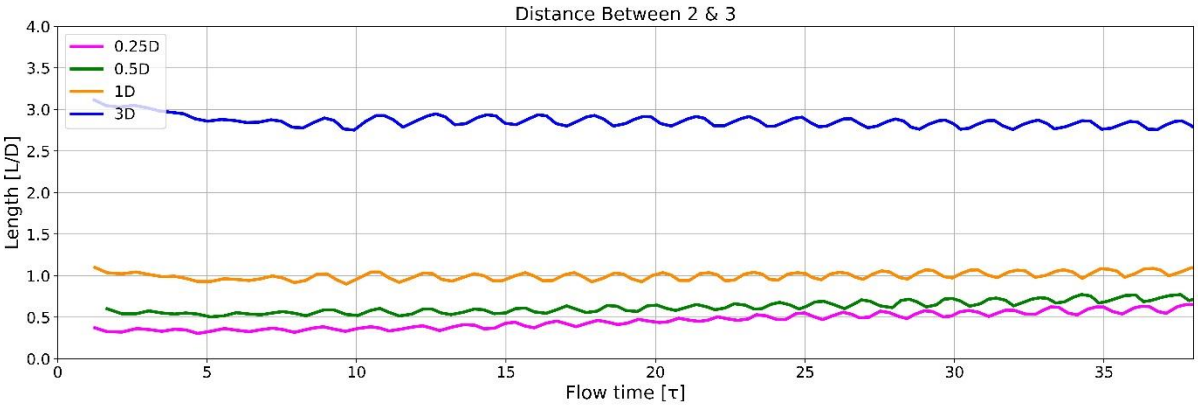

Figure 4-22: Distance between second and third bubble versus time.

The leading bubbles had an almost identical Nu (Figure 4-23), as seen in the two-bubble scenario (Figure 4-10 and Figure 4-11). The Nu produced also showed a good fit with the correlation given by equation 4.1. The cases performed similarly to the two-bubble scenario and reached a final value below 8. In Figure 4-24, the overall Nu increased for all the cases. The middle bubbles also showed an increase of roughly 25%, similar to the two-bubble scenario. The increase was due to the disturbed thermal boundary layer caused by the leading bubble. There was no significant difference between the cases for the first half of the heated section. Towards the end of the section, the values started to differ, and the final results varied from just below 9 to 10. The values were still relatively close together, which could be due to the other bubbles confining the middle bubble. A similar trend is observed with the length development of the middle bubble (Figure 4-17).

Figure 4-25 shows a significant difference for the intermediate values of the Nu for the different cases. The case for L_{int} = 0.25D produced the highest intermediate Nu increasing by 36.5% of the interval x_H = 5 – 10, while L_{int} = 3D had the lowest intermediate value, only increasing by 8.2% over the same interval. This shows that the spacing between bubbles directly influenced the system's heat transfer capabilities, with smaller spacings being more advantageous. As the spacing between bubbles changed, the recovery time of the thermal boundary layer changed resulting in a different Nu. The final values for the different cases were still similar at around 12. This is a 50% increase over the leading bubble and a 20% over the middle bubble. It was expected that the difference between sequential bubbles would decrease as more bubbles passed through the section and a steady state was reached.

The graph shows an increase of the Nu of L_{int} = 0.25D, 0.5D and 1D towards the end of the heated section. The highest Nu occurred at the rear of the bubble, where the film thickness was thinnest. Therefore, as the bubble left the heated section, the average Nu along the length of the bubble increased due to a reduced number of data points.

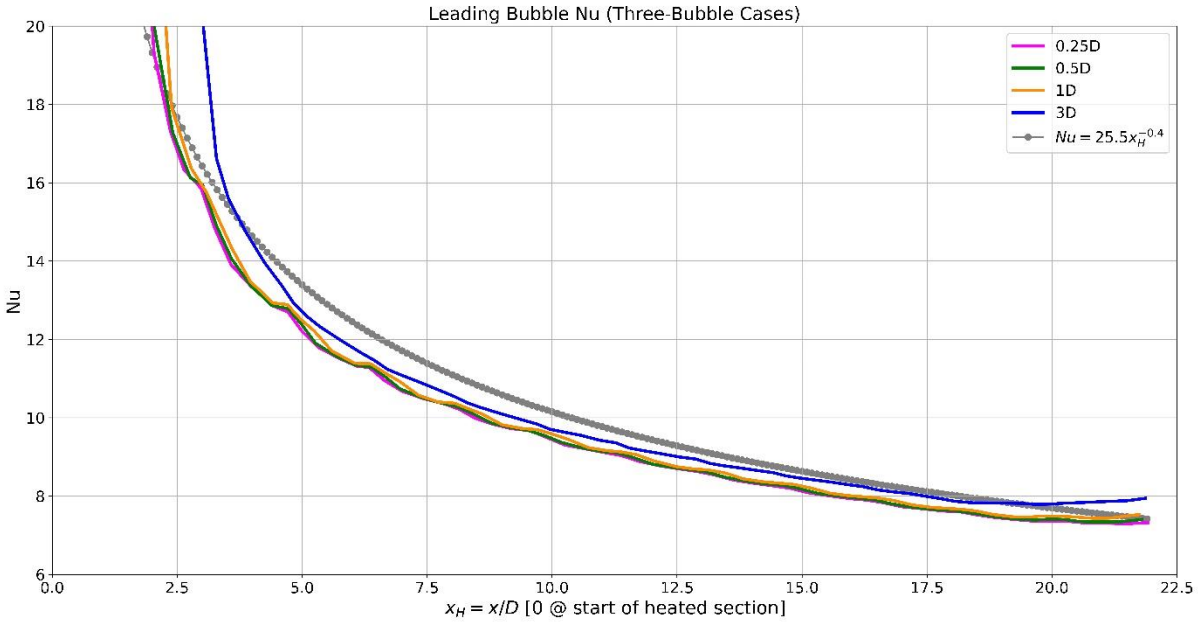

Figure 4-23: Averaged Nusselt number (Nu) of leading bubble versus bubble midpoint (three-bubble cases).

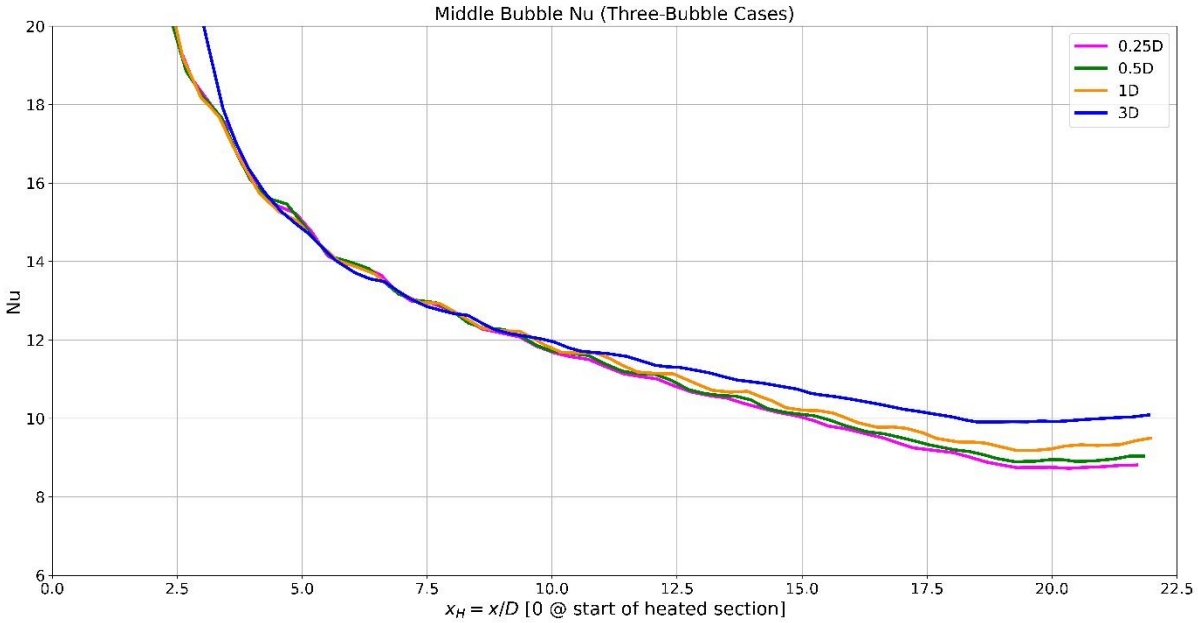

Figure 4-24: Averaged Nusselt number (Nu) of middle bubble versus bubble midpoint (three-bubble cases).

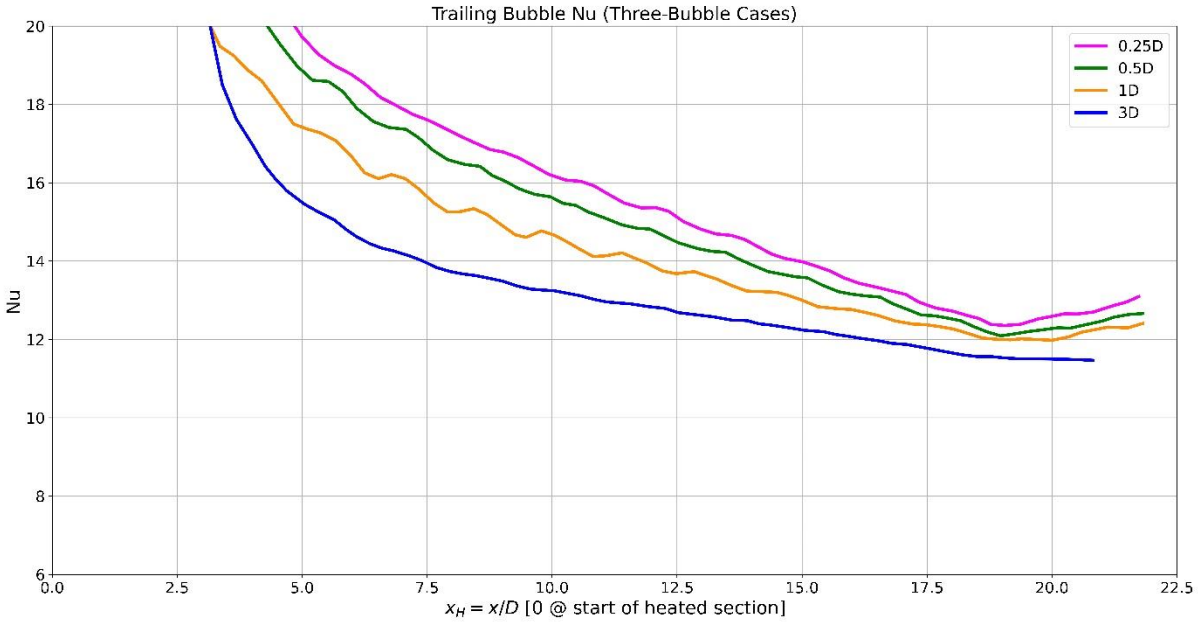

Figure 4-25: Averaged Nusselt number (Nu) of trailing bubble versus bubble midpoint (three-bubble cases).

The normalised volume for the three-bubble cases in Figure 4-26 showed a steady increase for all the cases and a significant difference between the cases. The smaller the initial spacing, the greater the volume change. Table 4-3 lists the average gradient over the interval τ = 20-30. These gradients also suggest that decreasing the distance between bubbles improved the heat transfer and increased the volume change rate due to increased mass transfer. This corresponds to the results of the planar domain in the two-bubble scenario. The rate of change was also linear when all the bubbles were located in the heated section.

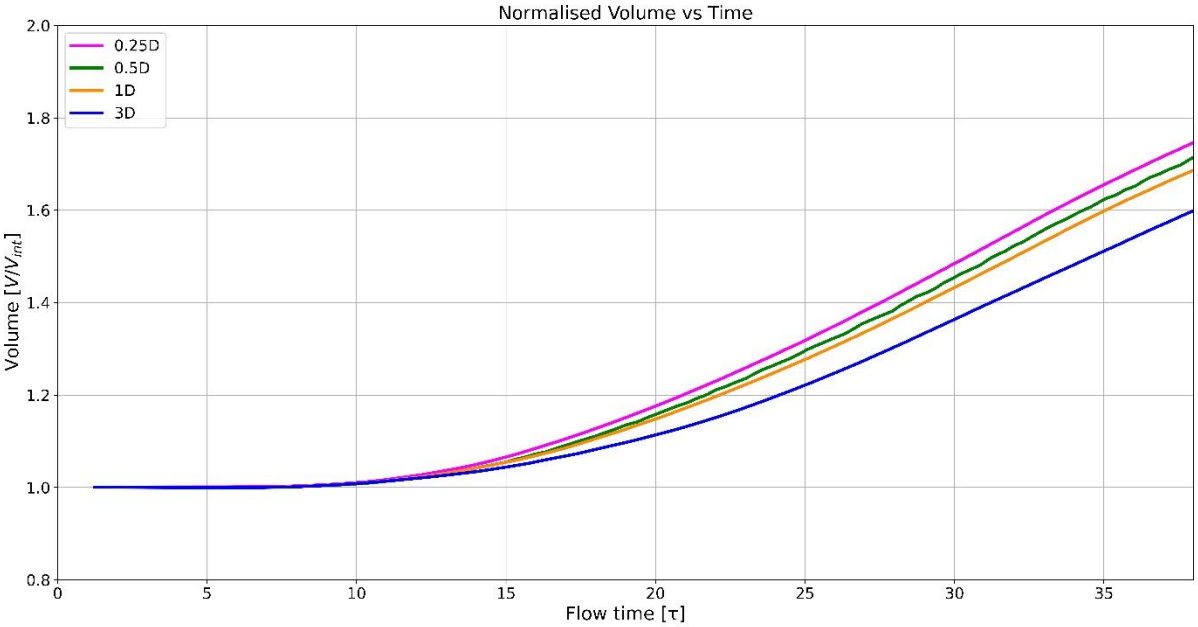

Figure 4-26: Normalised vapour volume versus time (three-bubble cases).

Table 4-3: Average gradient of normalised volume for τ = 20-30 for three-bubble cases.

Initial spacing (L_{int})	Volume gradient for three-bubble cases
0.25D	0.0309
0.5D	0.0305
1D	0.0285
3D	0.0252

To ensure that the mass transfer model did not force phase change, L_{int} = 0.25D was recreated with a zero-heat flux applied. Figure 4-27 shows that the normalised vapour volume remained constant throughout the simulation. Additionally, the velocity of the noses and tails of the bubbles in these two cases are compared. The velocities were calculated from the change in position over time. The largest difference was present for the nose of the leading bubbles. The velocity where heat flux was applied was 30% higher than for the case without heat flux. This decreased towards the tail of the final bubble, where the difference was less than 4%, illustrating that evaporation accelerated the flow and that the bubbles grew in the direction of flow.

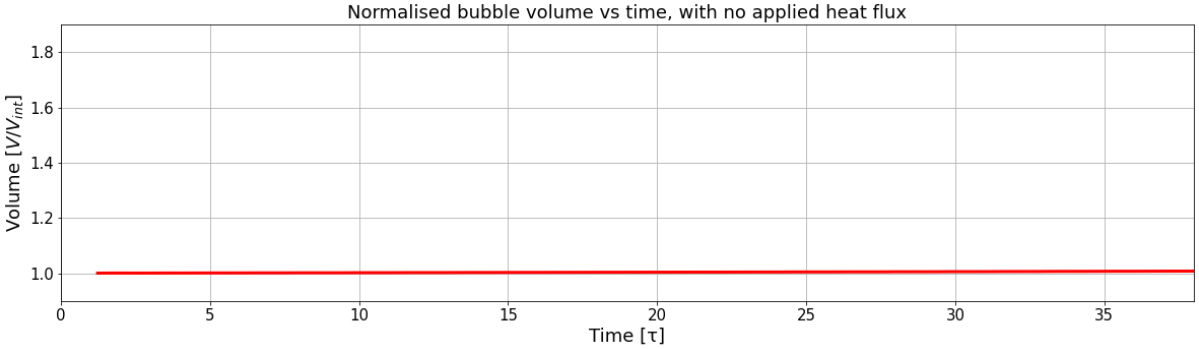

Figure 4-27: Normalised vapour volume versus time for zero-heat flux case.

4.4 Three-dimensional results

The case with L_{int} = 3D was selected for the three-dimensional investigation into the effect of different gravitational orientations. The channel had a height of 0.5mm and a width of 5mm for an aspect ratio of 10. The aim was to investigate four different cases: a top- and bottom-heated case to compare with the two-dimensional results and a single-side heated case rotated around the x-axis to three different positions. The figure on the left in Figure 4-28 illustrates the top- and bottom-heated case, and the two on the right the rotated domain for bottom-heated and side-heated.

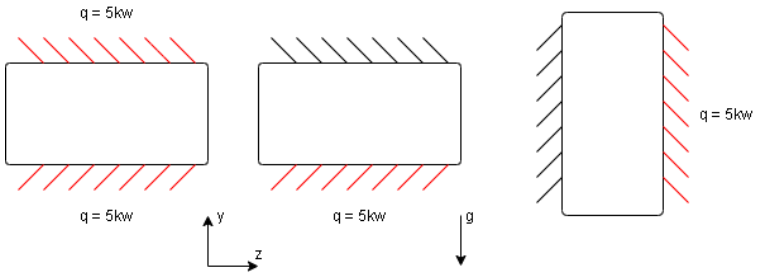

Figure 4-28: Heat fluxes applied to the three-dimensional cases, viewed down the channel in the flow direction.

Unfortunately, these simulations have not yet finished. After more than 8 weeks and using 216-240 parallel core, the simulation has only reached 5.2 ms of physical time. It should be stated that these

simulations have not been conducted as a continuous run but rather as a series of short submissions to a computer cluster with a 48-hour run-time limit. Due to these limitations and other factors that influenced the availability of the cluster, this simulation took more than six months to reach this state.

No data of significant value has been produced, because the leading bubble has only started to enter the heated section. The dashed black line in Figure 4-29 indicates the entrance of the heated section; the three-dimensional and two-dimensional cases are represented by the solid and dashed lines respectively. The small dataset that is available does show a good comparison with the two-dimensional case.

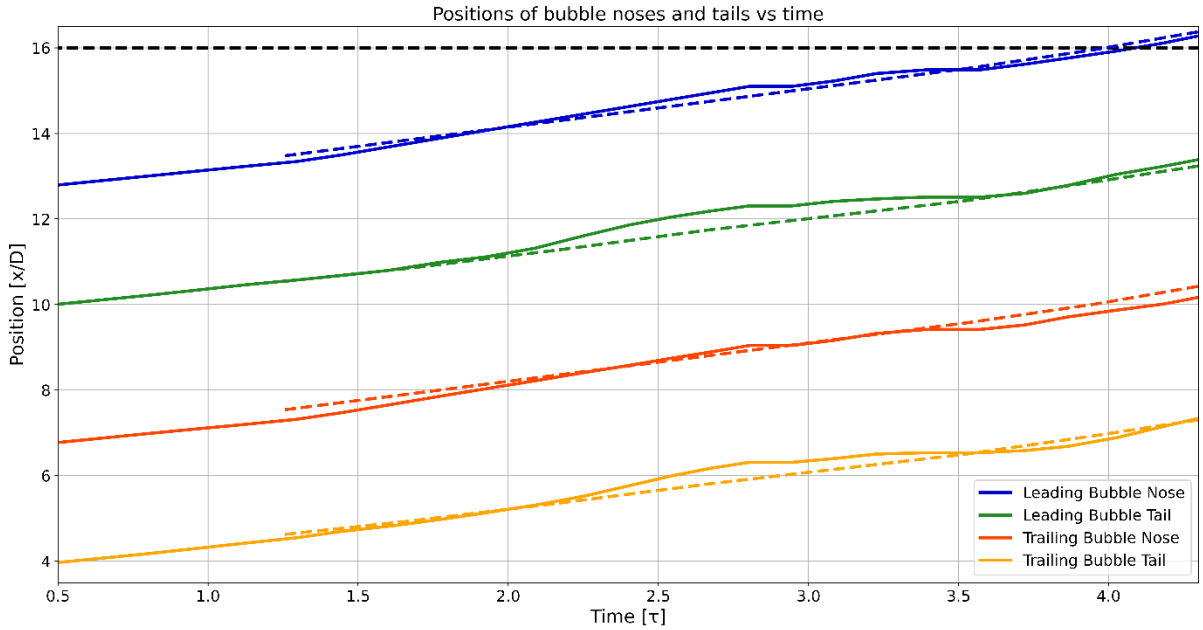

Figure 4-29: Comparing the position of bubble noses and tails versus time of the three-dimensional case (solid line) with the two-dimensional case (dashed line). The dashed black line indicates the start of the heated section.

4.5 Conclusion

The influence of the spacing between bubbles was numerically investigated in a two-dimensional domain. The results showed that a shorter spacing improved the heat transfer of the sequential bubbles, resulting in more phase change. The two-bubble case with an initial spacing of 6D saw a change in volume of 70% and the case of 0.25D increased by 88%. The three-bubble case had a difference of 15% in final volume between the largest and smallest initial spacings. The sequential bubbles benefited more from the disturbed thermal boundary layer with a shorter spacing, improving the heat transfer. The leading bubbles perform similar to each other as they all enter a heated section which is at a steady-state.

A three-dimensional analysis was attempted, but the simulations have not yet finished. The preliminary results show a good correlation to the two-dimensional results. However, no data have been available on the heat transfer yet. The high aspect ratio of the domain containing two bubbles was ambitious regarding the time frame. A single bubble investigation would have been possible. Since the liquid-vapour interface accounted for most of the mesh elements, multiple bubbles drastically increased the number of elements, and the interface only became larger as the bubbles developed, increasing the calculation time of the iterations as the simulation progressed.

5. Conclusion

In this study, various numerical simulations were conducted to investigate the influence of the liquid slug length between bubbles on the heat transfer and phase change during microchannel slug flow. First, a literature review was conducted, investigating heat transfer, flow boiling, previous studies and possible applications.

In the next chapter, the numerical methodology was discussed. The governing equations of the system and the solution procedure were described. The models used for mass transfer and mesh adaption were reviewed. The last section of the chapter presented a comparison of the results with the results of a previous study and found that the chosen models and methods produced accurate results.

Simulations in two-dimensional and three-dimensional domains were conducted in Ansys Fluent 19.4. The VOF method was used to simulate two-phase flow. The dimensions were 0.5 mm x 36 mm for the two-dimensional domain and 0.5 x 5 x 19 mm for the three-dimensional domain. The three-dimensional domain had a rectangular cross-section with rounded corners. The working fluid in all the simulations was refrigerant R245fa. The bubbles were patched into an adiabatic entrance region to allow the bubble to develop before heat transfer was present. The entrance region allowed adjustment of the initial distance between the bubbles independently of other flow parameters. The mass flux at the entrance was 550 kg/m^2.s, and the applied heat flux was set to 5 kW/m^2. The simulation time of the two-dimensional cases was 50 ms. Axisymmetric and planar domains were used to investigate the interaction between multiple bubbles in the slug flow regime and the effects on heat transfer. Adaptive meshing was used to conduct these simulations with reduced computational costs.

The following conclusions were drawn:

- The thermally disturbed region was longer than the spacing between the bubbles for all the cases investigated, resulting in the sequential bubbles having higher heat transfer coefficients. The Nu was found to increase by 25% from the leading bubble to the following bubble in all the cases. A further increase of 20% was observed between the second and third bubbles.
- As the initial spacing was reduced, the heat transfer was enhanced for the trailing bubbles. This was due to a shorter recovery time available to the thermal boundary layer before the next bubble passed.
- More phase change occurred when the bubbles were closer together.
- When more than two bubbles were present in the domain, the bubbles in the middle were confined, and their growth was limited.
- Simulating multiple bubbles provided a more accurate representation of reality than with single-bubble simulations.
- The three-dimensional simulations could not be conducted in the time frame of the study, and the effects of gravitational orientation on multibubble slug flow could not be investigated.

The results of this study provide insight into aspects of slug flow that are difficult to observe experimentally. The results also show a good comparison with the work of Magnini et al. (2013a) and Magnini & Thome (2016).

6. Recommendations

The numerical simulations conducted in this study were idealised cases to investigate the effect of the distance between bubbles. Recommendations for further work are as follows:

- The mesh adaption used in this study made it possible to conduct a three-dimensional simulation. However, the high aspect ratio was ambitious as the simulations are still running. The domain currently consists of $32x10^6$ cells and will increase as the bubbles grow and develop. The number of bubbles influences the number of elements because the total refined region increases with a total increased interface area. To improve simulation time, it is recommended to decrease the aspect ratio of the microchannel. For example, reducing the aspect ratio from 1:10 to 1:5 can drastically reduce the number of elements and improve simulation time.
- This study can be improved by adding more bubbles to the domain. Investigating four or five bubbles present in the domain will provide better insight into how the bubbles in the middle develop and influence the heat transfer characteristics. This will also be a closer representation of reality.
- Employing adaptive meshing can allow researchers to investigate longer channels and longer flow time in two-dimensional. This can provide valuable information into the converging nature of time-averaged Nu, bubble growth and bubble coalescence.

References

Abdollahi, A., Sharma, R. N. & Vatani, A. 2017. Fluid flow and heat transfer of liquid-liquid two phase flow in microchannels: A review. *International Communications in Heat and Mass Transfer,* 84**,** 66-74.

Agostini, B., Bontemps, A. & Thonon, B. 2006. Effects of Geometrical and Thermophysical Parameters on Heat Transfer Measurements in Small-Diameter Channels. *Heat Transfer Engineering,* 27**,** 14-24.

ASME 2009. *Standard for Verification and Validation in Computational Fluid Dynamics and Heat Transfer: An American National Standard*, American Society of Mechanical Engineers.

Asthana, A., Zinovik, I., Weinmueller, C. & Poulikakos, D. 2011. Significant Nusselt number increase in microchannels with a segmented flow of two immiscible liquids: An experimental study. *International Journal of Heat and Mass Transfer,* 54**,** 1456-1464.

Bach, M. 2014. *Impact of Temperature on Intel CPU Performance* [Online]. Available: https://www.pugetsystems.com/labs/articles/Impact-of-Temperature-on-Intel-CPU-Performance-606/.

Barber, J., Sefiane, K., Brutin, D. & Tadrist, L. 2009. Hydrodynamics and heat transfer during flow boiling instabilities in a single microchannel. *Applied Thermal Engineering,* 29**,** 1299-1308.

Bayareh, M., Nasr Esfahany, M., Afshar, N. & Bastegani, M. 2020. Numerical study of slug flow heat transfer in microchannels. *International Journal of Thermal Sciences,* 147**,** 106118.

Betz, A. R. & Attinger, D. 2010. Can segmented flow enhance heat transfer in microchannel heat sinks? *International Journal of Heat and Mass Transfer,* 53**,** 3683-3691.

Bogojevic, D., Sefiane, K., Walton, A., Lin, H. & Cummins, G. 2009. Two-phase flow instabilities in a silicon microchannels heat sink. *International Journal of Heat and Fluid Flow,* 30**,** 854-867.

Bonometti, T. & Magnaudet, J. 2007. An interface-capturing method for incompressible two-phase flows. Validation and application to bubble dynamics. *International Journal of Multiphase Flow,* 33**,** 109-133.

Bordbar, A., Taassob, A., Zarnaghsh, A. & Kamali, R. 2018. Slug flow in microchannels: Numerical simulation and applications. *Journal of industrial and engineering chemistry,* 62**,** 26-39.

Brackbill, J. U., Kothe, D. B. & Zemach, C. 1992. A continuum method for modeling surface tension. *Journal of Computational Physics,* 100**,** 335-354.

Bretherton, F. P. 1961. The motion of long bubbles in tubes. *Journal of Fluid Mechanics,* 10**,** 166-188.

Carlson, A. 2007. *Numerical Simulations Of Slug Flow In A Micro Channel.* Master thesis, The Norwegian University of Science and Technology.

Çengel, Y. A. & Ghajar, A. J. 2015. *Heat and Mass Transfer: Fundamentals & Applications,* Fifth edition., New York, NY, McGraw Hill Education.

Che, Z., Wong, T. N. & Nguyen, N.-T. 2012. Heat transfer enhancement by recirculating flow within liquid plugs in microchannels. *International Journal of Heat and Mass Transfer,* 55**,** 1947-1956.

Che, Z., Wong, T. N. & Nguyen, N.-T. 2013. Heat transfer in plug flow in cylindrical microcapillaries with constant surface heat flux. *International Journal of Thermal Sciences,* 64**,** 204-212.

Chinnov, E., Ronshin, F. & Kabov, O. 2015. Features of two-phase flow in a rectangular microchannel with the height of 300 µm. *Thermophysics and Aeromechanics,* 21**,** 759-762.

Courant, R., Friedrichs, K. & Lewy, H. 1967. On the partial difference equations of mathematical physics. *IBM journal of Research and Development,* 11**,** 215-234.

Ferrari, A., Magnini, M. & Thome, J. R. 2018. Numerical analysis of slug flow boiling in square microchannels. *International Journal of Heat and Mass Transfer,* 123**,** 928-944.

Ferziger, J. H. & Perić, M. 2002. *Computational methods for fluid dynamics,* 3rd edition, Berlin, Springer.

Fondelli, T., Andreini, A. & Facchini, B. 2015. Numerical Simulation of Dam-Break Problem Using an Adaptive Meshing Approach. *Energy Procedia,* 82**,** 309-315.

Guo, Z., Fletcher, D. F. & Haynes, B. S. 2016. Numerical simulation of annular flow hydrodynamics in microchannels. *Computers & Fluids,* 133**,** 90-102.

Gupta, R., Fletcher, D. F. & Haynes, B. S. 2009. On the CFD modelling of Taylor flow in microchannels. *Chemical Engineering Science,* 64**,** 2941-2950.

Gupta, R., Fletcher, D. F. & Haynes, B. S. 2010. CFD modelling of flow and heat transfer in the Taylor flow regime. *Chemical Engineering Science,* 65**,** 2094-2107.

Han, Y. & Shikazono, N. 2009. Measurement of the liquid film thickness in micro tube slug flow. *International Journal of Heat and Fluid Flow,* 30**,** 842-853.

Hardt, S. & Wondra, F. 2008. Evaporation model for interfacial flows based on a continuum-field representation of the source terms. *Journal of Computational Physics,* 227**,** 5871-5895.

Husain, A. & Kwang-Yong, K. 2008. Shape Optimization of Micro-Channel Heat Sink for Micro-Electronic Cooling. *IEEE Transactions on Components and Packaging Technologies,* 31**,** 322-330.

Jafari, R. & Okutucu-Özyurt, T. 2016. 3D numerical modeling of boiling in a microchannel by arbitrary Lagrangian–Eulerian (ALE) method. *Applied Mathematics and Computation,* 272**,** 593-603.

Kandlikar, S., Garimella, S., Li, D., Colin, S. & King, M. R. 2005. *Heat transfer and fluid flow in minichannels and microchannels,* Amsterdam, Elsevier.

Kandlikar, S. G. 2002. Fundamental issues related to flow boiling in minichannels and microchannels. *Experimental Thermal and Fluid Science,* 26**,** 389-407.

Kew, P. A. & Cornwell, K. 1997. Correlations for the prediction of boiling heat transfer in small-diameter channels. *Applied Thermal Engineering,* 17**,** 705-715.

Kharangate, C. R. & Mudawar, I. 2017. Review of computational studies on boiling and condensation. *International Journal of Heat and Mass Transfer,* 108**,** 1164-1196.

Khodaparast, S., Magnini, M., Borhani, N. & Thome, J. R. 2015. Dynamics of isolated confined air bubbles in liquid flows through circular microchannels: an experimental and numerical study. *Microfluidics and Nanofluidics,* 19**,** 209-234.

Kreutzer, M. T., Kapteijn, F., Moulijn, J. A. & Heiszwolf, J. J. 2005. Multiphase monolith reactors: Chemical reaction engineering of segmented flow in microchannels. *Chemical Engineering Science,* 60**,** 5895-5916.

Kumari, S., Kumar, N. & Gupta, R. 2019. Flow and heat transfer in slug flow in microchannels: Effect of bubble volume. *International Journal of Heat and Mass Transfer,* 129**,** 812-826.

Kunkelmann, C. 2011. *Numerical modeling and investigation of boiling phenomena.* Technische Universität.

Li, J.-M. & Wang, B.-X. 2003. Size effect on two-phase regime for condensation in micro/mini tubes. *Heat Transfer—Asian Research,* 32**,** 65-71.

Liu, D., Ling, X., Peng, H., Li, J. & Duan, L. 2020. Experimental and numerical analysis on heat transfer performance of slug flow in rectangular microchannel. *International Journal of Heat and Mass Transfer,* 147**,** 118963.

Liu, Q. & Palm, B. 2016. Numerical study of bubbles rising and merging during convective boiling in micro-channels. *Applied Thermal Engineering,* 99**,** 1141-1151.

Lockhart, R. & Martinelli, R. 1949. Proposed correlation of data for isothermal two-phase, two-component flow in pipes. *Chem. Eng. Prog,* 45**,** 39-48.

Ma, S., Sherwood, J. M., Huck, W. T. S. & Balabani, S. 2014. On the flow topology inside droplets moving in rectangular microchannels. *Lab on a Chip,* 14**,** 3611-3620.

Magnini, M., Pulvirenti, B. & Thome, J. 2013a. Numerical investigation of the influence of leading and sequential bubbles on slug flow boiling within a microchannel. *International Journal of Thermal Sciences,* 71**,** 36-52.

Magnini, M., Pulvirenti, B. & Thome, J. R. 2013b. Numerical investigation of hydrodynamics and heat transfer of elongated bubbles during flow boiling in a microchannel. *International Journal of Heat and Mass Transfer,* 59**,** 451-471.

Magnini, M. & Thome, J. 2016. A CFD study of the parameters influencing heat transfer in microchannel slug flow boiling. *International Journal of Thermal Sciences,* 110**,** 119-136.

Mehdizadeh, A., Sherif, S. A. & Lear, W. E. 2011. Numerical simulation of thermofluid characteristics of two-phase slug flow in microchannels. *International Journal of Heat and Mass Transfer,* 54**,** 3457-3465.

Mikaelian, D., Haut, B. & Scheid, B. 2015. Bubbly flow and gas–liquid mass transfer in square and circular microchannels for stress-free and rigid interfaces: dissolution model. *Microfluidics and Nanofluidics,* 19**,** 899-911.

Mohammed, H., Gunnasegaran, P. & Shuaib, N. 2011. Numerical simulation of heat transfer enhancement in wavy microchannel heat sink. *International Communications in Heat and Mass Transfer,* 38**,** 63-68.

Naphon, P. 2007. Laminar convective heat transfer and pressure drop in the corrugated channels. *International Communications in Heat and Mass Transfer,* 34**,** 62-71.

Nichita, B. A. & Thome, J. R. A level set method and a heat transfer model implemented into FLUENT for modeling of microscale two phase flows. AVT-178 Specialists' Meeting on System Level Thermal Management for Enhanced Platform Efficiency, 2010.

Ohadi, M., Choo, K., Dessiatoun, S. & Cetegen, E. 2013. Emerging Applications of Microchannels. In *Next Generation Microchannel Heat Exchangers.* New York: Springer.

Ong, C. L. & Thome, J. R. 2011. Macro-to-microchannel transition in two-phase flow: Part 1 - Two-phase flow patterns and film thickness measurements. *Experimental Thermal and Fluid Science,* 35**,** 37-47.

Ottino, J. M. & Wiggins, S. 2004. Introduction: mixing in microfluidics. *Philosophical Transactions of the Royal Society of London. Series A: Mathematical, Physical and Engineering Sciences,* 362**,** 923-935.

Potgieter, J. 2019. *Numerical investigation on the effect of gravitational orientation on bubble growth during flow boiling in a high aspect ratio microchannel.* Master thesis, University of Pretoria.

Revellin, R. 2005. *Experimental two-phase fluid flow in microchannels.* EPFL.

Ribatski, G., Wojtan, L. & Thome, J. R. 2006. An analysis of experimental data and prediction methods for two-phase frictional pressure drop and flow boiling heat transfer in micro-scale channels. *Experimental Thermal and Fluid Science,* 31**,** 1-19.

Sadeghi, E., Bahrami, M. & Djilali, N. 2010. Estimation of Nusselt Number in Microchannels of Arbitrary Cross Section with Constant Axial Heat Flux. *Heat Transfer Engineering,* 31**,** 666-674.

Sakanova, A., Keian, C. C. & Zhao, J. 2015. Performance improvements of microchannel heat sink using wavy channel and nanofluids. *International Journal of Heat and Mass Transfer,* 89**,** 59-74.

Schrage, R. W. 1953. *A Theoretical Study of Interphase Mass Transfer*, Columbia University Press.

Serizawa, A., Feng, Z. & Kawara, Z. 2002. Two-phase flow in microchannels. *Experimental Thermal and Fluid Science,* 26**,** 703-714.

Srinivasan, V. & Khandekar, S. 2017. Thermo-hydrodynamic transport phenomena in partially wetting liquid plugs moving inside micro-channels. *Sadhana - Academy Proceedings in Engineering Sciences,* 42**,** 607-624.

Sui, Y., Teo, C. J., Lee, P. S., Chew, Y. T. & Shu, C. 2010. Fluid flow and heat transfer in wavy microchannels. *International Journal of Heat and Mass Transfer,* 53**,** 2760-2772.

Sun, D.-L., Xu, J.-L. & Wang, L. 2012. Development of a vapor–liquid phase change model for volume-of-fluid method in FLUENT. *International Communications in Heat and Mass Transfer,* 39**,** 1101-1106.

Szczukiewicz, S., Borhani, N. & Thome, J. R. 2013. Two-phase heat transfer and high-speed visualization of refrigerant flows in 100 × 100 μm2 silicon multi-microchannels. *International Journal of Refrigeration,* 36**,** 402-413.

Szczukiewicz, S., Magnini, M. & Thome, J. R. 2014. Proposed models, ongoing experiments, and latest numerical simulations of microchannel two-phase flow boiling. *International journal of multiphase flow,* 59**,** 84-101.

Talimi, V., Muzychka, Y. S. & Kocabiyik, S. 2012. A review on numerical studies of slug flow hydrodynamics and heat transfer in microtubes and microchannels. *International Journal of Multiphase Flow,* 39**,** 88-104.

Tanasawa, I. 1991. Advances in Condensation Heat Transfer. In *Advances in Heat Transfer.* HARTNETT, J. P., IRVINE, T. F. & CHO, Y. I. (eds.). Tokyo: Elsevier.

Thome, J. R. 2004. Boiling in microchannels: a review of experiment and theory. *International Journal of Heat and Fluid Flow,* 25**,** 128-139.

Tuckerman, D. B. & Pease, R. F. W. 1981. High-performance heat sinking for VLSI. *IEEE Electron Device Letters,* 2**,** 126-129.

Vermaak, M., Potgieter, J., Dirker, J., Moghimi, M. A., Valluri, P., Sefiane, K. & Meyer, J. P. 2020. Experimental and numerical investigation of micro/mini channel flow-boiling heat transfer with non-uniform circumferential heat fluxes at different rotational orientations. *International Journal of Heat and Mass Transfer,* 158**,** 119948.

Wang, Y., Sefiane, K. & Harmand, S. 2012. Flow boiling in high-aspect ratio mini-and micro-channels with FC-72 and ethanol: experimental results and heat transfer correlation assessments. *Experimental Thermal and Fluid Science,* 36**,** 93-106.

Wojtan, L., Revellin, R., Thome, J. R. & Italia, H. B. L. I.-H. B. L. 2006. Investigation of saturated critical heat flux in a single, uniformly heated microchannel. *Experimental Thermal and Fluid Science,* 30**,** 765-774.

Zhao, Y., Chen, G. & Yuan, Q. 2006. Liquid-liquid two-phase flow patterns in a rectangular microchannel. *AIChE journal,* 52**,** 4052-4060.

Zhou, C. H. & Ai, J. Q. 2013. Mesh adaptation for simulation of unsteady flow with moving immersed boundaries. *International Journal for Numerical Methods in Fluids,* 72**,** 453-477.

Appendices

Appendix A: Mesh refinement and mass transfer UDF

```
/*(Hardt and Wondra, 2008) Evaporation Model.*/
#include "udf.h"
#include "prf.h"
#define domain_ID 2
static real NV=0.0;/*Vapour Normalisation Factor*/
static real NL=0.0;/*Liquid Normalisation Factor*/
static real mass_v=0;/*Vapour Creation per Cell*/
static real mass_l=0;/*Liquid Disappearance per Cell*/
static real enrg_s=0.0;/* Energy Change per Cell*/
static real T_SAT = 304.15;/*Saturation Temperature*/
static real ac= 1; /*Accomodation Coefficient*/
static real mgVOF=0.0; /*Magnitude of VOF Gradient*/
static real M=134; /*Molecular Mass*/
static real h=187300.0; /*Latent Heat*/
static real R=8314.0; /*Gas Constant*/
static real pi =3.1415259;/*pi*/
static real m_lg = 0.0;/*Mass Flux*/
static real m_nt=0.0;/*Temporal Gradient of Mass Flux*/
static real m_gr=0.0;/*Source term for Mesh Adaption*/
static real Ntop=0.0;/*Normalisation factor*/
static real Nbot=0.0;/*Normalisation factor denominator*/
static real Ntot=0.0;/*Normalisation factor numerator*/
static real RhoG=10.5;/*Vapour Density*/
static real RhoL=1322;/*Liquid Density*/
static real NVbot=0.0;/*Denomenator for Equation 17*/
static real NVLtop=0.0;/*Numerator for Equation 17 and Equation 18/
static real NLbot=0.0;/*Denomenator for Equation 18*/
static real VCutV=1e-3;/*Vapour volume cut-off*/
static real VCutL=1e-1;/*Liquid volume cut-off*/
static real cpl=1352; /*Liquid Specific Heat*/
static real cpg=926;/*Vapour Specific Heat*/
/*Scalars
uds-scalar-0: Volume Fraction
uds-scalar-1: Initial Mass Source Term Used for Smearing
uds-scalar-2: Smeared Mass Source Term
uds-scalar-3: Initial Mesh Source Term Used for Smearing
uds-scalar-4: Smeared Mesh Source Term
uds-scalar-5: Smeared and Bounded Mass Source Term
uds-scalar-6: Vapour Source Term
uds-scalar-7: Liquid Source Term
uds-scalar-8: Energy Source Term
uds-scalar-9: Gradient of Initial Source Term
*/
```

/*The purpose of the adjust_gradient function is to assign the volume fraction to a scalar quantity. Ansys Fluent does not automatically calculate the gradient of the volume fraction, but it does calculate it for scalar quantities, so this function forces Ansys Fluent to calculate the gradient of the volume fraction.*/

```
DEFINE_ADJUST(adjust_gradient, domain)
{
  Thread *t;
```

```
  cell_t c;
  face_t f;
  domain = Get_Domain(domain_ID);
  /* Fill UDS with the variable. */
  thread_loop_c (t,domain)
  {
    if (THREAD_STORAGE(t,SV_UDS_I(0))!=NULL)
    begin_c_loop (c,t)
      {
        C_UDSI(c,t,0) = (C_VOF(c,t));
      }
    end_c_loop (c,t)
  }
  thread_loop_f (t,domain)
  {
    if (THREAD_STORAGE(t,SV_UDS_I(0))!=NULL)
    begin_f_loop (f,t)
      {
        F_UDSI(f,t,0) = (F_VOF(f,t));
      }
    end_f_loop (f,t)
  }
}
```

/*The in_s_term function calculates the initial source term that will later be smeared.
First, Ntot, which ensures that the total interfacial area remains constant once the scalar field is skewed to the liquid side, is calculated.
Next, the initial source term, as well as its gradient, which is used to calculate the gradient of the energy source term, is calculated.
Finally, the mass flux is multiplied by the interfacial area and the normalisation factor to create the initial source term. */

```
DEFINE_ADJUST(in_s_term, domain)
{
  Thread *t;
  cell_t c;
  m_lg=0;
  m_gr=0;
  Ntot=0;
  domain = Get_Domain(domain_ID);
  /* Calculate integrals and normalisation factor as N*/
  thread_loop_c(t,domain)
  {
    begin_c_loop(c,t)
    {
      Ntop += NV_MAG(C_UDSI_G(c,t,0))*C_VOLUME(c,t);
      if (C_VOF(c,t)<0.99 && C_VOF(c,t)>0.01)
      Nbot += C_UDSI(c,t,0)*NV_MAG(C_UDSI_G(c,t,0))*C_VOLUME(c,t);
    }
    end_c_loop(c,t)
  }
  if (PRF_GRSUM1(Nbot)!=0)
  {
    Ntot=PRF_GRSUM1(Ntop)/PRF_GRSUM1(Nbot);
  }
  /* Calculate mass flux. */
```

```
  thread_loop_c (t,domain)
  {
    begin_c_loop (c,t)
    {
      mgVOF = NV_MAG(C_UDSI_G(c,t,0));
      if (mgVOF>=1 && C_VOF(c,t)<0.99 && C_VOF(c,t)>0.01)
      {
        m_lg = (2*ac/(2-ac))*sqrt(M/(2*pi*R))*RhoG*h*(C_T(c,t)-
T_SAT) /pow(T_SAT, 1.5);
        m_gr=(2*ac/(2-ac))*sqrt(M/(2*pi*R))*RhoG*h/pow(T_SAT, 1.5);
      }
      else
      {
        m_lg=0;
        m_gr=0;
      }
      if (mgVOF>=1)
      {
        m_nt=(2*ac/(2-ac))*sqrt(M/(2*pi*R))*RhoG*h/pow(T_SAT, 1.5);
      }
      else
      {
        m_nt=0;
      }
      C_UDSI(c,t,3)=m_nt*mgVOF;
      C_UDSI(c,t,1)=Ntot*C_VOF(c,t)*m_lg*mgVOF;/* Initial Source
term P0*/
      C_UDSI(c,t,9)=Ntot*C_VOF(c,t)*m_gr*mgVOF;
    }
    end_c_loop (c,t)
  }
}
```

/*The mass_source and mesh_refine functions are unsteady terms that are used to smear the source terms over a constant distance regardless of the size of the time step. */

```
DEFINE_UDS_UNSTEADY(mass_source,c,t,i,apu,su)
{
  real physical_dt, vol, rho, phi_old;
  physical_dt = 4e-9;
  vol = C_VOLUME(c,t);
  rho = C_R(c,t);
  *apu = -rho*vol / physical_dt;/*implicit part*/
  phi_old = C_UDSI(c,t,1);
  *su = rho*vol*phi_old/physical_dt;/*explicit part*/
}
DEFINE_UDS_UNSTEADY(mesh_refine,c,t,i,apu,su)
{
  real physical_dt, vol, rho, phi_old;
  physical_dt = 4e-9;
  vol = C_VOLUME(c,t);
  rho = C_R(c,t);
  *apu = -rho*vol / physical_dt;/*implicit part*/
  phi_old = C_UDSI(c,t,3);
  *su = rho*vol*phi_old/physical_dt;/*explicit part*/
```

```
}
```

/*The diffuse function takes the mass source term, which has been smeared by the Ansys Fluent solver, and bounds it so that mass transfer will only occur within refined cells*/

```
DEFINE_ADJUST(diffuse, domain)
{
  Thread *t;
  cell_t c;
  domain = Get_Domain(domain_ID);
  /* Fill UDS with the variable. */
  thread_loop_c (t,domain)
  {
    begin_c_loop (c,t)
    {
      if (C_UDSI(c,t,4)>=1e5)
      {
        C_UDSI(c,t,5) = C_UDSI_M1(c,t,2);
      }
      if (C_UDSI(c,t,4)<1e5 || C_UDSI_M1(c,t,2)<0)
      {
        C_UDSI(c,t,5) = 0;
      }
    }
    end_c_loop (c,t)
  }
}
```

/* The norm_fct function creates normalisation factors by integrating the initial source term, and then integrating the bounded and smeared source terms to ensure the conservation of total mass transfer*/

```
DEFINE_ADJUST(norm_fct, domain)
{
  Thread *t;
  cell_t c;
  NVbot=0.0;
  NVLtop=0.0;
  NLbot=0.0;
  NL=0.0;
  NV=0.0;
  domain = Get_Domain(domain_ID);
  thread_loop_c (t,domain)
  {
    begin_c_loop (c,t)
    {
      NVLtop += C_UDSI(c,t,1)*C_VOLUME(c,t);
      if (C_VOF(c,t) <= VCutV)
      {
        NVbot += (1-C_VOF(c,t))*C_UDSI(c,t,5)*C_VOLUME(c,t);
      }
      if (C_VOF(c,t) >= (VcutL))
      {
        NLbot += C_VOF(c,t)*C_UDSI(c,t,5)*C_VOLUME(c,t);
      }
```

```
    }
    end_c_loop (c,t)
  }
  if (PRF_GRSUM1(NVbot) !=0 && PRF_GRSUM1(NLbot) !=0)
  {
    NV=PRF_GRSUM1(NVLtop)/PRF_GRSUM1(NVbot);
    NL=PRF_GRSUM1(NVLtop)/PRF_GRSUM1(NLbot);
  }
}
```

/*The vap_src function uses the smeared and bounded source terms and the normalisation factor to explicitly create a source term for the vapour domain*/

```
DEFINE_SOURCE(vap_src,c,sec_th,dS,eqn)
{
  mass_v=0;
  Thread *mix_th, *pri_th;
  mix_th = THREAD_SUPER_THREAD(sec_th);
  pri_th = THREAD_SUB_THREAD(mix_th,0);
  if (C_VOF(c,pri_th)<=VCutV)
  {
    mass_v = NV*(1-C_VOF(c,pri_th))*C_UDSI(c,mix_th,5);/*explicit
part*/
    dS[eqn] = 0;/*implicit part*/
  }
  else if (C_VOF(c,pri_th)>VCutV)
  {
    mass_v = 0;/*explicit part*/
    dS[eqn] = 0;/*implicit part*/
  }
  C_UDSI(c,mix_th,6)=mass_v;
  return mass_v;
}
```

/*The liq_src function uses the smeared and bounded source terms and the normalisation factor to explicitly create a source term for the liquid domain*/

```
DEFINE_SOURCE(liq_src,c,pri_th,dS,eqn)
{
  mass_l=0;
  Thread *mix_th, *sec_th;
  mix_th = THREAD_SUPER_THREAD(pri_th);
  if (C_VOF(c,pri_th)>=(VcutL))
  {
    mass_l = -NL*C_VOF(c,pri_th)*C_UDSI(c,mix_th,5);/*explicit
part*/
    dS[eqn] = 0.0;/*implicit part*/
  }
  else if (C_VOF(c,pri_th)<(VcutL))
  {
    mass_l = 0;/*explicit part*/
    dS[eqn] = 0;/*implicit part*/
  }
  C_UDSI(c,mix_th,7)=mass_l;
  return mass_l;
}
```

/*The enrg_src function uses the initial source term, its gradient and the liquid and vapour source terms,
multiplied by their specific heats to implicitly create a source term for the mixture domain*/

```
DEFINE_SOURCE(enrg_src,c,t,dS,eqn)
{
  real enrg_s=0;
  enrg_s = -C_UDSI(c,t,1)*h+C_UDSI(c,t,7)*cpl*(C_T(c,t)-
298.15)+C_UDSI(c,t,6)*cpg*(C_T(c,t)-298.15);/*explicit part*/
  dS[eqn] = -
C_UDSI(c,t,9)*h+C_UDSI(c,t,7)*cpl+C_UDSI(c,t,6)*cpg;/*implicit
part*/
  C_UDSI(c,t,8)=enrg_s;
  return enrg_s;
}
```